Material Science and Technology Division

Propulsion Materials Program
Quarterly Progress Report for
October through December 2009

D. R. Johnson
Technical Project Manager

Prepared for
U.S. Department of Energy
Assistant Secretary for Energy Efficiency and Renewable Energy
Office of Vehicle Technologies Program
VT 05 04 000

Prepared by the
OAK RIDGE NATIONAL LABORATORY
Oak Ridge, Tennessee 37831-6066
Managed by
UT-Battelle, LLC
for the Department of Energy
Under contract DE-AC05-00OR22725

CONTENTS

Project 18516 – Materials for Electric and Hybrid Drive Systems

***Agreement 16305 – Materials by Design – Solder Joints of High Performance Electronics* (ORNL)**

***Agreement 16306 – Power Electronics Materials Compatibility* (ORNL)**

***Agreement 16307 – Environmental Effects on Power Electronic Devices* (ORNL)**

***Agreement 19201 – MBD Non-Rare Earth Magnetic Materials* (ORNL)**

Project 18517 – Combustion System Materials

***Agreement 11752 – Materials for HCCI Engines* (ORNL)**

Project 18518 – Materials for High Efficiency Engines

***Agreement 13329 – Mechanical Reliability of Piezo-Stack Actuators* (ORNL)**

***Agreement 15050 – Evaluation of Materials via ACERT Engine* (ORNL)**

***Agreement 16303 – Materials for High Pressure Fuel Injection Systems* (ORNL)**

***Agreement 16304 – Materials for Advanced Engine Valve Train* (ORNL)**

***Agreement 17257 – Materials for Advanced Turbocharger Design* (ORNL)**

***Agreement 17894 – NDE for ACERT Engine Components* (Argonne)**

***Agreement 18570 – Alternative Fuels Materials Compatibility* (ORNL)**

***Agreement 18571 – Materials Issues Associated with EGR Systems* (ORNL)**

***Agreement 19202 – Friction and Wear in Ti Components* (ORNL)**

Project 18519 – Materials for Exhaust and Energy Recovery

***Agreement 10635 – Catalysts vs First Principles* (ORNL)**

***Agreement 19214 - Impact of Biofuels on Diesel Particulate Filters* (ORNL)**

<u>Project 18865 – Materials by Design</u>

Agreement 9105 – Characterization of Catalyst Microstructures **(ORNL)**

Agreement 14957 – Thermoelectric Mechanical Reliability **(ORNL)**

Agreement 16308 – MBD - Thermoelectrics Theory and Structure **(ORNL)**

Agreement 17895 – Durability of ACERT Engine Components **(ORNL)**

Agreement 16305: Materials by Design – Solder Joints of High Performance Power Electronics

G. Muralidharan, Andrew Kercher, and Burak Ozpineci
Oak Ridge National Laboratory

Objective/Scope

Advanced hybrid and electric propulsion systems are required to achieve the desired performance and life targets set for future automobiles. As specified in the OFCVT objectives, a target lifetime of 10-15 years has been projected for hybrid and electric propulsion systems meant for operation in harsh automotive environments. Power electronic components and systems are integral components of advanced automotive hybrid and electric propulsion systems. The trend in automotive power electronics is for using higher operating temperatures which has a detrimental effect on the stability of materials used in such systems. The objective of this task is to evaluate the effects of the higher temperatures on critical metallic materials that are used in power electronic devices and systems and to use the Materials-by-Design approach to identify appropriate combinations of materials that would decrease inopportune failures and maximum lifetime and reliability.

Based on the trend for using higher temperatures in power electronic components, there is a significant need to study failures of electronic packages induced by metallurgical changes of solder joints used as die attaches, and in wire bonds exposed to high temperatures (up to 200°C in contrast to the current 125-150°C exposure) anticipated in such applications. These failures can be induced in solder joints and other components by combination of temperatures, stresses, and current. Coarsening of solder joint microstructure along with the formation of intermetallic compounds takes place during high temperature exposure. Wire bonds are also known to be a key location of failures for packages meant for high temperature use. An understanding of the failures in solder joints and wire bonds will empower us to develop a computation-oriented method for the design of materials for packaging applications.

The approach used in this work would be to study failures in simple package designs so that the emphasis is on materials rather than package design thus avoiding complexities of package design issues that may overshadow materials issues. Packages will be subject to extremes of operational stress levels/temperature levels to the study the origin of failures. Steady-state exposure at high temperatures and cyclic exposures (thermal fatigue) all affect microstructure of the materials, their properties, and hence the failure of joints. X-ray radiography along with acoustic and infrared imaging (as is necessary) will be used to characterize voids present in the solder joints. Knowledge from the failures would enable the selection/development of more appropriate materials that would ensure required lifetimes of 10 to 15 years expected of modules in EVs and Hybrid systems.

Technical Highlights

As reported earlier, in collaboration with Powerex Inc., progress has been made in preparing Au-Sn and Sn-Ag solder joints for thermal cycling testing and high temperature exposure. The 2.5 mm x 2.5 mm silicon dies were mounted on a metallized

AlN DBC substrate with the metallization consisting of a medium phosphorus (6-12%) Nickel layer followed by a thin Au layer on the surface. To understand the initial void content in the solder joint, high resolution X-ray radiography was carried out on all the specimens.

Thermal cycling results showed that joints between Au-Sn and Si resulted in cracking of the silicon die during thermal cycling. Ag-Sn joints between silicon and DBC substrates have been tested to 3000 cycles. They do accumulate significant damage and the joint strength evaluation is on hold pending installation of a new die shear system.

In addition to joints based on silicon, SiC joints have been prepared with Au-Sn solders. The SiC dies measure about 2.0 mm x 2.0 mm. These are undergoing thermal cycling between 5°C (5 min. hold) and 200°C (30 min. hold). Figure 1 shows an X-ray image of a Au-Sn solder joint that was processed between SiC dies and med phosphorus (6-12%) Nickel layer with a Au flash substrate in the as-processed condition and after 890 thermal cycles. Note that there is still some voiding observed in the as-processed condition. However, very little damage is evident within the solder joint, and cracking that was observed in earlier experiments with silicon die, are not apparent in these experiments with SiC dies.

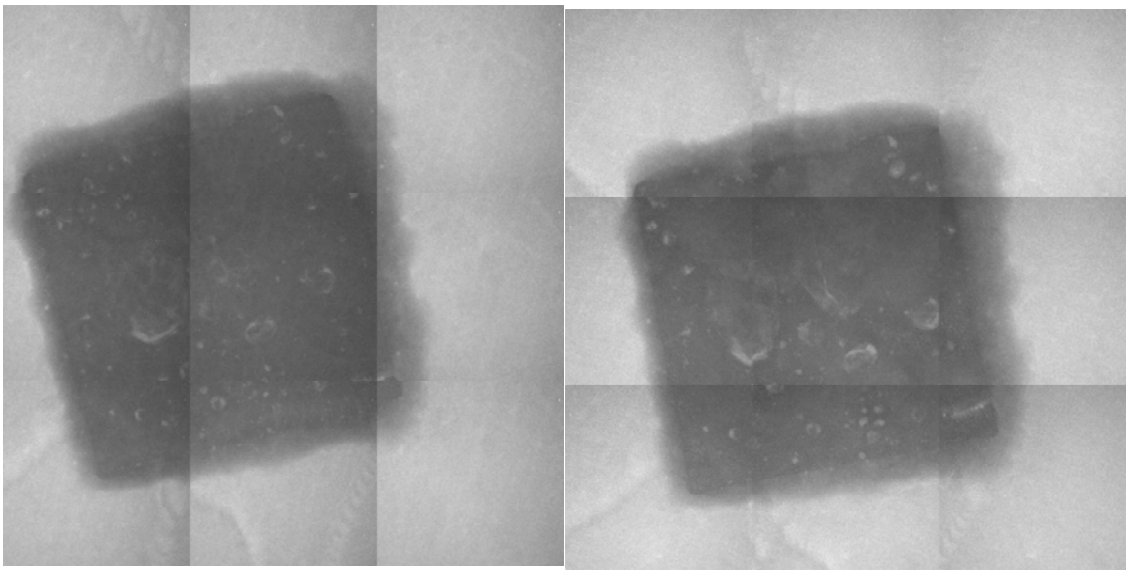

0 890

Figure 1. High resolution X-ray images of Au-Sn joint between SiC dies and DBC substrates before and after 890 thermal cycles showing the evolution of damage within the solder joint.

Finite Element Modeling: In order to understand the relationship between material properties, damage evolution and solder joint fatigue life, finite element modeling of damage evolution in solder joints during thermal cycling has been initiated based upon information available in the literature [1]. 3-D finite element modes of the assembled joints have been created and initial results of stress and strain evolution has been

obtained. Further calculations will be performed to understand the extent of predictive capability available for lifetimes of the solder joints.

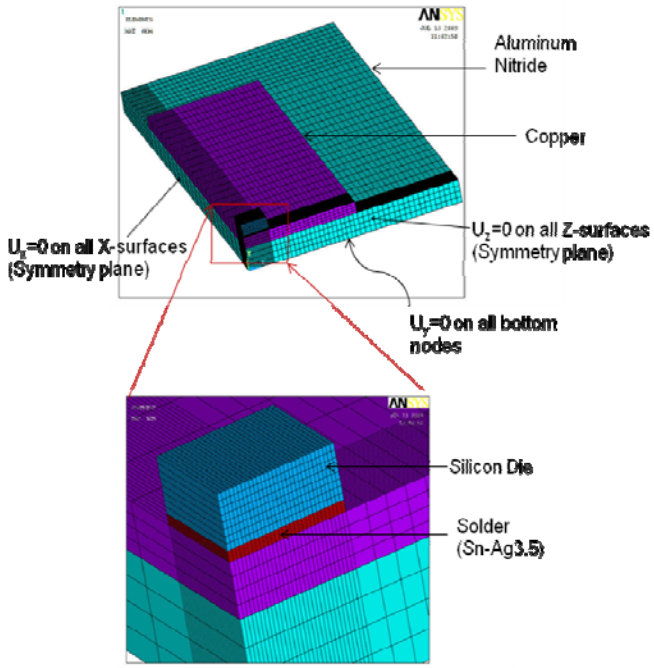

Figure 2. 3-D Finite Element Model of Silicon Die, Sn-Ag Solder Die Attach, and Substrate.

Status of FY 2009 Milestones

Work is on schedule to meet the following milestone.

Complete fabrication and evaluate reliability of sintered joint using one thermal cycling condition (9/2010)

Communications/Visits/Travel

Communications are continuing with Powerex regarding results of solder joint testing. In addition, a meeting with held with Prof. G. Q. Lu of Virginia Tech at Virginia Tech University to discuss the processing of sintered die attaches. A system to accomplish the processing of these joints will be fabricated at ORNL.

Problems Encountered

The Dage BT 22 system that is available at ORNL has a maximum die shear capacity of 20Kg force. Joints prepared with 2.5 x 2.5 mm dies with Au-Sn solder could not be sheared with existing system and a new die shear system Royce 650 has been procured and is being installed for die shear experiments. Figure 3 shows an image of the system that will be installed at ORNL to enable measurement of die shear strengths of solder joints.

Figure 3. Royce 650 universal bond test system procured this quarter to enable testing of joint strengths using die shear measurements.

Publications/Presentations/Awards

None

References

1. Bret. A. Zahn, “Impact of Ball via Configurations on Solder Joint Reliability in Tape-Based, Chip-Scale Packages,” Proceedings of 2002 Electronics Component and Technology Conference, pp. 1475-1483.

Agreement 16306: Power Electronics Materials Compatibility

B. L. Armstrong, D. F. Wilson, C. W. Ayers, S. L. Campbell and S. J. Pawel
Oak Ridge National Laboratory

Objective/Scope

The use of evaporative cooling for power electronics has grown significantly in recent years as power levels and related performance criteria have increased. As service temperature and pressure requirements are expanded, there is concern among the Original Equipment Manufacturers (OEMs) that the reliability of electrical devices will decrease due to degradation of the electronic materials that come in contact with the liquid refrigerants. Potential forms of degradation are expected to include corrosion of thin metallic conductors as well as physical/chemical deterioration of thin polymer materials and/or the interface properties at the junction between dissimilar materials in the assembled components. Initially, this project will develop the laboratory methodology to evaluate the degradation of power electronics materials by evaporative liquids.

Technical Highlights

During this quarter, work was continued on the cycle timing and the current being pushed through the circuits to develop a waveform profile that will allow for failure mechanisms to be expressed. A decision was made to perform testing under the conditions that failure was observed but to terminate testing just prior to the point of observed instability and the resulting changes at the crown of wires on the two cards at the bottom of the test cells, which are shown in Figure 1. The microstructure of these specimens would be compared to those of specimens that were tested to failure (Figure 2) to ascertain the relationship between microstructure and failure mode. As shown in Figure 2, the microstructure near the bond region consists of small diameter, elongated grains and that near the crown consists of very large equiaxed grains. Unfortunately, system failures did allow the desired test cycles to be achieved.

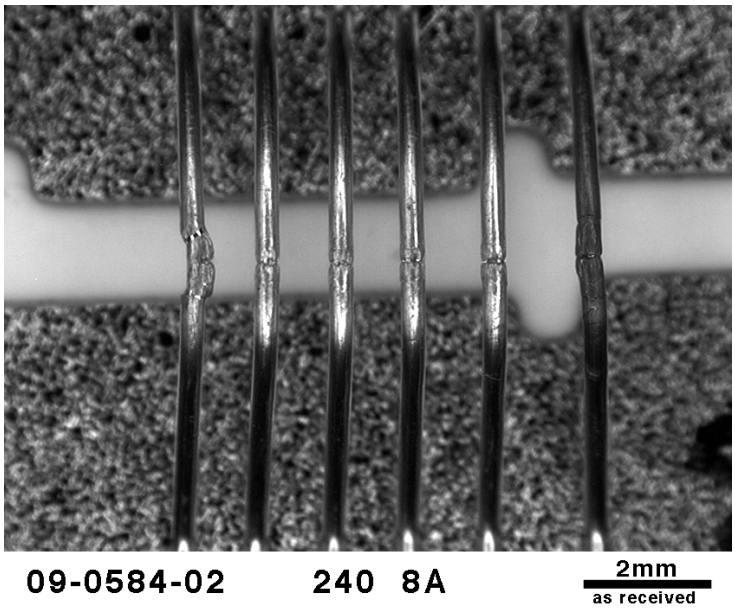

Figure 1. Aluminum wires showing changes that occurred at their crowns.

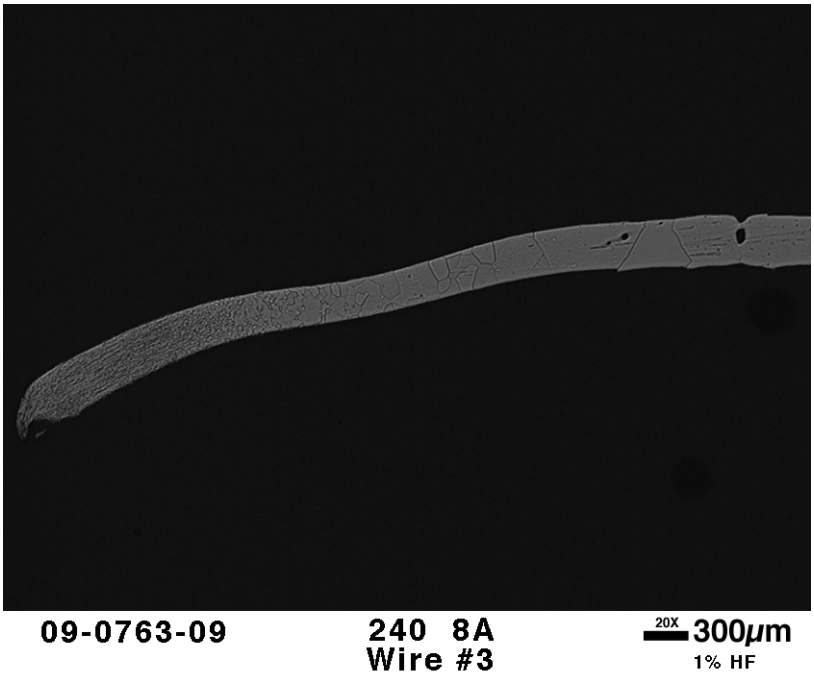

Figure 2. Polished cross section of aluminum wire showing the change in grain size and structure from the bond point (left) to the crown (right).

Work was initiated on the evaluation of as-received bond wires. After evaluation for elemental chemical analysis, Transmission Electron Microscopy specimens were fabricated and analysis of these specimens is on-going.

Status of FY 2010 Milestones

Initiate mapping of materials compatibility space of power electronics with appropriate evaporative coolant. (09/10) On track.

Communications/Visits/Travel

None.

Problems Encountered

Control systems for the cyclic testing system failed repeatedly. The system was evaluated in each instant and functionality was restored. However, this repeated failure did not allow attainment of unattended operation and hence planned long term testing has been delayed.

Publications/Presentations/Awards

None.

References

None to report.

Agreement 16307: Modeling/Testing of Environmental Effects on PE Devices

A. A. Wereszczak, P. J. Ritt, and H. -T. Lin
Oak Ridge National Laboratory

Objective/Scope

Understand the complex relationship between environment (temperature, humidity, and vibration) and the performance and reliability of the material constituents within automotive power electronic (PE) devices and in supportive systems. There is significant interest in developing more advanced PE devices (PED) and systems for transportation applications (e.g., hybrid electric vehicles, plug-in hybrids) that are capable of sustained operation to 200°C. Advances in packaging materials and technology can achieve this but only after their service limitations are better understood via modeling and testing.

Technical Highlights

The specimen preparation for the measurement of thermal diffusivity in a PED was initiated. Two pairs of IGBT and a diode were harvested from an inverter from a 2004 Toyota Prius was supplied by NTRC's T. Burress. The first pair was sectioned to produced a test coupon size appropriate (e.g., 10-13 mm square or diameter) for conventional thermal diffusivity measurements. This is shown in Fig. 1.

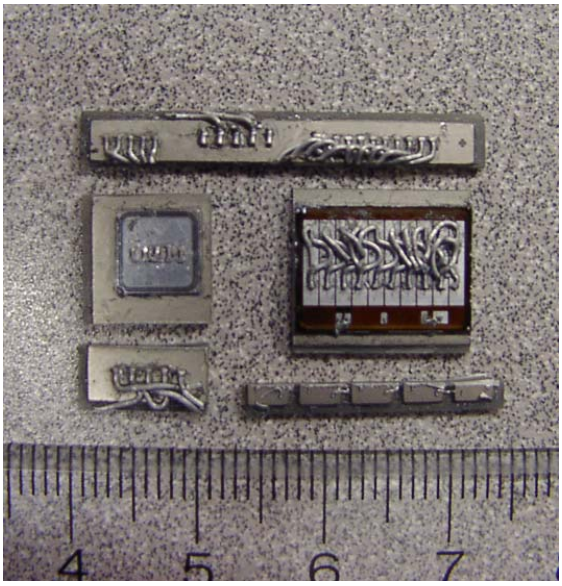

Figure 1. A diode (left-middle) and an IGBT (right-middle) from a 2004 Toyota Prius inverter.

The second pair of diode and IGBT was sectioned, the cross-sections metallographically prepared, and the dimensions and chemistries of the constituents were examined with optical and field-emission scanning electron microscopies (FE-SEM). An optical microscopy image of the IGBT's cross-section is shown in Fig. 2.

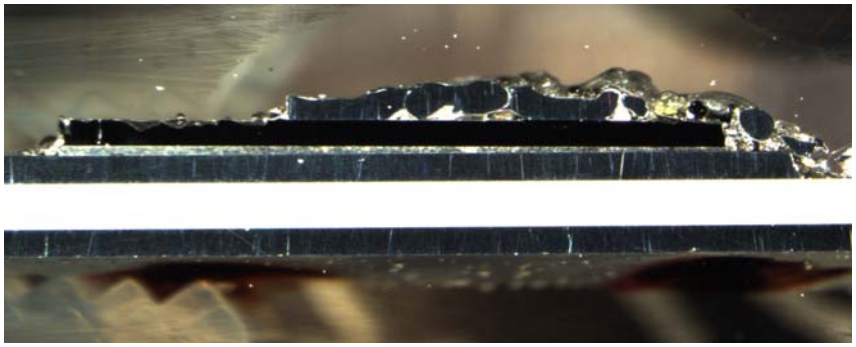

Figure 2. Polished cross-section of the IGBT from a 2004 Toyota Prius inverter. The black layer is the silicon. The light gray layer bonded to the silicon is the solder. The white (or lightest) is the aluminum nitride (AlN) insulator. The layers bonded to the AlN are both aluminum. The gray areas above the silicon are the aluminum wire bonds.

The silicon-side (top in Fig. 2) will be laser-flashed with a flash diffusimeter and the back-side temperature profile will be continuously monitored. This is schematically shown in Fig. 3 for the primary IGBT constituents shown in Fig. 2. A temperature-change - time curve is generated. The "apparent" thermal diffusivity of the entire structure will be estimated from that temperature-time curve. The adjective "apparent" is used because it presents the sum total of all the thermal resistance losses across the structure. The experimental analysis is then combined with a transient finite element analysis (FEA) model of the cross-section geometry where the thermal conductivity, heat capacity, and density of all the material constituents in the cross-section are used as input. Idealized interfaces (i.e., no interfacial resistance) are initially considered. That (idealized interface) transient FEA model is then compared against the experimental results. The FEA model will then be altered in a final step to estimate what the actual "apparent" thermal diffusivity of the PED is. Testing has commenced in early Q2.

An important aspect of the transient FEA analysis is knowing the dimensions (thicknesses) of all the constituents and a priori knowledge of each of their thermal conductivities (□), heat capacities (Cp), and densities (□). The polished cross-sections were examined with an optical comparator, and the thicknesses of each were measured. The thickness of the solder layer in both the IGBT and the diode from the Toyota Prius inverter was not uniform, so this effect on the thermal transfer will be examined and modeled. Additionally, the polished cross-section was examined with a FE-SEM and energy dispersive spectroscopy (EDS) was used to identify the chemistries of each of the constituents. Literature values of the □, Cp, and □ for each constituent are then used in the FEA model. Those constituents are shown in Fig. 3. The solder is a lead-tin (Pb-Sn) composition.

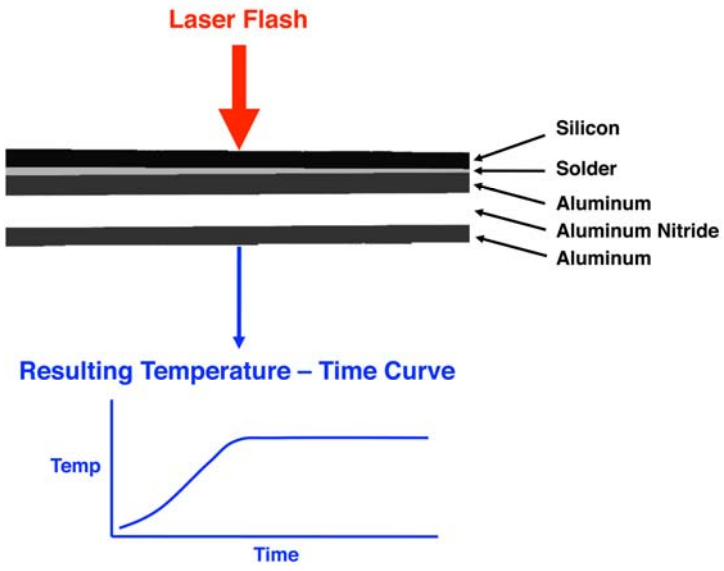

Figure 3. Schematic of the laser flash experiment performed with a (multilayered) IGBT.

Status of FY 2010 Milestones

Develop a test coupon, method, and model that will estimate and measure the apparent thermal diffusivity of a PED's die-solder-DBC laminate. (09/10) *On schedule.*

Communications/Visits/Travel

Wereszczak had numerous meetings with VT APEEM PIs L. Marlino, F. Wang, and R, Wiles to discuss collaborative efforts. Wereszczak also had several discussions with NREL about prospective collaborations involving the thermal diffusivity experiments run in this project.

Problems Encountered

None.

Publications/Presentations/Awards

An abstract entitled "Edge-Controlled Mechanical Failure of Si and SiC Semiconductor Chips" co-authored by A. A. Wereszczak, O. M. Jadaan, and T. P. Kirkland was submitted to the IMAPS sponsored conference High Temperature Electronics (HiTEC 2010), which will be held May 11-13, 2010 in Albuquerque, NM.

References

None.

Agreement 19201: Non-Rare Earth Magnetic Materials

Michael A. McGuire and David J. Singh
Oak Ridge National Laboratory

Objective/Scope

We will examine rare-earth-free chemical systems which hold promise for the discovery of new high-temperature ferromagnets with the large magnetic moments and strong anisotropies required for technologically useful permanent magnet materials. This research will focus on the development of new rare-earth free permanent magnet materials. Understudied chemical systems which are likely to contain materials with properties required for useful ferromagnets (large moments, high Curie temperatures, strong magnetic anisotropy) will be synthesized and characterized. First principle calculations will be performed to aid in the identification of promising target materials and to guide chemical tuning of magnetic properties through element substitutions and alloying. The focus will be on materials based on elements, such as Mn, Fe and Co, suitable for application in vehicles.

The primary challenge in this work is to obtain high magnetic anisotropy without rare-earth elements, while maintaining high saturation magnetization. The two main sources of anisotropy are magneto-crystalline anisotropy and shape anisotropy. Magneto-crystalline anisotropy is an intrinsic property determined by energy required to rotate a magnetic moment relative to the crystal lattice. Shape anisotropy is an extrinsic property related to the domain structure of individual crystallites. We are targeting new materials with large magneto-crystalline anisotropy, which could then be further enhanced by materials processing to optimize magnetic domain configurations.

Technical Highlights

During the first quarter of FY2010, extensive surveys of literature, phase diagrams, and crystal structure databases were undertaken. Through this process we have identified promising chemical systems which combine the magnetic transition metals iron and cobalt with heavy, non-rare earth elements, in which spin-orbit coupling should be strong. Magneto-crystalline anisotropy arises from strong spin-orbit interactions, which couples the magnetic spins to the crystal lattice. Materials chosen for investigation and chemical manipulation include:

(1) *Understudied cobalt rich compounds with Hf or W.* Hf_2Co_7 is ferromagnetic below about 420 K, but little else is known about this material. $HfCo_7$ has a Curie temperature of about 600 K and a saturation moment of about 1.1 Bohr magneton per cobalt. WCo_3 also has not been thoroughly characterized, and has been observed primarily as a precipitate in tungsten containing steels. Analysis of these intermetallic compounds and improvement of magnetic properties through alloying and/or addition of interstitial elements will be pursued.

(2) *Hexagonal Laves phases MT_2 (M = Hf, Ta, W; T = Mn, Fe, Co)*. These materials should serve as good model systems for understanding the effects of chemical

manipulation of magnetic properties. Many are near ferromagnetic instabilities, and studying how the ferromagnetic state can be stabilized via chemical substitutions and the inclusion of interstitial atoms would aid in the design of new magnetic materials. In particular, the effects of interstitial nitrogen will be explored. One strategy that will be employed is the addition of small amounts of titanium to these (and other) phases which will likely facilitate the uptake of nitrogen.

Status of FY 2010 Milestones

Progress toward our milestone of discovering new ferromagnetic materials that do not contain rare-earth elements is on schedule. The initial phase of this project has focused primarily on reviewing literature and databases to identify promising chemical systems for detailed study. Synthesis of targeted compositions will be the main focus of the second quarter of FY 2010.

Communications/Visits/Travel

None to report for this quarter.

Problems Encountered

No significant problems have been encountered.

Publications/Presentations/Awards

None to report for this quarter.

References

None for this report.

Agreement 11752: Advanced Materials Development through Computational Design for HCCI Engine Applications

Govindarajan Muralidharan, Rick Battiste and Bruce Bunting
Oak Ridge National Laboratory

Objectives/Scope

To identify and catalog the materials operating conditions in the HCCI engines and utilize computational design concepts to develop advanced materials for such applications.

Highlights

Technical Progress

Materials-by-Design of Advanced Materials:

In this quarter, work was continued on Ni-based alloys for valve applications. As reported earlier, using thermodynamic modeling, microstructure evaluation, and mechanical property evaluation, high temperature fatigue was identified as a property of critical interest in Ni-based alloy valve materials for the next generation automotive engines. In order to develop relationships between the microstructures of the alloys and their mechanical properties, high-temperature fatigue property data were obtained on all down-selected alloys as a part of the project. Using the approximate correlation between the fatigue lives obtained using the rotating beam and fully reversed fatigue testing techniques several alloys with required microstructures have been identified as candidates for high temperature valve applications.

Using the microstructures of these alloys as a guide, computational thermodynamics was used to identify additional alloys with microstructure similar to the commercial alloys with desirable properties. In contrast to the commercially available alloys with Ni-contents in the range of 50 wt. % to 60 wt. %, the Ni-content in these alloys ranges from about 30 wt. % to 45 wt. % with the potential to achieve comparable properties. This implies that the alloys will be of lower cost but comparable mechanical properties. Figure 1 shows a typical small heat of alloy that was cast at ORNL. Subsequent to casting, these alloys were homogenized and rolled at high temperatures. Small tensile specimens were machined from these alloys and tensile tests were conducted *in-situ* at 870°C. Figure 2 shows a typical stress-strain curve obtained from a new alloy. Note that the yield strength at 870°C for this alloy was measured to be 66 ksi about in contrast to previous alloys developed at ORNL which had high temperature UTS of 47 ksi. Further optimization of alloy composition and heat-treatment procedure will be performed in FY 2010.

Figure 1. Small heats of alloys were melted and cast in a vacuum arc furnace, homogenized, aged, and specimens were machined for high temperature tensile tests.

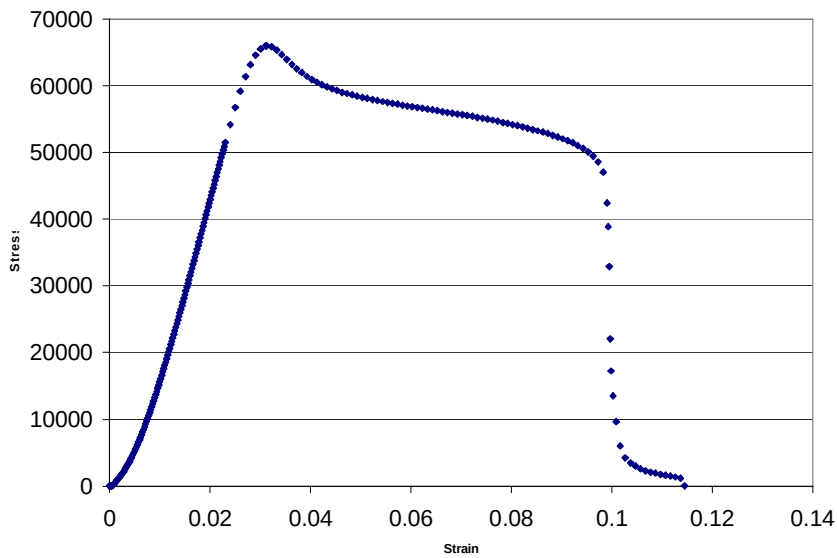

Figure 2. Stress (in Ksi) vs. Strain relationship at 870°C for a new alloy cast at ORNL obtained using in-situ high temperature tensile tests.

Milestones

Work is on schedule to meet the following milestone:

Complete selection of one commercial alloy and one newly developed alloy for high temperature valve application. **(9/2010)**

Agreement 13329: Mechanical Reliability of Piezoceramic Multilayer Actuators

H.-T. Lin, H. Wang, T. Matsunaga and A. A. Wereszczak
Oak Ridge National Laboratory

D. W. Memering, J. Carmona-Valdes and R. Stafford
Cummins Inc.

Objective/Scope

Enable confident utilization of piezo stack actuator in fuel injectors for heavy vehicle diesel engines. The use of such actuators in diesel fuel injectors has the potential to reduce injector response time, provide greater precision and control of the fuel injection event, and lessen energy consumption. Though piezoelectric function is the obvious primary function of lead zirconate titanate (PZT) ceramic stacks for fuel injectors, their mechanical reliability can be a performance and life limiter because PZT is brittle, lacks high strength, and is susceptible to fatigue. However, that brittleness, relatively low strength, and fatigue susceptibility can be overcome with the use of appropriate probabilistic design methods.

Technical Highlights

1. Piezoceramic Characterization

Efforts have been made to characterize the mechanical properties of KCI and EPCOS PZT materials as well as the effects of several critical factors identified during this reporting period. The strength-limiting flaws and electric field and their influences on the flexural strength of KCI PZT were studied by using both as-extracted and as-received specimens. Major up-to-date observations can be summarized as follows: 1) contact conditions (steel ball plus steel ring versus ceramic ball plus polymer ring) exerted an insignificant effect on the flexure strength of ball-on-ring; 2) the as-extracted PZT exhibited a lower strength than the as-received in ball-on-ring loading; 3) for the as-extracted PZT, the loading under 4-point bend resulted in a lower value of mechanical strength than ball-on-ring flexure; 4) under electric field, strength responses of the as-received PZT in ball-on-ring appeared to be asymmetric; in other words, a positive field resulted in a higher value than that in the open circuit and vice versa. The effect of electric field on the flexure strength is shown in Fig. 1 [1]. It is worth noting that this asymmetry turns out to be only significant with the positive electric loading. The overlapping confidence rings corresponding to the open circuit and negative field suggest that a negative field tended to degrade the strength, but the effect was insignificant. These tests revealed the important roles played by inherent flaws and polarization. Their response to other factors such as high temperature and humidity is not yet clear and needs to be tested and characterized thoroughly as required by the

application. These aspects were considered in this past quarter and will be continually concentrated in the following period of this project.

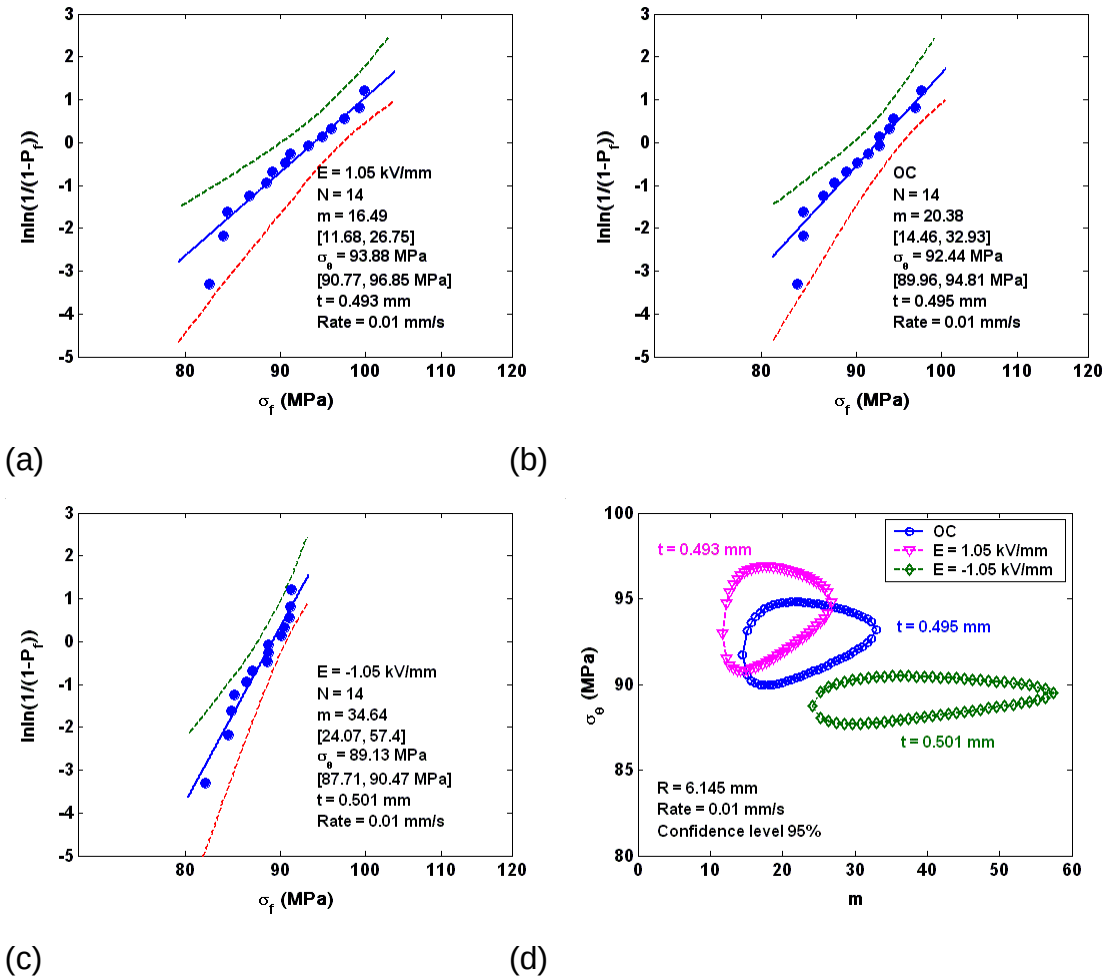

Fig. 1. Weibull plots of flexural strength for the as-received PZT in (a) 1.05 kV/mm, (b) open circuit, (c) -1.05 kV/mm, and (d) confidence ratio rings (95% level). Data were obtained using ball-on-ring setup with 6.4 mm steel ball and 9.5 mm steel ring [1].

Semi-articulated 4-point flexure was used to test and evaluate the flexure strength and temperature effect of KCI PZT in both as-received and as-extracted states (Fig. 2). For the as-extracted PZT, it appeared that the strengths subjected to various temperatures actually had a similar range of variation. The Weibull moduli of as-extracted PZT changed a little. The position of 100°C confidence ring is seen to be separated from other two. This may manifest the relative role of different strength-limiting flaw types that were activated under a sampling condition. It is interesting to see that, for the as-received PZT, the strength at 25°C was significantly higher than that at 200°C, while

the latter exhibited a confidence ring largely overlapping with those of the as-received PZT. There are at least two points that can be made with regard to the observation: 1) the temperature indeed had a significant effect on the mechanical strength of this PZT material; 2) the strength insensitivity of as-extracted PZT to temperatures may be attributed to the heating-induced depolarization in the single layer extraction. The heating to more than 200°C (but lower than its Curie temperature) during the extraction may result in partially-reoriented polarization that was frozen by the cooling to room temperature. Testing of as-extracted PZT thus reflected the status of PZT in heating, and their strength eventually was equivalent to that of the as-received PZT under corresponding temperature range.

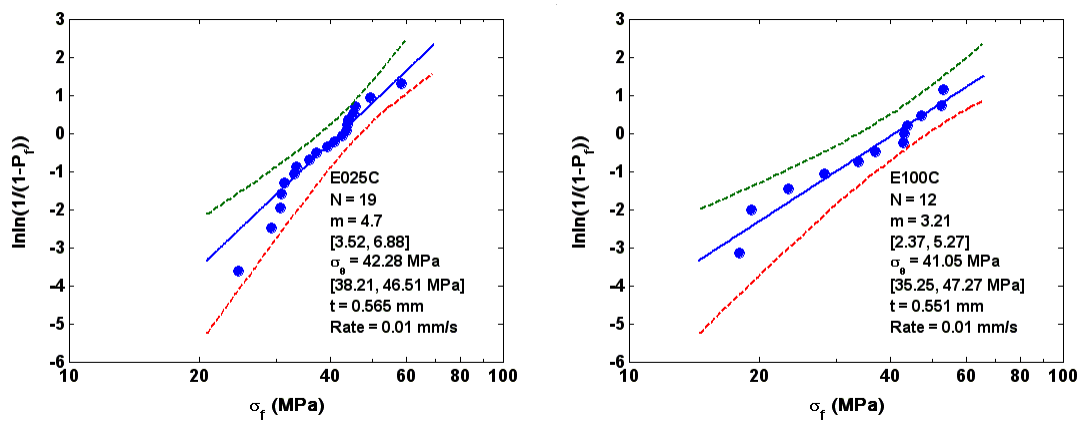

(a) (b)

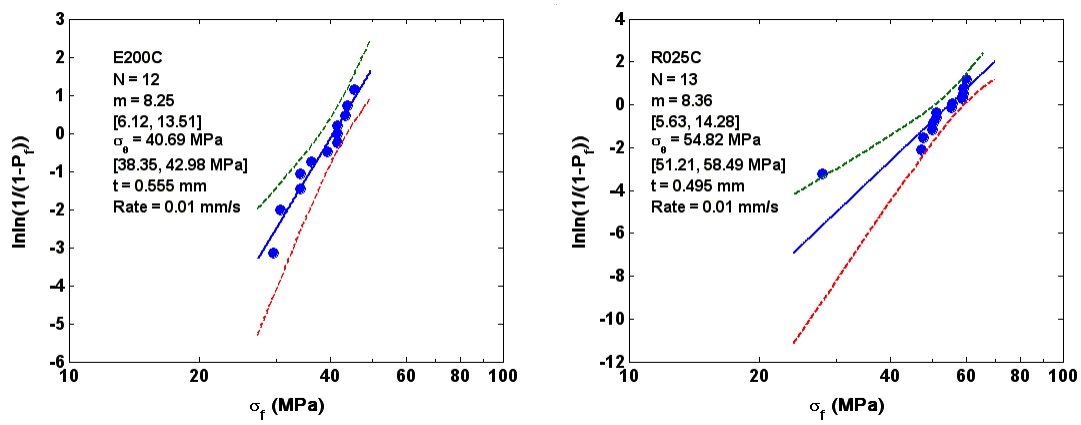

(c) (d)

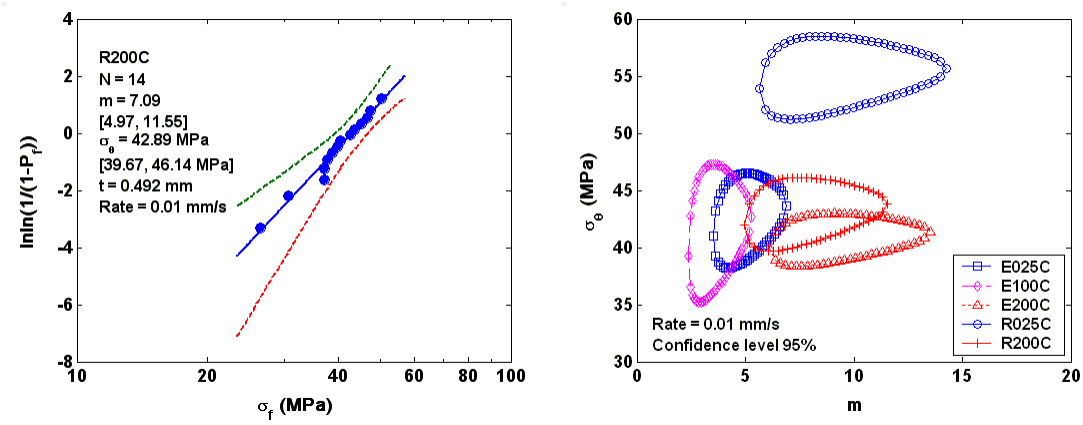

(e) (f)

Fig. 2. Weibull plots of flexure strength for (a) as-extracted PZT at 25°C, (b) at 100°C, (c) at 200°C, (d) as-received PZT at 25°C, (e) at 200°C, and (f) confidence ratio rings (95% level); 4-point bend with 3.175 mm of loading span and 6.35 mm of supporting span was used.

Extensive fractographical studies have been conducted using optical and scanning electron microscopes. Surface-located volume pore, porous region, agglomerate, and surface void were again revealed as related to identified failure origins. Several representative origins are given in Fig. 3.

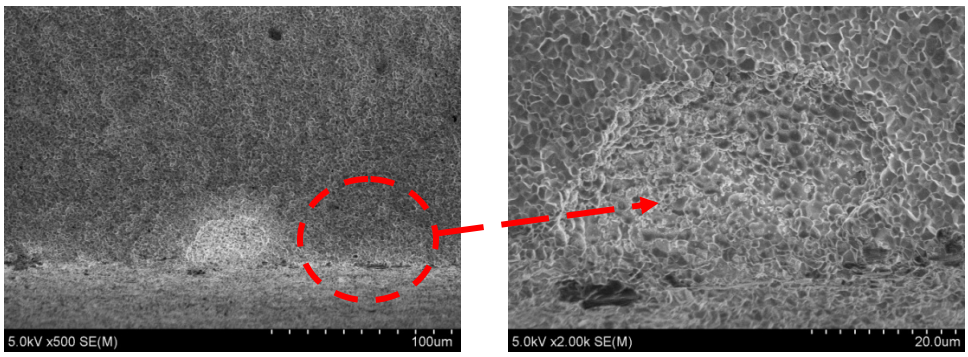

(a) (b)

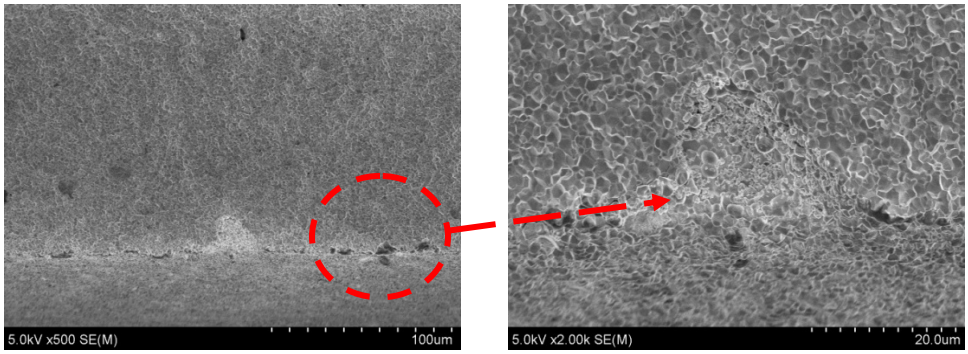

(c) (d)

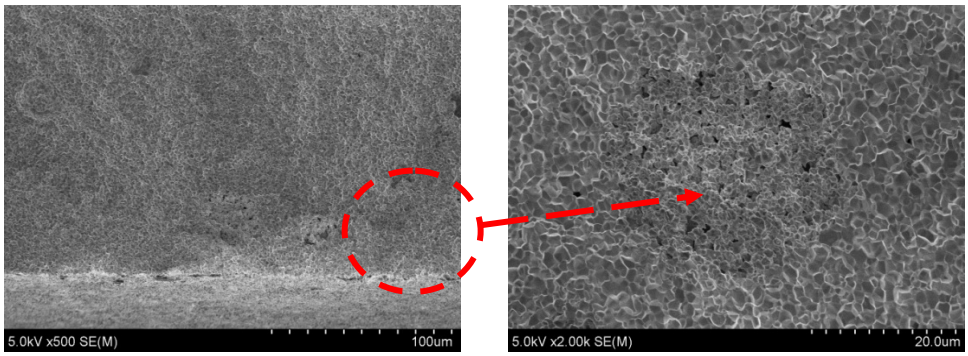

(e) (f)

Fig. 3. Failure origins featuring (a) & (b) volume pore, σ_f = 58.8 MPa, (c) & (d) surface void, σ_f = 50.1 MPa, and (e) & (f) porous region, σ_f = 60.0 MPa. Data were based on the as-received PZT and semi-articulated 4-point flexure setup was used with loading span 3.175 mm and supporting span 6.35 mm; the crosshead rate was 0.01 mm/s.

It has been a challenge to prepare the single layers of EPCOS PZT directly for proposed testing. Alternatives were pursued, especially the stack-based bending beams with different cross section geometric shapes and sizes. Such approach is effective in characterizing materials' strength against prevailing delimination as revealed on cross sections of the many stacks that failed in field tests. However, the investigation showed that this involved a substantial amount of preparation in order to meet a required number of specimens. Working toward this direction, the project was able to prepare a sufficient number of 10-layer plates from a commercial EPCOS stack (AN0X8500b). These plates, sized 6.8mm x 6.8mm x 0.67mm, appeared to be fairly uniform and can be used in 4-point flexure to test and evaluate the mechanical property of comprising PZT. The same semi-articulated 4-point bend flexure was used for this purpose. The results were shown in Fig. 4 with respect to the Weibull plot and corresponding confidence ring. The results based on the single layer of equivalent PZT (tape-cast) are also given in this

figure. As expected, the strength of 10-layer plates is relatively lower than of single-layer plates. The factographical study on these plates revealed a failure origin that featured the brittle facture of PZT layer and ductile failure of internal electrode (Fig. 5).

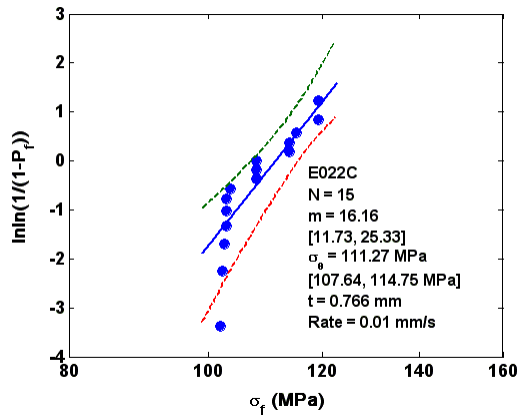

(a)

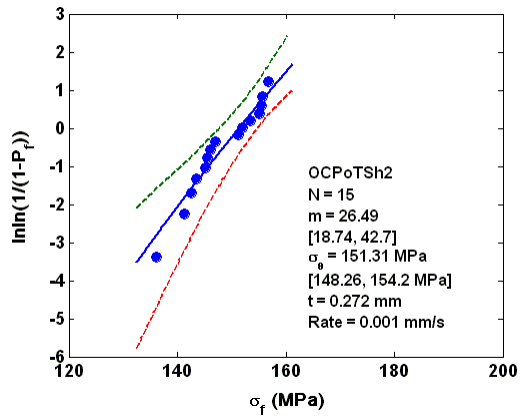

(b)

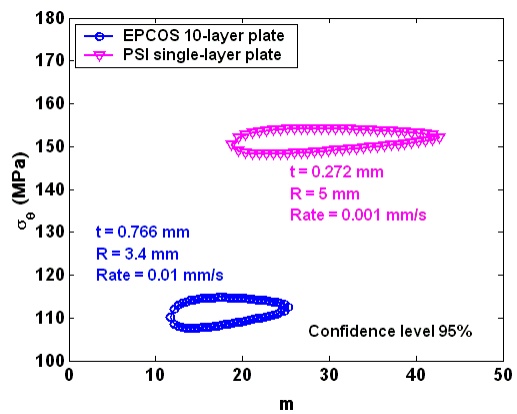

(c)

Fig. 4. Weibull plot for (a) as-extracted 10-layer EPCOS PZT, (b) single-layer PSI PZT, and (c) 95% confidence rings. Data were generated using ball-on-ring set up.

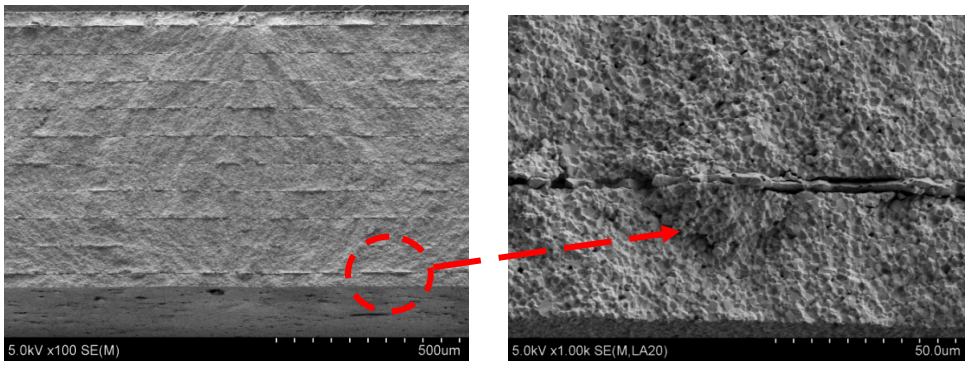

(a) (b)

Fig. 5. (a) Fracture surface of a 10-layer EPCOS plate (as-extracted) resulting from ball-on-ring loading and (b) failure origin; the crosshead rate was 0.01 mm/s.

2. PMLA Characterization

Testing on KCI stack (type A) was under consideration. This stack has a large capacitance and, at the same time, needs a high voltage for driving. Special attention must be given to the test setup and instrumentation, both of which shall be redesigned and modified as much as necessary. A piezo driver was acquired from KCI through Cummins, Inc. This driver has been calibrated in this past quarter and the driving software is being modified to accommodate the requirement from on-line data acquisition. Modification of the current testing frame is under way to account for the additional requirement on dynamics of system. At the same time, discussions on testing and characterization for ECPOS stack (type B) occurred with Cummins, Inc. as regarding the testing condition and requirements. Additional tests on type B stacks were planned.

The project continued the effort to develop a methodology on effectively characterizing the fatigue-induced structure damage of stacks. Model stacks from Noliac that were tested and evaluated extensively in the previous stage of the project using semi-bipolar electric loading was used. Particularly, a unique technique that had sequential polishing involved was developed along with optical microscopy and SEM. Through appropriate preparation, the multi scale damages can be revealed and observed that range from delimination, pores to etch groove relevant to domain activity. This technique is different from the gradual grinding used in industry for evaluating the internal damage of a failed stack. The grinding is efficient at revealing the extended cracks but modifying the domain structure. The latter is important information on the fatigue response of a PZT stack though. The relevant results have been summarized in this past quarter [2], and the application of the developed approach to failed stacks from field tests has been discussed with Cummins, Inc.

Status of FY 2010 Milestones

Measure and compare reliability of competing commercially available piezoactuators under consideration for use in diesel fuel injectors, *on schedule*.

Communications/Visits/Travel

Conference calls on CRADA update with Cummins, Inc. were held on Aug. 10 and Oct 1. Hua-Tay Lin and Hong Wang, along with Program Manager Dr. D. Ray Johnson, visited Cummins, Inc. on Dec. 1, 2009. Discussions were made regarding the future work under the current CRADA.

Publications/Presentations/Awards

1. Wang, H., Matsunaga, T. and Lin, H.-T., Characterization of poled single-layer PZT for piezo stack in fuel injection system, paper to be submitted and presented on *34th Int. Conf. on Adv. Ceramics and Composites*, Jan. 24-29, 2010, Daytona Beach, FL
2. Lin, H.-T., Wang, H., Wereszczak, A. A., Memering, D., Carmona-Valdes, J., Stafford, R., Design optimization of piezoceramic multilayer actuators for heavy duty diesel engine fuel injectors: 1) mechanical characterization of KCI and EPCOS plate specimen; 2) electric fatigue of as-received KCI single-layer plate specimen; 3) fatigue characterization on EPCOS and KCI stacks with mechanical preload, presented on 2nd *Meeting on ORNL-Cummins CRADA*, Dec. 1, 2009, Columbus, IN.
3. Wang, H., Cooper, T. A., Lin, H.-T., and Wereszczak, A. A., Fatigue responses of PZT stacks under semi-bipolar electric cycling with mechanical preload, to be submitted to *J. Appl. Phys.*, 2010.
4. Wang, H., Lin, H.-T., and Wereszczak, A. A., Strength properties of poled PZT subjected to biaxial flexural loading in high electric field, submitted to *J. Am. Ceram. Soc.*, 2009.
5. Wang, H., Lin, H.-T., Cooper, T. A., and Wereszczak, A. A., Mechanical strain and piezoelectric properties of PZT stacks related to semi-bipolar electric cyclic fatigue, *Proc. 33rd Int. Conf. on Adv. Ceramics and Composites*, Jan. 18-23, 2009, Daytona Beach, FL, also on Advances in Electronic Ceramics II, *Ceram. Eng. Sci. Proc.,* 30 (9), 2009, 53-63.

References

1. Wang, H., Matsunaga, T. and Lin, H.-T., Characterization of poled single-layer PZT for piezo stack in fuel injection system, to be submitted to *Proc. 34th Int. Conf. on Adv. Ceramics and Composites*, Jan. 24-29, 2010, Daytona Beach, FL
2. Wang, H., Cooper, T. A., Lin, H.-T., and Wereszczak, A. A., Fatigue responses of PZT stacks under semi-bipolar electric cycling with mechanical preload, to be submitted to *J. Appl. Phys.*, 2010.

Agreement 15050: Evaluation of Materials via ACERT Engine (CRADA with Caterpillar)

Michael Kass, Norberto Domingo, Robert M. Wagner, H. T. Lin, D. Ray Johnson, and Brian C. Kaul
Oak Ridge National Laboratory

Objective/Scope

This project is focused on improving the performance, emissions and efficiency of heavy-duty diesel engines through the application of materials enabled technologies. The range of material systems is comprehensive and includes 1) improved structural materials to accommodate higher cylinder pressures and temperatures, 2) improved durability and corrosion resistance, 3) low inertial components to improve transient response, 4) improved emissions aftertreatment performance, and 5) waste heat recovery systems.

To date a dynamometer engine research cell was constructed for use with heavy-duty engines. A 2004 C15 ACERT Caterpillar engine was provided by the Caterpillar materials research staff for materials-based efficiency evaluations. The engine was instrumented for combustion and thermal assessment. During FY09, the Caterpillar combustion research staff signed a WFO agreement with ORNL to evaluate a thermodynamic model used to assess efficiency improvements on the ACERT engine.

Progress This Quarter (October – December 2009)

- A power factor correction system was installed in the test cell to better facilitate power transfer from the dynamometer to the grid. This system eliminates power fluctuations in the building power that had previously caused problems at high engine loads.
- Baseline testing of the engine has begun. These data will be used for comparison when modified components are tested in upcoming reporting periods.
- A sample comparison of ORNL baseline data to data provided by Caterpillar for this engine model is shown in Figures 1 and 2 for 1200 RPM operation.

  As illustrated here, there are some performance differences between this engine as configured at ORNL and Caterpillar's baseline. Notably, the ORNL engine is de-rated such that the highest load point from the Caterpillar data set is not obtainable; also, the with this calibration, a higher air flow is observed for a given power output, along with a slightly leaner A/F ratio.

  Due to these differences in the engine controller calibration, a complete set of baseline data for the engine as-installed at ORNL, across the speed/load map, will be used in evaluating revised parts, rather than relying on Caterpillar-supplied data.

- Preliminary discussions are ongoing to identify components for evaluation. Technologies include insulating components for improved waste-heat recovery and thermoelectrics.

Publications/Presentations/Awards

No publications or presentations occurred during this quarterly period.

Plans for Next Reporting Period

- Complete the acquisition of baseline data in preparation to use for comparison when evaluating components.

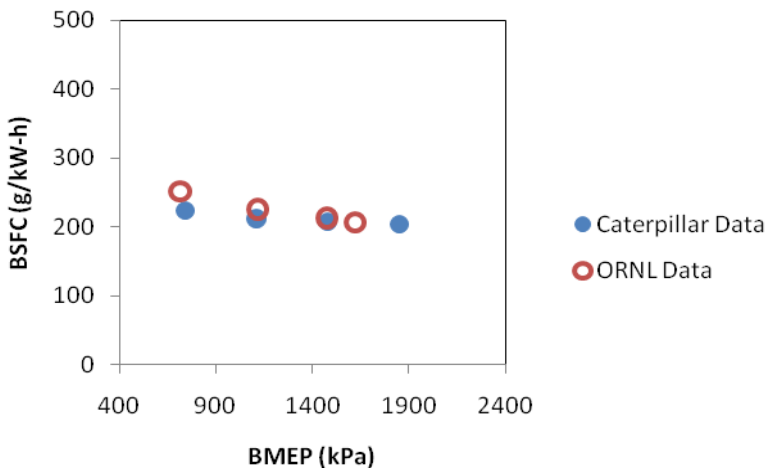

Figure 1 - Baseline BSFC Data at 1200 RPM

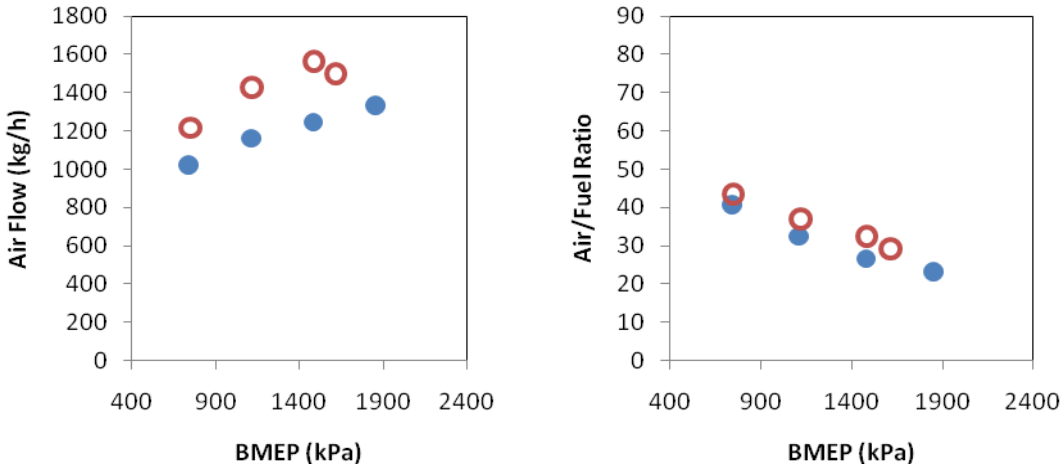

Figure 2 - Baseline Air Flow and Air/Fuel Ratio Data at 1200 RPM

Agreement 16303: Materials for High Pressure Fuel Injection Systems

Peter J. Blau, Jane Howe, Dorothy Coffey, and Amit Shyam
Oak Ridge National Laboratory
and
Michael J. Pollard
Caterpillar Corporation

Objective/Scope

The objective of this Cooperative Research and Development Agreement (CRADA) between UT-Battelle, LLC and Caterpillar Corporation is to advance the state of the art in the characterization, selection, and use of metallic alloys for high-pressure diesel engine fuel injector nozzles.

During recent decades, fuel efficient, low-emissions diesel engine designs for heavy trucks have relied upon increasing fuel injection pressures to optimize combustion characteristics. Precise fuel metering is required. This key functional requirement has raised concerns over the ability of spray holes to be machined to sufficiently close tolerances to provide desired spray patterns and for the materials of construction to withstand hundreds of millions of high-pressure pulses without succumbing to fatigue damage. The data and analyses obtained in the course of this three-year effort are expected to provide vital information for designers of high-performance fuel systems for advanced, energy-efficient diesel engines.

A three-pronged approach has been developed. It involves: (1) characterization of current fuel injector hole geometry and alloy metallurgy, (2) measuring the residual stress in nozzle tips near spray holes, and (3) development and use of specialized fatigue test methods to address the special requirements of the next generation of high-pressure fuel injectors.

Technical Highlights

A recent review of this project was conducted internally at Caterpillar. The consensus was that a modified approach, including the temporary suspension of residual stress work, and the adoption of the current fatigue testing plan was appropriate. The following highlights describe recent fatigue testing results and some new electron microscopy work underway.

Fatigue testing and fractographic analysis.
Fatigue tests lasting over 10 million cycles, and at various stress levels, have been completed on smooth, hour-glass type, heat-treated test specimens provided by Caterpillar. As shown in Figure 1, the alloys exhibited two modes of fatigue initiation, separated by a characteristic threshold maximum stress value, in this case about 900 MPa. Short-lived specimens tend to fail from surface-initiated flaws and those at lower stresses tend to fail from bulk initiated flaws. This interesting dual failure mode behavior has been observed in the case of other steels, but this is the first time that it has been observed with the current fuel injector nozzle alloy.

Fractographic analyses of the steel specimens are being conducted at ORNL to substantiate the reasons behind this kind of behavior. A publication on these results is anticipated, but will be subject to approval by the CRADA partner.

Electron microscopy of hole walls.
In order to study the microstructure produced by the process that produces spray holes, and especially to consider potential sources of micro-fracture initiation, a focused ion beam (FIB) method was employed to remove a tiny slab of material from the inside of a fuel injector sack spray hole wall. Figure 2 shows the features of tiny specimen with a carbon capping layer, an oxide layer, and the steel beneath it. Once the specimen has been sufficiently thinned, transmission electron microscopy work will be performed.

Plans for the coming quarter

1) Continue to conduct axial fatigue tests and fractography of fuel injector alloy specimens that have been machined and heat treated at Caterpillar.

2) Complete installation and calibration of an optical imaging system to track the growth of fatigue cracks in situ, near the edges of holes in the gauge sections of fatigue specimens.

3) Conduct a transmission electron microscopy study of the fine structure of re-cast layers in injector hole walls.

Status of FY 2010 Milestones

1) Complete baseline fatigue tests on smooth specimens without artificial flaws. **(3/31/2010) Status:** on-going

2) Complete fatigue tests on heat-treated steel specimens containing holes produced by the same process used on fuel injector nozzles. **(9/30/2010) Status**: to be started.

Communications/Visits/Travel

Monthly coordination calls have been made between ORNL and Caterpillar.

Problems Encountered

Equipment and staff are ready at ORNL to continue multi-million-cycle fatigue testing; however, there has been a delay in receiving machined specimens for fatigue studies from the partner. Both milestones for FY 2010 are dependent on the availability of test specimens, so this is a critical situation for meeting the project work schedule. Efforts are being made to expedite the issue.

Publications/Presentations/Awards

None this period.

References

None

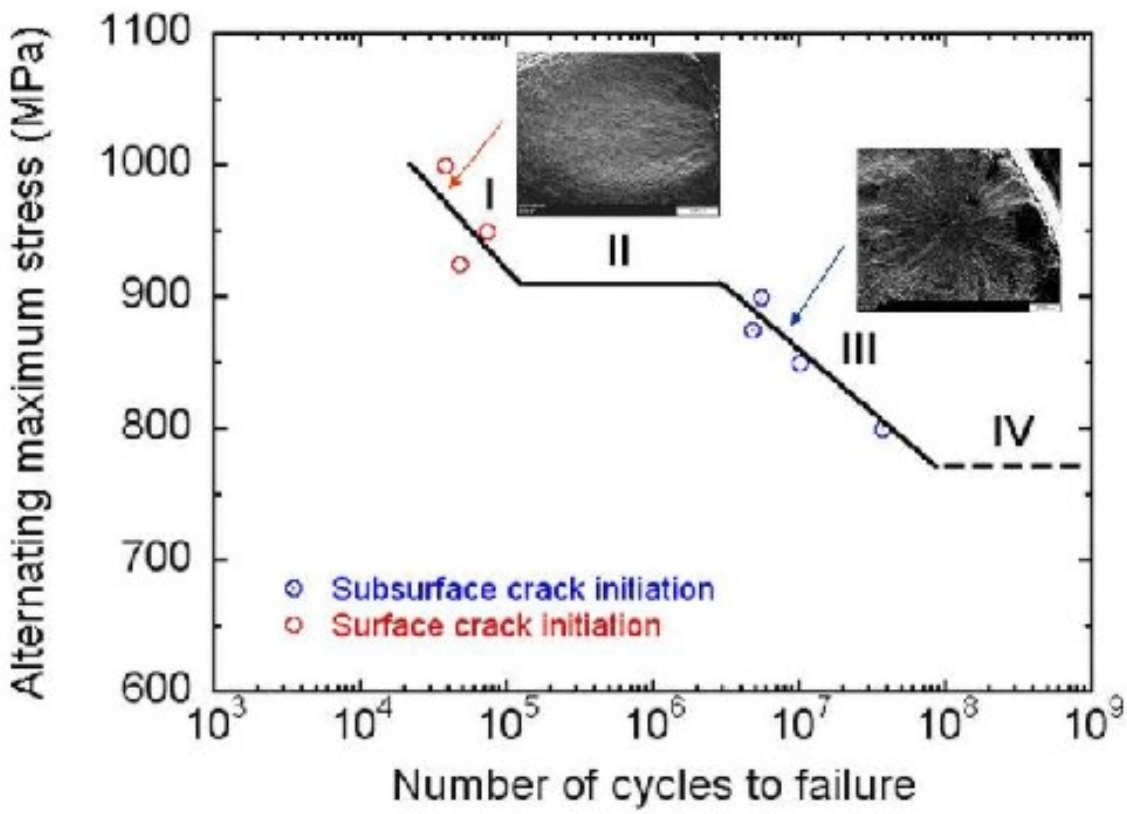

Figure 1. Illustration of the discontinuous relationship between fatigue life and the applied maximum stress. Image insets show fracture surfaces that exemplify surface-initiated failure (region I) and bulk flaw initiation (region III).

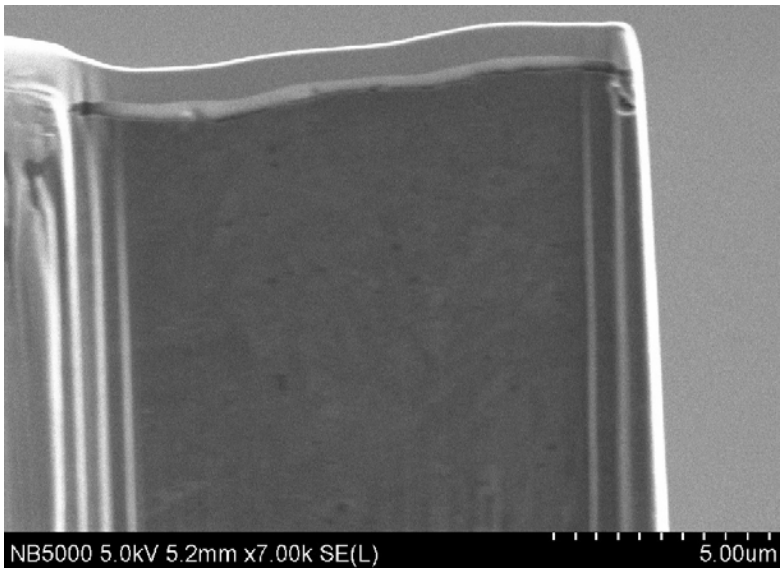

Figure 2. Specimen cut from the wall of a spray hole. The top gray band is the capping layer to help hold the specimen. Immediately below it is a light layer of oxide on the hole wall surface, and below that is the steel containing both the recast layer below the oxide and the bulk microstructure below that (scanning electron microscope image).

Agreement 16304: Materials for Advanced Engine Valve Train

P. J. Maziasz and N. D. Evans
Oak Ridge National Laboratory
and
N. Phillips
Caterpillar, Inc.

Objective/Scope

This is an ORNL CRADA project with Caterpillar, NFE-07-00995 and DOE OVT Agreement 16304, which lasts for about 3.5 years, and is scheduled to end in Dec., 2010. This CRADA project focused on addressing the wear and failure modes of current on-highway heavy-duty diesel exhaust valves and seats, and then evaluating changes in valve-seat design or selection of advanced alloys, which will then enable higher temperature capability, as well as better performance and durability. The CRADA was extended for 12 more months due to technical success during the 2nd year of the project. It will be extended further this year, due to the need to generate new creep-data and wear-test new prototype valves made of new Ni-based superalloys with more temperature capability. Requests for more detailed information on this project should be directed to Caterpillar, Inc.

Highlights

Caterpillar, Inc.

Caterpillar completed testing of J3 alloy seat-inserts with modified process and determined that both short- and long-term benefits are measureable. Caterpillar has requested seat-inserts to match with the new prototype valves that will be delivered to Caterpillar for testing to indicate higher temperature capability.

ORNL

ORNL placed a subcontract with the valve maker to produce tensile/creep specimens for testing at ORNL, and to forge and heat-treat new prototype exhaust valves from the new Ni-based superalloys for testing at Caterpillar, to demonstrate more temperature capability and performance than the standard alloy 31V.

Technical Progress, 1st Quarter, FY2010

Background

This OVT Agreement 16304 is an ongoing ORNL CRADA project with Caterpillar, NFE-07-00995, which will last for about 3.5 years, after last-year's 1 year extension. This CRADA project has addressed the wear and failure modes found for current on-highway heavy-duty diesel exhaust valves and seats. It then identified changes in valve-seat advanced alloys that will enable higher temperature capability, as well as better performance and durability. The need for such upgraded valve-seat alloys is driven by the demands to meet new emissions and fuel economy goals which continue to push diesel exhaust component temperature higher. The CRADA was scheduled to be

complete at the end of 2009, but has been extended for 12 more months, due to outstanding technical progress and success. Requests for more detailed information on this project should be directed to Caterpillar, Inc.

Approach

Caterpillar provides the baseline wear and mechanical behavior characteristics of engine-exposed standard valves and seats, and provides exposure of similar components from simulation-rig testing at Caterpillar. ORNL provides more in-depth characterization and microcharacterization of those valves and seats, and provides knowledge and understanding of the full range of commercially available heat-resistant alloys, to select those most suitable for upgraded valve performance. ORNL and Caterpillar have developed an understanding of the underlying degradation mechanisms, which is the technical basis for selecting and testing alternate valve and seat alloys with upgraded performance and temperature capability. Caterpillar and ORNL are working with Caterpillar's various component and materials suppliers, to enable parallel prototype production of upgraded exhaust valves and seats for evaluation in Caterpillar's wear-test rig, and test specimens of the same advanced alloys for ORNL to test and characterize.

Technical Progress – Caterpillar, Inc.

This quarter, Caterpillar completed "Buettner-Rig" testing of seat-inserts with modified processing for wear-resistance, and determined the longer-term benefits.

Caterpillar initiated a project with a major valve supplier to obtain heats of two advanced, alternate Ni-based superalloys for forging into upgraded exhaust valves. These new alloys should have improved performance and higher temperature capability than the standard 31V alloy. Last quarter, the team finalized the mechanical testing and characterization of specimens at the valve supplier and at ORNL, and for prototype exhaust valves for testing and evaluation in the wear-test rigs at Caterpillar.

Technical Progress – ORNL

Last quarter, ORNL received a set of J3 alloy exhaust-valve seat-inserts with two different processing modification treatments for improved wear-resistance. Microstructural characterization of those seats was completed at ORNL this quarter.

ORNL placed a sub-contract with Caterpillar's exhaust valve supplier to forge new valves and to make various mechanical properties test specimens from two alternate Ni-based alloys with more temperature capability and performance than the standard 31V alloy. ORNL received some of the test specimens, and began elevated temperature tensile and creep testing this quarter.

Communications/Visits/Travel

Detailed team communications between ORNL and Caterpillar occur regularly in multi-party conference calls. Caterpillar has extended team discussions to include their commercial seat-insert supplier as well as one of their exhaust valve suppliers.

ORNL visited the Caterpillar Technical Center (Peoria, IL) to review this project with Caterpillar management on November 17th, 2009, and set goals for next year.

Status of Milestones (ORNL for DOE)

Milestones for Caterpillar rig-testing of prototype valves and seats of new advanced alloys are on schedule for FY 2010.

Publications/Presentations/Awards

None

Agreement 17257: Materials for Advanced Turbocharger Designs

P.J. Maziasz and A. Shyam
Oak Ridge National Laboratory
and
P. Pattabiraman
Honeywell Turbo Technologies

Objective/Scope

This is a new ORNL CRADA project with Honeywell, NFE-08-01671 (DOE/EERE/OVT Agreement 17257), that began in August, 2009, and is scheduled to last for about 3 years. This CRADA project will address the limitations of lifetime or use-temperature for the various components (casing, wheel, shaft, bearings) of both the turbine and compressor parts of the turbocharger system. The increase in exhaust temperatures provides higher engine efficiency and lower emissions and also increases turbocharger component temperatures. The need for most heat-resistant materials must, therefore, be addressed. Requests for more detailed information on this CRADA project should be directed to Honeywell, Inc.

Highlights

This is a new project this quarter.

Technical Progress, 1st Quarter, FY2010

Background

This new CRADA project, which began at the end of FY2009, will extend for 3 years, and cover several different tasks. The first will be to assess and prioritize the various components that need or would most benefit from materials upgrades to increase temperature capability and performance, as well as durability and reliability. The next tasks will examine current performance and degradation modes of wheel/shaft assemblies for turbines and compressors, housings for turbines and compressors, and bearings. We will then obtain and test new materials with upgraded performance, and provide the results to Honeywell for designing advanced turbocharger systems and to manufacture new prototype components for testing and evaluation.

Approach

This new CRADA project began at the beginning of August, 2009, and is comprised of six tasks, which will span the 3 year duration of this project. Activity began with ORNL and Honeywell discussing the priority of the various turbocharger components for materials upgrades.

The turbine wheel-shaft assembly was chosen as the first component for consideration, with analysis of residual stresses near the weld-joint of the Ni-based superalloy wheel to the steel shaft being the focus. This new CRADA project also continues previous work between ORNL and Honeywell on testing of the new CF8C-Plus cast stainless steel as

a significant performance upgrade for the turbine housing relative to standard SiMo cast iron.

Figure 1 shows a typical Honeywell turbocharger system used for passenger vehicle engine applications. It is cut-away, so that the internal rotating components (wheels, shaft) for the turbine (hot-end) and compressor (cold-end) can be seen. Figure 2 shows some results from previous work by ORNL and Honeywell comparing the new CF8C-Plus steel to HK30-Nb, a standard commercially available upgrade material for turbochargers for heavy-duty truck diesel engines when temperatures exceed the limitations of SiMo cast iron. For comparison of elevated temperature tensile properties at 600-800°C, CF8C-Plus cast stainless steel has similar yield-strength at 700°C, and higher strength at 800°C than HK30-Nb stainless steel. One task of this new CRADA project for turbine housings will continue this work for a broad range of other high temperature properties, including creep and fatigue strength, and expand it to turbine housing applications for passenger vehicle gasoline engines.

.

Figure 1 – Typical Honeywell turbocharger system for passenger vehicles. Cut-away shows turbine wheel inside the cast-iron casing (nearest end) of the turbine end, an aluminum housing on the compressor side, and the transition region in between, containing the steel shaft connecting both wheels and bearings.

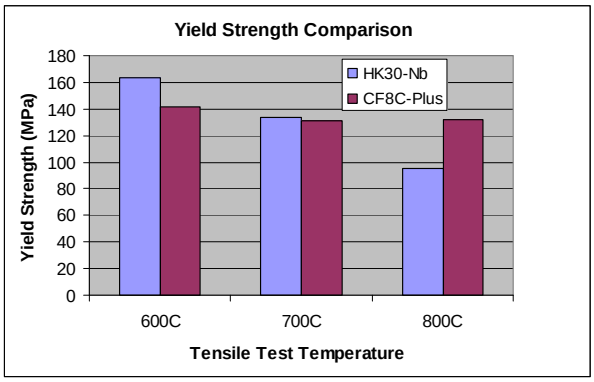

Figure 2 – Comparison of yield strength (YS) measured by elevated temperature tensile testing of both cast CF8C-Plus and cast HK30-Nb austenitic stainless steels. While the HK30-Nb has slightly higher YS at 600°C, both materials have similar strength at 700°C, and the CF8C-Plus steel is stronger at 800°C.

Technical Progress

For Task 3, ORNL continued several of the CF8C-Plus steel creep-rupture tests that were stopped during the previous CRADA project. ORNL also machined new tensile/creep specimens of CF8C-Plus steel to fill in the data gaps for selected high-temperature tensile and creep-rupture tests. Honeywell also prioritized taking the steps necessary to commercially produce some prototype turbocharger housing using CF8C-Plus steel for certain turbocharger models, to that they could be evaluated and tested.

For Task 1, Honeywell identified neutron-scattering experiments to measure residual stresses in welded wheel/shaft assemblies as one of their highest priority items. Efforts began to define these experiments, and to request neutron scattering time at the HFIR Residual Stress User- Facility this quarter.

Communications/Visits/Travel

A team from ORNL visited Honeywell Turbo Technologies in Torrance, CA on 13-15 October, 2010 for a Kick-Off Meeting on CRADA NFE-08-01671. The visit included Jerry Gibbs, the Program Manager of Propulsion Materials from DOE/EERE/OVT, who overviewed DOE program opportunities and priorities, and indicated where advanced turbocharger technology fit in with the engine efficiency and emissions goals of the program. Data on creep and fatigue of CF8C-Plus steel from the prior DOE/EERE CRADA project were reviewed and discussed. Work for this new CRADA project for next year was also discussed and prioritized.

Status of Milestones (ORNL for DOE)

None, new project this quarter.

Publications/Presentations/Awards

None

Agreement 17894: NDE for ACERT Engine Components

J. G. Sun and J. A. Jensen*
Argonne National Laboratory
***Caterpillar, Inc.**
Technical Center

Objective/Scope

Applications of advanced materials in diesel engines may enhance combustion and reduce parasitic and thermal losses, thereby improving engine efficiency. Engine components developed from advanced materials, however, require rigorous assessment to assure their reliability and durability in more stringent operating conditions. The objective of this work is to develop and assess various nondestructive evaluation (NDE) methods for characterization of advanced engine components in a Caterpillar heavy-duty ACERT experimental engine at ORNL. NDE technologies established at ANL, including optical scanning, infrared thermal imaging, ultrasonics, and x-ray CT, will be further developed for detection of volumetric, planar, and other types of flaws that may limit the performance of these components. NDE development will be focused on achieving higher spatial resolution and detection sensitivity. Current efforts are directed in applications of optical methods for valvetrain components, x-ray and ultrasonic for joinings, and thermal imaging for thermal barrier coatings (TBC).

Technical Highlights

Work during this period (October-December 2009) focused on continued thermal imaging NDE analysis for TBC specimens received from Caterpillar, Inc.

1. Thermal Imaging NDE for Thermal Barrier Coatings

During this period we continued to optimize experimental and data-processing parameters for reliable and accurate thermal tomography characterization of TBC specimens. The parameters that affect the tomography results include the flash duration of the flash lamps, the amount of heat absorbed on TBC surface, and the data acquisition speed. A finite flash duration, typically in the range of 1-2ms, can usually be modeled and corrected from the theoretical solution based on the ideal instantaneous flash assumption. The flash duration only affects the early time period of a transient measurement. In the tomography result, its effect appears within the top few slices of the coating layer and has been observed in the previous results (April-June 2009 report). Therefore, it is necessary to correctly account for the flash duration effect in order to generate accurate NDE results for the coating layer. By adjusting the flash duration parameter, better results were obtained as compared to those reported earlier. This is demonstrated using the as-processed TBC specimen #10 shown in Fig. 1a. Comparing the 5 plane slices of the coating layer obtained earlier with a 2ms flash duration in Fig. 2a and now with a 0.8 ms duration in Fig. 2b, there is a considerable improvement in image quality in the first three layers, although the difference is not very apparent in the two deeper layers. More importantly, the coating layer becomes more distinct with a uniformly lower effusivity in the new data (Fig. 3b) as seen from the cross-sectional slices in Fig. 3.

(a) (b)

Fig. 1. Photographs of TBC specimen #10 with (a) as-received and (b) a black-painted surface.

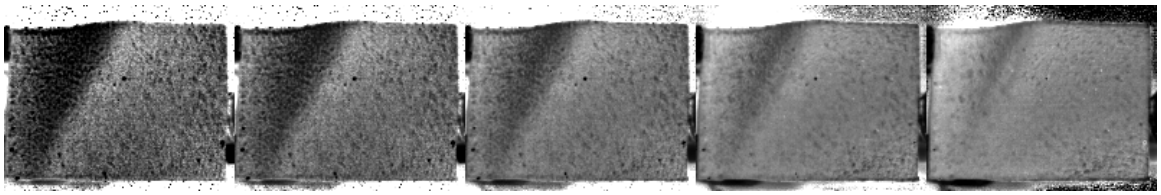

Slice #1 Slice #2 Slice #3 Slice #4 Slice #5

(a)

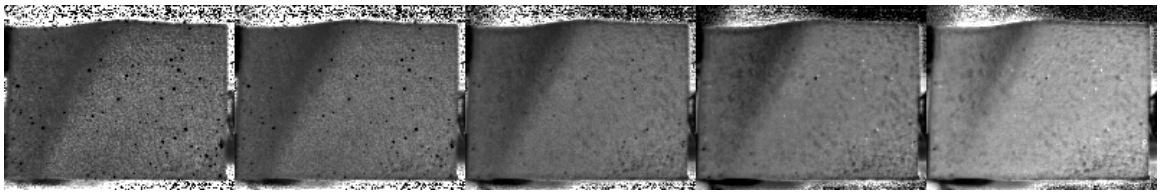

Slice #1 Slice #2 Slice #3 Slice #4 Slice #5

(b)

Fig. 2. Plane slices of the coating layer for TBC specimen #10 obtained with (a) 2.0ms and (b) 0.8ms flash duration parameter.

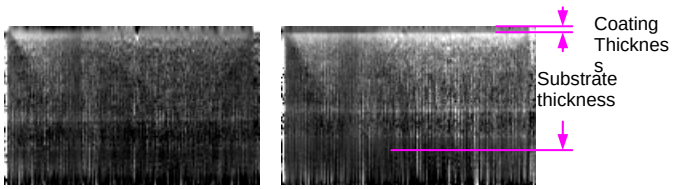

(a) (b)

Fig. 3. Cross-section slices for TBC specimen #10 obtained with (a) 2.0ms and (b) 0.8ms flash duration parameter.

Because the surface of as-processed TBCs has high optical reflection, there was a concern that heat absorption on TBC surface during thermal imaging test was not sufficient to produce accurate thermal tomography results. For as-processed TBC #10, the maximum temperature on coating surface during the flashing time was found to be <5°C, which is significantly lower than an adequate heating level. As a result, the noise in the tomography results (Figs. 2-3) is higher especially in deeper substrate layers. A solution to improve the heating efficiency is to apply a graphite-based black paint on the coating surface. The black paint is typically 1-2µm thick and can be easily burn off at ~700°C within a short time. To assess the effectiveness of the black paint, and also to verify the result obtained without the paint, half of the TBC #10 surface was painted as

shown in Fig. 1b. The experiment was conducted at a higher data-acquisition speed of 1905Hz in order to increase the depth resolution for the coating and substrate. With the black paint, the maximum surface temperature during the flashing period was found to be >32°C, a significant improvement in heat absorption efficiency.

Figure 4 shows plane and cross-sectional slices derived from the thermal-imaging data obtained with high-speed acquisition and on black-painted surface of the as-processed TBC #10. From the cross-section image in Fig. 4b, the coating layer has a distinct lower thermal effusivity and a thickness represented by 7 plane slices. Accordingly, Fig. 4a shows the plane coating slices (F1-7) and substrate slices (F8-14) that are just below the interface. By comparing the cross-sectional slices in Fig. 3 and Fig. 4b obtained respectively from the same TBC surface without and with paint, the painted surface resulted in a significantly improved image quality. This is represented by a uniform coating and substrate effusivity as well as a sharp interface as seen in Fig. 4b, all due to a higher heat absorption by the black surface.

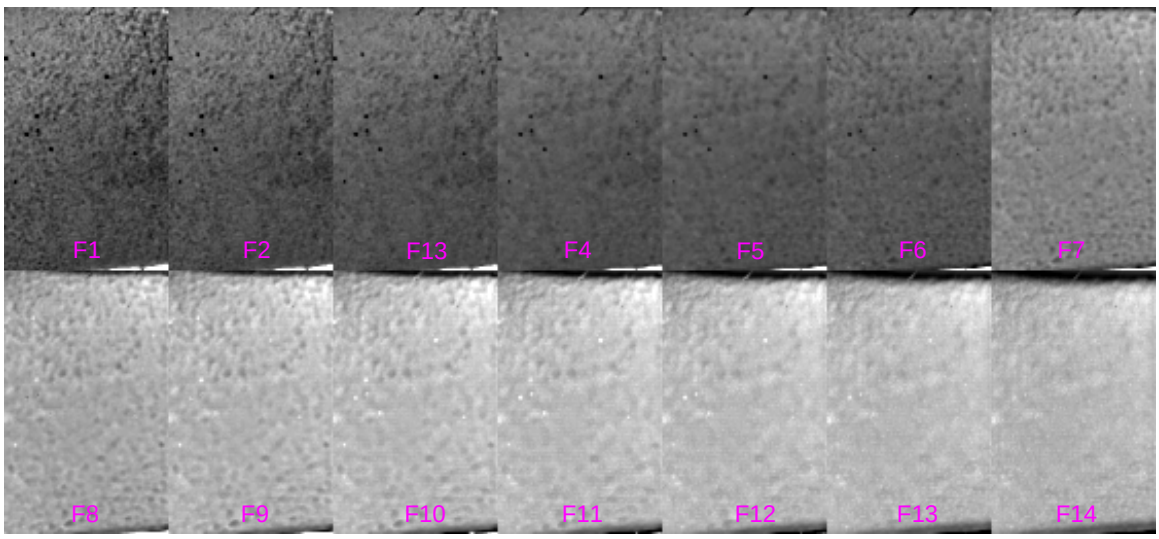

Fig. 4a. Plane slices within the coating (F1-7) and substrate (F8-14) layer for TBC specimen #10 with a black paint on surface.

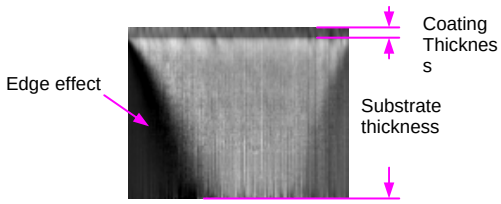

Fig. 4b. A typical cross-section slice for TBC specimen #10 with a black paint on surface.

Although a black paint may improve the result, it is normally undesirable to paint the TBC surface. Under such conditions, thermal imaging must be performed on natural TBC surface, and the reliability and accuracy of the acquired data have to be assured. To address this issue, the plane slice near the interface, which is the slice #5 in the unpainted data (Fig. 5a) and slice #7 in painted data (Fig. 5b), are examined to

determine if the same result is obtained. Because TBC #10 is a “good” sample, the only features to be compared are the darker spots corresponding to the surface bumps. From Fig. 5, it is evident that the number and distribution of the darker spots are essentially the same in both images. The slight difference in spot sizes and scales is due to focusing and data-acquisition speed. Therefore, it is concluded that thermal imaging can reliably examine coating and interface conditions for natural TBCs that may have high surface reflections. The only problem is when it is necessary to inspect the deeper substrate condition, which however is normally uniform and unimportant for almost all TBC samples.

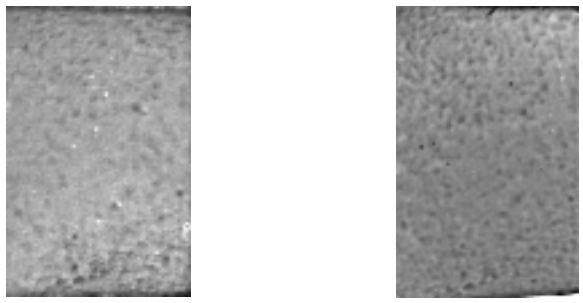

(a) (b)

Fig. 5. Comparison of plane slice at interface obtained (a) without and (b) with black paint on TBC specimen #10 as shown in Fig. 1.

The new flash duration parameter was also used to construct new thermal tomography results for as-processed and thermal-cycled TBC #9 using the previously acquired thermal-imaging data. The new results also showed better resolution for features in the shallow coating depths, which is particularly important for identifying shallow delaminations in the thermal-cycled coating. Figure 6 shows the plane slices of the coating layer in thermal-cycled TBC specimen #9. The images were scaled brighter to better reveal the delaminations which are displayed with darker grayscales corresponding to lower effusivities. As indicated in Fig. 6, some shallow delaminations are observed at the top-right region in slice #1; they disappear at slices deeper than #2. Within a large rectangular area at the left side, many individual delamination spots emerge at deeper depths, mostly in slices >#3. At the right side of the sample, there is almost no delamination. This area shows a darker brownish color on surface (see inserted photograph). As explained in the 2009 annual report for this project, a brown surface color indicates that the coating on the surface has already been spalled. These results in Fig. 6 therefore clearly demonstrate that thermal tomography can easily detect delaminations and resolve their size and depth distributions. Further improvement for delamination depth resolution can be achieved by using higher data-acquisition speed and black paint on thermal-cycled TBC surfaces.

To verify the thermal tomography results, it is necessary to correlate the detected delaminations with actual ones within the coating. This is relatively easy for delaminations in these TBCs because they are raised above the surface and many have cracks in their center, as seen in the photomicrograph in Fig. 7. However, because the pixel size in thermal imaging data for TBC #9 is large at ~0.2mm, it is challenging to match individual delaminations in the thermal imaging data and in the surface micrograph. Optical methods such as laser backscatter have better spatial resolution

than thermal, so can be used to detect small delaminations. Effort to obtain a detailed correlation of detected delaminations by thermal and optical methods with actual ones in the coating is continuing and will be presented in next report.

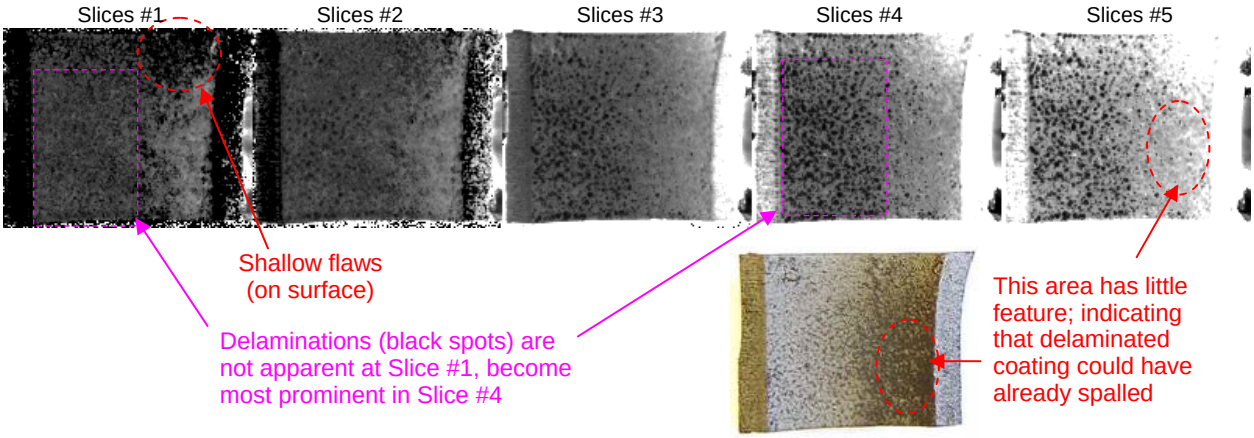

Fig. 6. Characterization of delamination depth and distribution in thermal-cycled TBC #9.

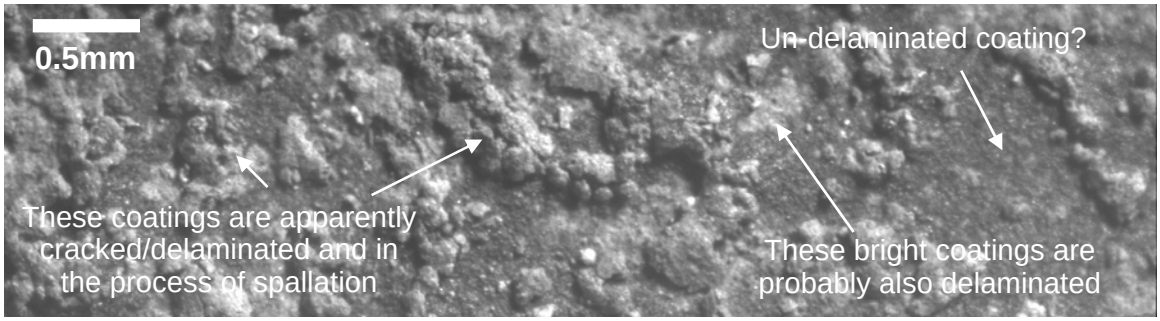

Fig. 7. Photomicrograph of the surface of thermal-cycled TBC #9.

Status of Milestones

Current ANL milestones are on schedule.

Communications/Visits/Travel

J.G. Sun visited Caterpillar Tech Center on Nov. 18, 2009 to discuss program matters.
J.G. Sun plans to attend the 34th International Conference and Exposition on Advanced Ceramics and Composites, Daytona Beach, FL, January 24-29, 2010.

Problems Encountered

None this period.

Publications

J.G. Sun, "Measurement of Thermal Barrier Coating Conductivity by Thermal Imaging Method," in Ceramic Eng. Sci. Proc., eds. D. Singh and J. Salem, Vol. 30, no. 3, pp. 97-104, 2009.

J.G. Sun, "Depth Deconvolution Algorithm for Thermal Tomography," Argonne National Laboratory Invention Report Number IN-09-081, reported to DOE on Dec. 2, 2009.

Agreement 18570: Engine Materials Compatibility with Alternative Fuels (EMCAF)

S. J. Pawel
Oak Ridge National Laboratory

Objective/Scope

The purpose of this Cooperative Research and Development Agreement (CRADA) between Oak Ridge National Laboratory and USCAR is to systematically evaluate compatibility between engine materials and ethanol fuel blends over a range of temperatures from ambient to elevated temperatures consistent with engine operation. Four primary tasks are included in the overall program:

1) surface analysis of materials exposed in field and lab exposures
2) in-situ extraction of gas and/or fluid from the valve seat crevice
3) development of electrochemical testing protocols
4) laboratory corrosion exposures of coupon materials

Technical Highlights

Initial efforts have been made to demonstrate a proof-of-principle device for sampling of gas/fluids in the valve seat crevice (task 2). A cylinder head provided by the partners was sectioned and a small diameter hole (to accommodate a 320 µm diameter tube) drilled from behind the intake to the gap between the head and valve seat. Initial tests to withdraw water from this area were successful. Figure 1 provides a picture of the initial proof-of-principle device.

Status of FY2010 Milestones

Work initiated.

Communications/Visits/Travel

With the CRADA being signed in late November, a kick-off meeting was held in December at the USCAR Headquarters in Southfield, MI. Representatives from ORNL (five Team members) and representatives of the USCAR Partners (ten Team members) as well as the DOE Sponsor met to review the CRADA requirements, discuss information protection, and plan the immediate path forward.

Problems Encountered

none

Publications/Presentations/Awards

none

References

none

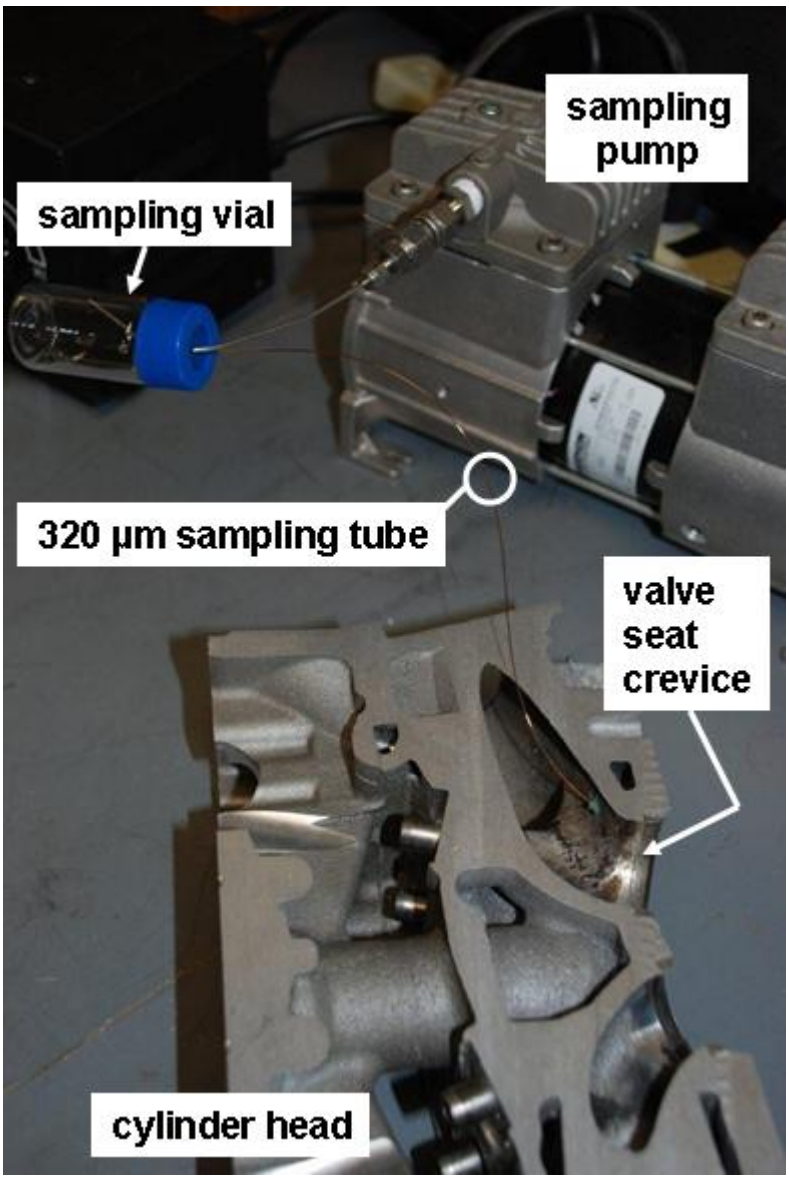

Figure 1. Proof-of-principle device for sampling gas/liquid from the valve seat crevice.

Agreement 18571: Materials Issues Associated with Exhaust Gas Recirculation Systems

M. J. Lance, C. S. Sluder and J. M. E. Storey
Oak Ridge National Laboratory

Objective/Scope

Provide information to industry specialists about fouling deposit properties so as to enable improved models and potential design improvements to reduce fouling and its impact on the performance of EGR (exhaust gas recirculation) coolers.

Technical Highlights

Samples are currently being images with neutron tomography. Figure 1 shows four clean EGR tube sections that were images so as to collect a baseline. Steel is transparent to neutrons whereas hydrogen is a strong neutron scatterer so it is hoped that neutron tomography will provide a powerful non-destructive method of collecting images hydrocarbon/soot deposits in EGR coolers. Images of soot-loaded industry-provided samples are currently being collected at HFIR but were not ready for this report.

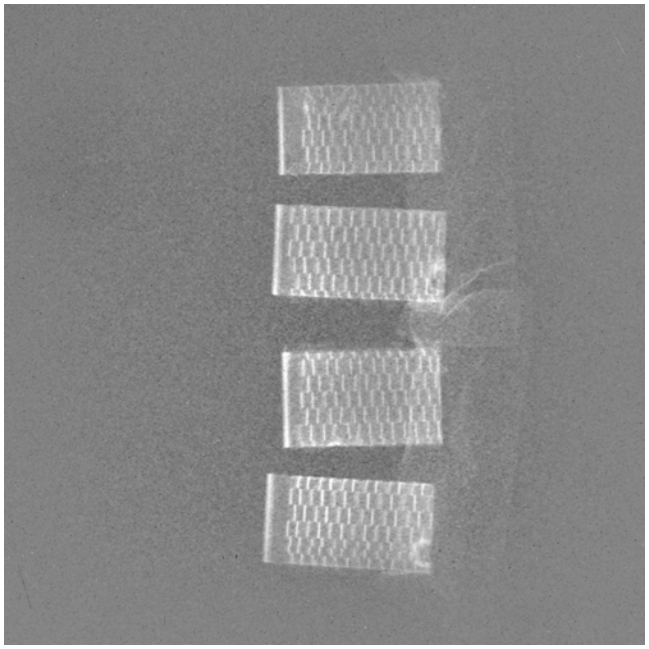

Figure 1. Neutron images of clean (no soot) sections of an industry-provided EGR cooler tube.

Chemical characterization of industry provided coolers has continued with recent GC-MS measurements conducted at NTRC. Results have tended to support previous TGA/DTA measurements that showed higher hydrocarbon content with increasing deposit mass. In addition, mechanical properties measurements have been attempted by indenting a laboratory-generated deposit with a 2 mm diameter punch. Using a high resolution load cell, a load could be measured on the deposit prior to compressing it.

Future measurements will be conducted as a function of temperature in order to see if the mechanical properties of the deposit change during EGR operation.

A tenth company has been added to the EGR advisory board and they have provided a cooler tube for analysis. This tube has undergone the same suite of characterization techniques used on previous coolers.

Status of FY2010 Milestones

Complete chemical and microstructural characterization of industry provided coolers. (09/10) *On Schedule.*

Communications/Visits/Travel

None.

Problems Encountered

None.

Publications/Presentations/Awards

None.

References

None.

Agreement 19202: Titanium Friction and Wear
(Surface Engineering of Bearing Components)

Peter Blau
Oak Ridge National Laboratory

Objective/Scope

Energy efficiency and durability of internal combustion engines (ICEs), whether fueled by conventional or alternative fuels, benefits from the utilization of lightweight materials. Examples include fiber composites and alloys of aluminum, magnesium, or titanium. While such materials offer attractive efficiency gains, their use presents certain technical and economic challenges. The nature of those challenges depends upon which materials and engine components are involved. One class of applications involves tribological applications: that is, those which concern friction, wear, and lubrication. Studies by engine research groups in the United States, Japan, and the United Kingdom have shown that mechanical losses comprise about fifteen percent of the energy dissipation from fuel in a typical ICE, and that of those, energy losses by friction comprise about eighty percent. Considering subsystems, the two major contributors to engine frictional losses are the piston ring/cylinder interface and the engine bearings. Past work at ORNL and a number of other laboratories have addressed materials and lubrication-related aspects of the first contributor. The current project, beginning in FY 2010, addresses the second contributor: connecting rod bearings.

The objective of this project is to enable the use of lightweight titanium alloys in connecting rods (CRs) by applying integrated surface-engineering methods and in situ-formed deposits to effect significant improvements in the lubricity and durability of bearing surfaces at both the piston end and the large (crankshaft) end of the CR. Current practice typically uses inserts at both ends, but the goal of this effort is to develop and test surface engineering methods that allow the Ti surfaces to be used effectively without the need for additional bearing inserts. It capitalizes on recent developments in titanium processing technology to reduce material cost, and the capabilities of ORNL to effect changes in the surface-critical properties of metals and alloys through a variety of treatment routes. In order to fairly evaluate the effectiveness of these methods, a spectrum load-actuated tribo-testing system will also be developed. The final stage of this project involves proof-of-concept tests on either motored or fired engines.

Technical Highlights

This is the first project quarterly report. Therefore, an initial overview and plan for this effort is provided.

Background and initial progress. The connecting rods in an internal combustion engine are among the most highly-stressed components. A schematic diagram of a typical connecting rod (CR) design and its principal parts is shown in Figure 1. Forces from the combustion chamber must be transmitted through the connecting rod to rotate the engine main shaft with minimal frictional losses or wear of the bearings. Due to the firing cycle and inertia of the system, the radial bearing loads at the ends of the CR vary significantly as the crank rotates and as a function of engine speed. Owing to this

geometric arrangement, small-end bearings exhibit different load histories than big-end bearings. So-called ‘polar load diagrams’ are used by engine designers to display the directions and magnitudes of forces relative to the center of rotation. Further information and examples of this method are available in references such as the book by Taylor [1].

Current diesel engines use forged alloy steel connecting rods with metallic bearing inserts to control friction against the crankshaft and piston wrist pin at the small-end, respectively. If strong, corrosion-resistant titanium (Ti) alloys were to cost-effectively replace alloy steel in connecting rods, engine weight could be reduced to increase fuel efficiency. Furthermore, if the bearing openings at the ends of the lightweight Ti CRs could be surface engineered to perform durably and be compatible with current engine lubricants, Ti alloy connecting rods could be used without the need for inserts or cast-in end-bearings, like the current bronzes or lead-based Babbitt alloys that were used. Integral bearing surfaces would reduce the number of parts, avoid thermal expansion mismatch with inserts, and reduce manufacturing complexity. Furthermore, Ti is an extremely corrosion resistant metal, and that would provide additional benefits in durability.

Currently, a number of companies, many of them specialty machine shops, offer Ti alloy CRs to the high-performance and racing markets. These products tend to be extremely pricey, some costing as much as US$ 1500 for one rod. The development of low-cost raw materials and mass production manufacturing processes therefore becomes key if Ti CRs are to be widely introduced. For bearings, Ti alloy CRs usually employ inserts or hard metal coatings. However, the current project focuses on the technology to enable Ti surfaces to serve as plain bearing surfaces without mechanical inserts.

As mentioned earlier, the combination of cylinder pressure and the inertia of the rotating components, the bearings on a connecting rod witness widely-changing normal loads (see for example, Fig. 2, using data from Taylor [1]). That behavior causes the surfaces to experience more than one lubrication regime as the engine runs (hydrodynamic, mixed-film, and boundary lubrication). Thus, the lubricant film thickness and surface coverage varies, and there is no steady-state of tribocontact. During some portions of bearing rotation, the materials may come into direct contact under boundary lubrication conditions. The solid surfaces must be protected during such times, and bare Ti is inadequate. Past DOE-sponsored research at ORNL and elsewhere has shown that bare titanium alloys exhibit poor frictional characteristics [2]. They tend to scuff and gall [3]. Surface treatments, like oxygen diffusion, surface patterning, and nano-compositing offers the potential to reduce these deleterious effects. Significantly, certain oxygen diffusion treatments [4] enable Ti to be lubricated by conventional engine oils despite the fact that the oils were originally formulated for use with ferrous-based surfaces. In addition, friction-reducing patterned surfaces and in situ-formed composite surface layers offer other options.

Year one will develop testing methodology and use it to downselect viable surface treatment compositions and processes. Year two will focus on optimizing micro-topography conjointly with compositional surface modification. Year three will apply an

integrated surface design approach to demonstrate friction and wear performance of proto-typical titanium connecting rods in motored or fired engines.

Progress. During the first quarter of this new project, a literature survey was initiated to establish the state of the art in surface treatments for titanium alloys. Information on the loads and motions of connecting rods was also gathered. Most tribology references concerned aerospace applications of titanium, like turbine blades and discs, where the focus is on fretting wear (high-frequency, low amplitude vibrations). Published studies of titanium subjected to sliding wear and friction do exist, but are much less common. Therefore, the initial phases of this work will generate baseline data on non-treated Ti and cast iron, and will be a benchmark for comparing improvements in the early phases of this work. An ASTM reciprocating test method (G 133, Ref. [5]), developed at ORNL under support from the DOE Ceramic Technology Project of the 1980s and 1990s, will be used for preliminary screening work. While this method was aimed at piston ring/liner configurations, the big-end bearing also experiences variable motions under boundary lubrication. Therefore, a more simulative procedure, more analogous to plain bearing geometry and motions will be developed. This spectrum load actuated tribotester will be used to evaluate promising surface engineering approaches under non-steady-state loading conditions simulative of engine bearings.

Future Plans. In the upcoming quarter, plans include two tasks. (1) Titanium alloy materials will be obtained and used to establish baseline friction and wear data under diesel oil-lubricated conditions, using the ASTM G 133 reciprocating sliding test. In particular, we will explore the effects of new and used oils on friction and wear of Ti alloys. Prior ORNL data on cast iron will be used for comparison, but bronzes may also be included. (2) The preliminary design concept for a spectrum load actuated tribotester will be developed.

Status of FY 2010 Milestones

Design friction and wear testing apparatus to simulate connecting rod motions, loads, and speeds, and complete a series of baseline experiments on small test coupons of candidate titanium alloys, with and without surface treatments. **(09/10)**

Communications/Visits/Travel

None

Problems Encountered

None

Publications/Presentations/Awards

None

References

[1] C. M. Taylor, ed. (1993) *Engine Tribology*, Elsevier Tribology Series Vol. 26, Elsevier Pub. (UK).

[2] J. Qu, P. J. Blau, and N. S. Kulkarni (2005) “Unusual Sliding Friction and Wear Behavior of Titanium Alloys against Metal, Polymer, and Ceramic Counterfaces,” *Wear*, Vol. 258, No. 9, Apr. 2005, pp. 1348-1356.

[3] P. J. Blau, D. L. Erdman III, E. Ohriner, and B. C. Jolly (2010) “High-Temperature Galling Characteristics of Ti-6Al-4V with and without Surface Treatments,” accepted for presentation, Soc. of Tribologists and Lubrication Engineers Annual Meeting, Las Vegas, NV, May 16-20.
[4] J. Qu, P. J. Blau, J. Y. Howe, H. M. Meyer III (2009) “Oxygen diffusion enables anti-wear boundary film formation on titanium surfaces in zinc-dialkyl-dithiophosphate (ZDDP)-containing lubricants,” *Scripta Materialia*, Vol. 60 (10), pp. 886-889.
[5] ASTM G133, *Standard Test Method for Linearly-Reciprocating Ball on Flat Sliding Wear*, ASTM Annual Book of Standards, Vol. 03.02 (2008), ASTM International, West Conshohocken, PA, pp. 551-559.

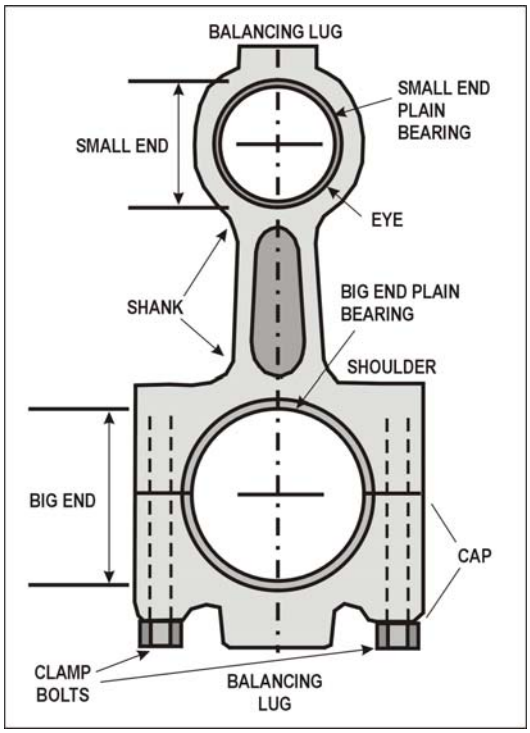

Figure 1. Features of a typical connecting rod in a diesel or spark ignition ICE. Details vary depending on the type of engine.

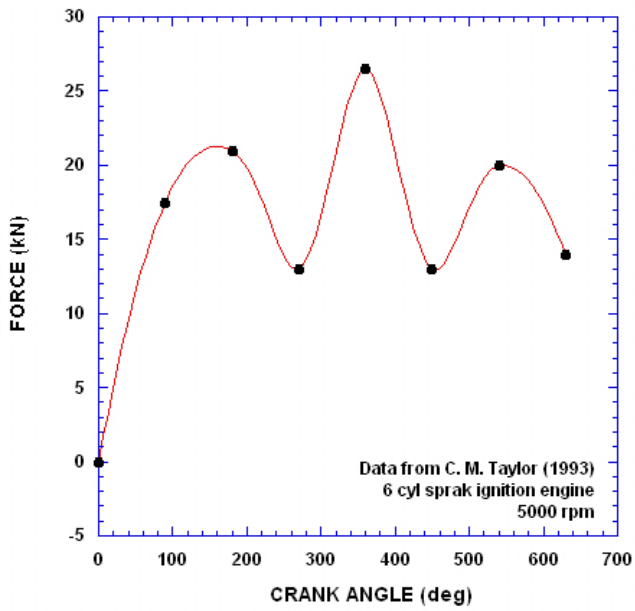

Figure 2. Variation of normal forces on a big-end bearing as the crank shaft rotates. Forces higher than 27,000 N occur during a portion of the cycle. [Data extracted from a polar force diagram in C. M. Taylor, *Engine Tribology* (1993), Elsevier Pub., UK.]

Agreement 10635: Catalysis by First Principles - Can Theoretical Modeling and Experiments Play a Complimentary Role in Catalysis?

C. Narula, M. Moses DeBusk, Xiaofan Yang
Oak Ridge National Laboratory

Objective/Scope

This research focuses on an integrated approach between computational modeling and experimental development, design and testing of new catalyst materials, that we believe will rapidly identify the key physiochemical parameters necessary for improving the catalytic efficiency of these materials. The results will have direct impact on the optimal design, performance, and durability of supported catalysts employed in emission treatment; e.g., lean NO_x catalyst, three-way catalysts, oxidation catalysts, and lean NO_x traps etc.

The typical solid catalyst consists of nano-particles on porous supports. The development of new catalytic materials is still dominated by trial and error methods, even though the experimental and theoretical bases for their characterization have improved dramatically in recent years. Although it has been successful, the empirical development of catalytic materials is time consuming and expensive and brings no guarantees of success. Part of the difficulty is that most catalytic materials are highly non-uniform and complex, and most characterization methods provide only average structural data. Now, with improved capabilities for synthesis of nearly uniform catalysts, which offer the prospects of high selectivity as well as susceptibility to incisive characterization combined with state-of-the science characterization methods, including those that allow imaging of individual catalytic sites, we have compelling opportunity to markedly accelerate the advancement of the science and technology of catalysis.

Computational approaches, on the other hand, have been limited to examining processes and phenomena using models that had been much simplified in comparison to real materials. This limitation was mainly a consequence of limitations in computer hardware and in the development of sophisticated algorithms that are computationally efficient. In particular, experimental catalysis has not benefited from the recent advances in high performance computing that enables more realistic simulations (empirical and first-principles) of large ensemble atoms including the local environment of a catalyst site in heterogeneous catalysis. These types of simulations, when combined with incisive microscopic and spectroscopic characterization of catalysts, can lead to a much deeper understanding of the reaction chemistry that is difficult to decipher from experimental work alone.

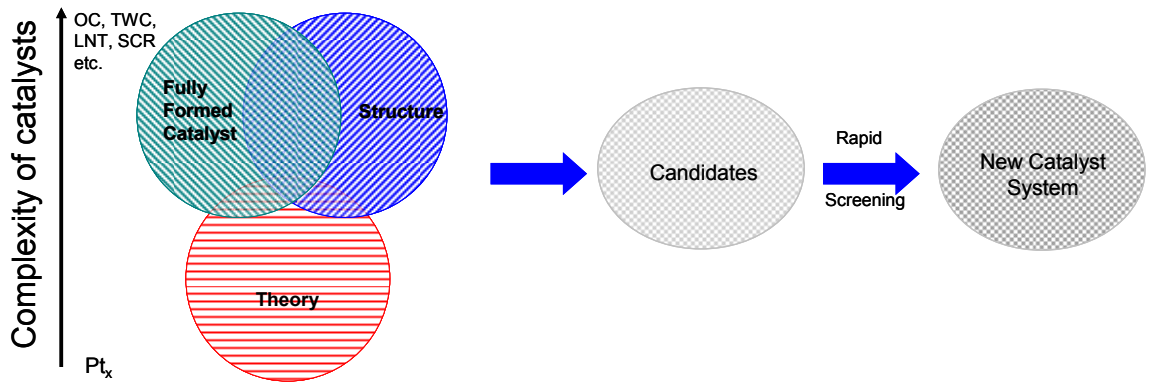

Thus, a protocol to systematically find the optimum catalyst can be developed that combines the power of theory and experiment for atomistic design of catalytically active sites and can translate the fundamental insights gained directly to a complete catalyst system that can be technically deployed.

Although it is beyond doubt computationally challenging, the study of surface, nanometer-sized, metal clusters may be accomplished by merging state-of-the-art, density-functional-based, electronic-structure techniques and molecular-dynamic techniques. These techniques provide accurate energetics, force, and electronic information. Theoretical work must be based on electronic-structure methods, as opposed to more empirical-based techniques, so as to provide realistic energetics and direct electronic information.

A computationally complex system, in principle, will be a model of a simple catalyst that can be synthesized and evaluated in the laboratory. It is important to point out that such a system for experimentalist will be an idealized simple model catalyst system that will probably model a “real-world” catalyst. Thus it is conceivable that “computationally complex but experimentally simple” systems can be examined by both theoretical models and experimental work to forecast improvements in catalyst systems.

We have focused on the oxidation catalyst to develop and demonstrate catalyst by design protocol as a prelude to developing catalyst by design protocols for complex emission treatment catalysts; e.g., TWCs, NO_x traps, and HC-SCR catalysts. Our Goals are as follows:

- Our theoretical goal is to carry out the calculation and simulation of realistic supported Pt nanoparticle systems (i.e., those equivalent to experiment), in particular by addressing the issues of complex cluster geometries on local bonding effects that determine reactivity. As such, we expect in combination with experiment to identify relevant clusters, and to determine the electronic properties of these clusters.
- Our experimental goal is to synthesize metal carbonyl clusters, decarbonylated metal clusters, sub-nanometer metal particles, and metallic particles (~5 nm) on alumina (commercial high surface area, sol-gel processed, and mesoporous molecular sieve), characterize them employing modern techniques including

Aberration Corrected Electron Microscope (ACEM), and evaluate their CO, NO_x, and HC oxidation activity.

- This approach will allow us to identify the catalyst sites that are responsible for CO, NO_x, and HC oxidation. We will then address support-cluster interaction and design of new durable catalysts systems that can withstand the prolonged operations.

Technical Highlights

Our theoretical studies on single platinum atoms supported on θ-alumina slab shows that the platinum atom is in zero oxidation state. This result is very different from that reported in literature on single platinum atoms supported on α-alumina or simplified models of γ-alumina where a platinum atom generally has an unpaired electron. This also means that mechanism of CO, NO_x, or HC oxidation on Pt(0) will be different from that on Pt(I) or Pt(II). We plan to carry out first principle studies of CO oxidation on Pt atoms supported on θ-alumina slab.

Since our experimental work has already shown that the distribution of platinum on γ-alumina and θ-alumina is almost identical, and the surface properties and CO oxidation of both catalysts are identical, we propose that Pt supported on θ-alumina is a better model for Pt supported on γ-alumina than Pt supported on α-alumina or simplified models of γ-alumina.

Our next step involves substitution of platinum atoms from agglomerates with palladium to understand the energetics of the system that will enable us to synthesize more durable catalysts than the current generation of catalysts.

Theoretical Studies

We have previously summarized the results on DFT calculation of bulk θ-alumina, θ-alumina slab, and a single platinum atom on a θ-alumina slab. We also reported preliminary results on a charge neutral supercell of 420 atoms combining 2 x 3 x 3 cells and found the location of platinum to optimize in an environment identical to the one in 180-atom supercell [Figure 1]. We also optimized the single Pd, Ag, or Au atom adsorbed on the [010] surface of θ-alumina and found the adsorption energies for Pt, Pd, Au, and Ag are in the order of Pt>Pd>Au>Ag and are -62.29, -44.84, -20.21, and -13.23 Kcal/mole, respectively suggesting that the absorption of these atoms is exothermic.

The analysis of projected local density of state [LDOS] leads to a different bonding picture than that reported in literature for α-alumina or γ-alumina where platinum has unpaired electrons. The platinum d orbitals and s orbitals are occupied resulting in no unpaired electrons. The interaction of platinum orbitals with Op states results in O p_y orbitals shifting to lower energy. Bonding with two neighboring oxygen atoms and charge transfer to oxygen py orbitals result in no upaired electron on platinum atom. Formally, platinum is in zero oxidation state with d^{10} structure and is bonded to two oxygen atoms. The implication of this important result is that the mechanism of CO, NO,

or HC oxidation on sub-nanometer particles such as single atoms can be expected to be different from the large particles normally examined by DFT.

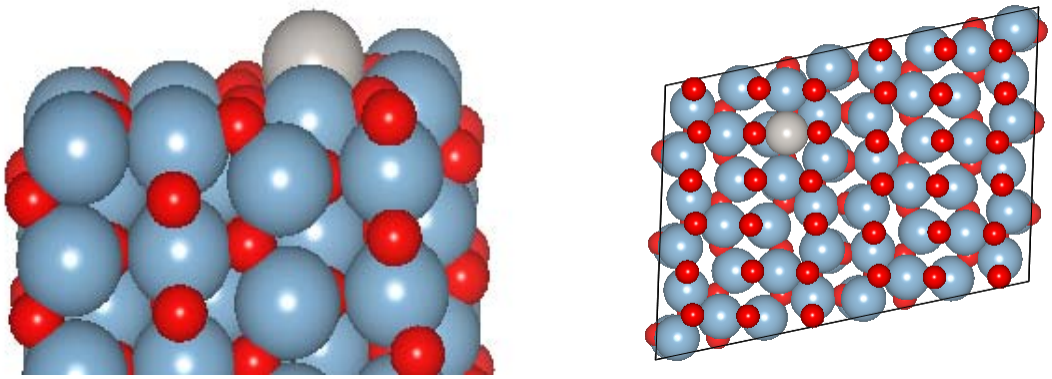

Figure 1: Pt location on a 2x4x2 (left) and 2x3x3 (right) supercells of 010 surface

The configuration of a palladium atom is $d^{10}s^{0}$, and it has higher energy valence d and s states than those for platinum. For Pd atoms, the Pd-O bond distances are 2.227 Å and 2.201 Å with an O-M-O angle of 134.54º. The distance from sub-surface Al is 2.49 Å and the Pd atom sits 0.86 Å above the cell surface. As expected, these distances are slightly larger that those for platinum atom but the bonding are identical to Pt atoms. For Au atoms, the Au-O bond distances are 2.45 Å and 2.69 Å with an O-M-O angle of 107.34º. The distance from sub-surface Al is 2.976 Å and nearest surface Al is 2.706 Å. The Au atom sits 1.519 Å above the cell surface. The Ag-O bond distances for Ag/θ-alumina are 2.483 and 2.549 Å with an O-Ag-O angle of 108.5º. The distance from sub-surface Al is 3.08 Å and from closest surface Al is 3.09 Å. Both Ag and Au are $d^{10}s^{1}$ atoms and the energy of their valence d and s orbitals are lower that that of valence orbitals of Pt. Since there is a magnetic moment of 1.0 associated with both atoms, they must be formally in oxidation state 2 (d^{9} species). This is supported by the fact that s orbital is empty and d orbitals exhibits polarization and partial occupancy. This bonding picture is also different from Au or Ag on α-alumina where Au is bonded to an oxygen atom and Ag occupies a three-fold hollow site. The bonding picture Au/α-alumina suggest that Au orbitals are split by interaction with oxygen but remain filled. The s orbital also remains filled. Thus Au-O interaction is proposed to be a weak filled-filled one. The interaction of silver, on the other hand, is proposed to be an ionic one where Ag s states are vacated and do not participate in bonding.

Considering the facts (reported previously) that the Pt supported on γ-alumina and θ-alumina exhibit identical bimodal distribution of platinum (single atoms and 10-20 atom clusters) when examined by ACEM and have identical CO oxidation activity, we suggest that platinum on θ-alumina is a better representative of platinum on γ-alumina than the models reported in literature (platinum on α-alumina or platinum on simplified models of γ-alumina). As described previously, the structure of platinum on γ-alumina is uncertain due to uncertainty of the structure of γ-alumina.

We have initiated the DFT structural studies of 2-atom and larger clusters of Platinum on a charge neutral supercell of 420 atoms combining 2 x 3 x 3 cells. As mentioned in the last report the single platinum atom prefers the location on both supercells that are identical in local environment and have identical adsorption energies.

There are three additional identical locations on 2x3x3 supercell for platinum and we have optimized this supercell with platinum atom at all four positions.

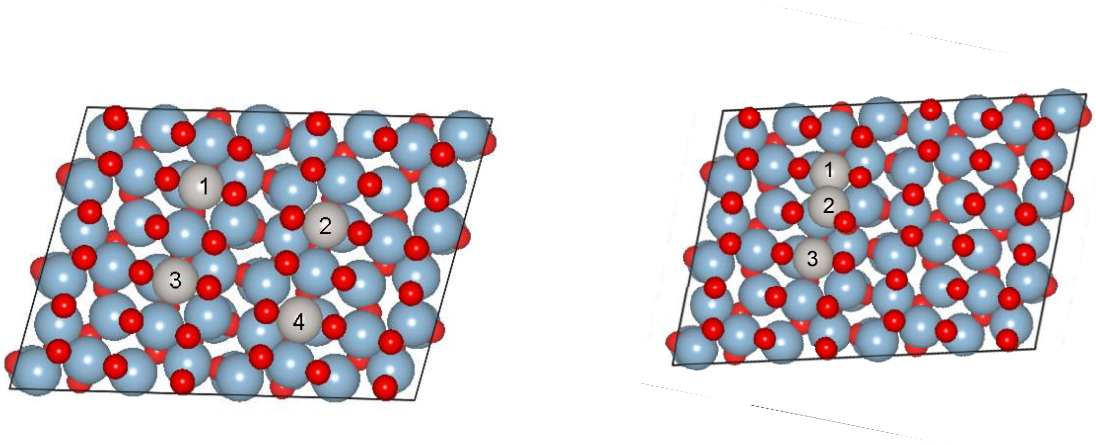

Figure 2: Platinum atoms on 2x3x3 supercell

Each of the four platinum atoms is bonded to 2 neighboring oxygen atoms and the bond distances from these oxygen atoms are summarized in Table 1.

Table 1: Platinum-Oxygen bond distances

	OXYGEN	OXYGEN
Pt 1	2.192	2.132
Pt 2	2.202	2.129
Pt 3	2.135	2.214
Pt 4	2.138	2.214

In order to build a large cluster we attempted to optimize platinum 2 bonded platinum 1. There is no significant difference (1.27 kcal/mole) between the energy of configurations where platinum 1 is bonded to platinum 2 or both platinum atoms occupy independent but identical sites. It is important to point out that, experimentally, we do not observe 2-10 atom clusters but 10-20 atom agglomerates are common. Interestingly, a platinum atom bonded to platinum 1 and platinum 3 is not energetically favorable over a platinum atom bonded to platinum 1 and an independent platinum 3 configuration shown in Figure 2 right). While platinum 1 and 3 are bonded to two neighboring oxygen atoms, the platinum 2 atom is only bonded to platinum 1. The bonding analysis for this configuration is in progress and will be presented in the next quarterly report.

The preliminary studies reported on small clusters suggest that the platinum atoms prefer independent locations where they are in zero oxidation state and are bonded to two neighboring oxygen atoms. This is also observed experimentally where we generally observe a bimodal distribution of single atoms and 10-20 atom agglomerates. We are developing models to understand the bonding in the 10-20 atom agglomerates. Our next step will be to study palladium substituted platinum agglomerates.

Experimental Studies

In order to be able to compare the results of theoretical models on palladium substituted platinum agglomerates, we have initiated studies to synthesize and characterize platinum-palladium agglomerates supported on alumina substrates.

We followed the procedure described by Toshima *et al.* (J. Chem. Soc. Faraday Trans., 1993, 89, 2537-2543) for the synthesis of bimetallic Pd-Pt clusters with different ratios in homogeneous size, around 1.5 nm, employing poly(N-vinyl-2-pyrrolidone) (PVP, average MW 40,000) to stabilize nanoparticles. The synthesis of particles is summarized in the following paragraphs:

Pd-Pt (1:1) on γ-Al_2O_3: A solution of hexa-chloroplatinic(IV) acid (66.4 mg, 0.133 mmol) and 1.180 g PVP in 100 mL water was added to a $PdCl_2$ (23.5 mg, 0.133 mmol) solution in 100 mL ethanol prepared by overnight stirring. The reaction mixture was heated under reflux for 1 hour, resulting in a dark brown transparent solution, which was cooled and dried in the air to yield a black solid. The black solid was dissolved in water and precipitated with acetone to obtain dark brown solid which was filtered and dried. The dark brown powder was added to water slurry (60 mL) of 1 g γ-alumina. The slurry was stirred over night and centrifuged to isolate dark grey powder. This dark grey powder was dried first overnight at room temperature and then for 1 hr at 100°C. The dried powder was sintered at 350°C for 1 hour to obtain Pd-Pt clusters supported on γ-alumina. The TEM of the clusters shows that the size of particles is ~2 nm [Figure 3].

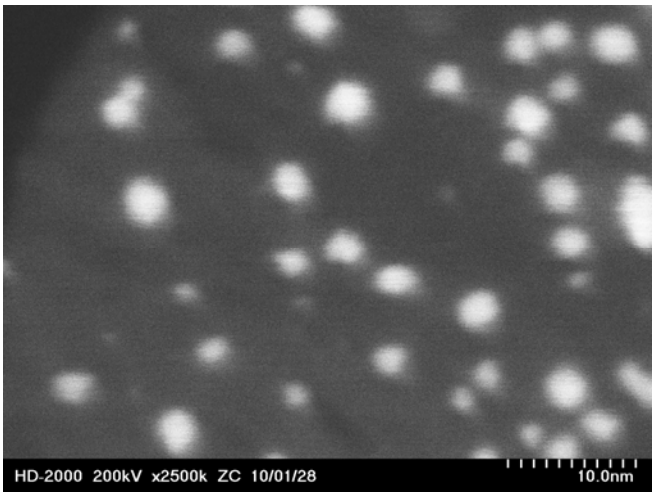

Figure 3: TEM of Pd-Pt (1:1) clusters on γ-Alumina

Pd-Pt (4:1) on γ-Al_2O_3: A solution of hexa-chloroplatinic(IV) acid (32.2 mg, 0.064 mmol) and 1.432 g PVP in 100 mL water was added to a $PdCl_2$ (45.7 mg, 0.258 mmol) solution in 120 mL ethanol prepared by overnight stirring. The reaction mixture was heated under reflux for 1 hour, resulting in a dark brown transparent solution, which was cooled and dried in the air to yield a black solid. The black solid was dissolved in water and precipitated with acetone to obtain dark brown solid which was filtered and dried. The dark brown powder was added to water slurry (100 mL) of 2 g γ-alumina. The slurry was stirred over night and centrifuged to isolate dark grey powder. This dark grey powder

was dried first overnight at room temperature and then for 1 hr at 100°C. The dried powder was sintered at 350°C for 1 hour to obtain Pd-Pt clusters supported on γ-alumina.

Next Steps: We plan to carry out the following tasks:

- We will carefully characterize palladium substituted platinum agglomerates and study their durability under CO, HC, and NO_x oxidation conditions and diesel emissions treatment conditions.
- Complete theoretical calculations on 10-20 atom platinum clusters supported on θ-alumina surface.
- Initiate CO oxidation theoretical studies on platinum single atoms supported on θ-alumina surface.

Other Activities

A joint project on lean NO_x treatment is on going with John Deere Co under work for others arrangement.

Communication/Visitors/Travel

Following abstracts have been accepted for presentation:

1. C.K. Narula, X. Chen, M.G. Stock, "First-Principles Studies of the Structure and Bonding of Metal Atoms Supported on θ-Alumina," American Physics Society Meeting, March 15-19, Portland, OR.
2. C.K. Narula, X. Chen, M.G. Stock, "First-Principles Studies of the Structure and Bonding of Metal Atoms Supported on θ-Alumina," Computational Chemistry Symposium at American Chemical Society Meeting, March 21-26, San Francisco, CA.

Publications

1. C.K. Narula, X. Chen, M.G. Stocks, Unraveling the structure of metal atoms supported on alumina, Nature, (manuscript in preparation)
2. C.K. Narula, "Catalyst by Design – Bridging the Gap between Theory and Experiments at Nanoscale Level" Encyclopedia of Nanoscience and Nanotechnology, Vol. II, Taylor & Francis, New York, 2008, pp 771-782 (invited).
3. C.K. Narula, L.F. Allard, D.A. Blom, M. Moses-DeBusk, "Bridging the Gap between Theory and Experiments – Nano-structural Changes in Supported Catalysts under Operating Conditions" SAE-2008-01-0416, SAE Int. J. Mater. Manu., 1(2008) 182-188.
4. C.K. Narula, L.F. Allard, D.A. Blom, M.J. Moses, W. Shelton, W. Schneider, Y. Xu, "Catalysis by Design - Theoretical and Experimental Studies of Model Catalysts", SAE-2007-01-1018 (invited).
5. C.K. Narula, M.J. Moses, L.F. Allard, "Analysis of Microstructural Changes in Lean NO_x Trap Material Isolates Parameters Responsible for Activity Deterioration" SAE 2006-01-3420.

6. Y. Xu, W.A. Shelton, and W.F. Schneider, “The thermodynamic equilibrium compositions, structures, and reaction energies of Pt*x*O*y* (*x* = 1-3) clusters predicted from first principles,” *Journal of Physical Chemistry B,* 110 (2006) 16591.
7. Y. Xu, W. A. Shelton, and W. F. Schneider, “Effect of particle size on the oxidizability of platinum clusters,” *Journal of Physical Chemistry A*, 110 (2006) 5839.
8. C.K. Narula, S. Daw, J. Hoard, T. Hammer, “Materials Issues Related to Catalysts for Treatment of Diesel Exhaust,” *Int. J. Amer. Ceram. Tech*., 2 (2005) 452 (invited).

Presentations (last 12 months)

1. Moses-DeBusk, M.; Narula, C.K. "Catalyst by design: Combining the power of theory, experiments, and nanostructural characterization for catalyst development," 227th National American Chemical Society Meeting, March 2009 (invited).
2. Narula, C.K.; DeBusk, M.M.; Allard, L.F.; “Catalyst by Design – Theoretical, Nanostructural, and Experimental Studies of Oxidation Catalyst for Diesel Engine Emission Treatment, DEER 2009, Detroit, MI

Agreement 19214: Biodiesel Impact on Diesel Particulate Filter Durability

M. J. Lance and T. J. Toops
Oak Ridge National Laboratory

Objective/Scope

To characterize changes in the microstructure and material properties of diesel particulate filters (DPFs) in exhaust gas produced by biodiesel blends.

Technical Highlights

The specimen preparation for the measurement of strength degradation in a DPF was initiated. This work overlaps with Agreement 20091 (Electrically-Heated Diesel Particulate Filter Regeneration) on Project 18519 (same project as this agreement) however, that CRADA has yet to be signed so sample preparation relevant to both agreements is being conducted on this agreement. Figure 1 shows two disks machined from a cordierite filter that will be tested in biaxial flexure. Following testing, smaller samples will then be harvested from the fractured samples and so on which will allow us to determine the effect of sample size on the fracture strength of the filter. It is expected that the fracture strength will increase with smaller samples which may account for the lack of failure observed by GM during testing of the electrically-heated DPF regeneration system.

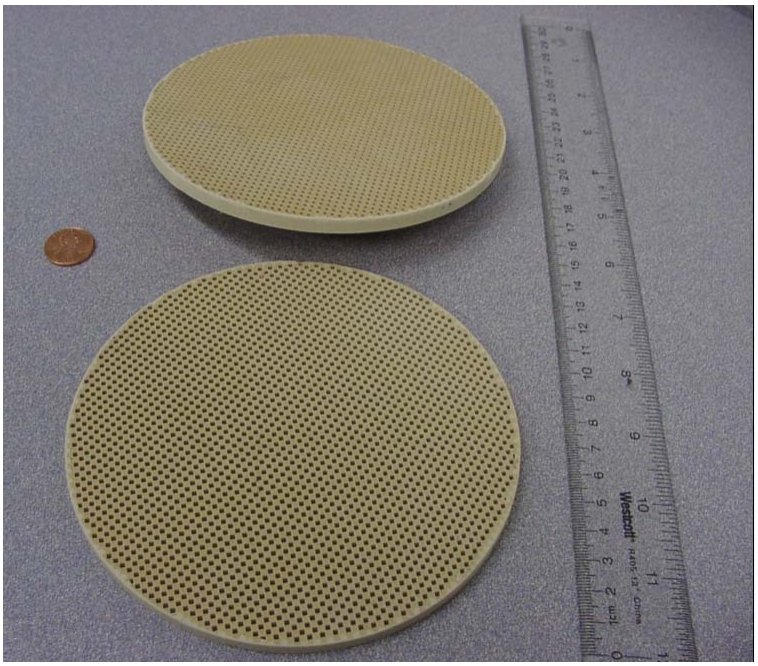

Figure 1. Disks machined from a cordierite DPF.

Status of FY2010 Milestones
Measure the chemical composition and pH of condensate and PM generated by a diesel engine running with ULSD and biofuel blends. (09/10) *On Schedule.*

Communications/Visits/Travel
None.

Problems Encountered
The single cylinder engine needed for determining the acidic species present in biodiesel blends and ULSD is booked until March. Before proceeding with the testing of DPF coupons, we need to determine acidic species so the low availability of the engine has been holding up work.

Publications/Presentations/Awards
None.

References
None.

Agreement 9105: Characterization of Catalyst Microstructures

L. F. Allard, C. K. Narula, C.H.J. Peden, J.-H. Kwak and A. K. Datye
Oak Ridge National Laboratory

Objective/Scope

The objective of the research is to understand fundamental processes in catalytic systems with applications to transportation technologies, such as those used for the treatment of NO_X emissions, and for the production of biomass-derived liquid fuels. The research heavily utilizes new capabilities and techniques for ultra-high resolution transmission electron microscopy with the HTML's aberration-corrected electron microscope (ACEM). The research is ultimately focused on understanding the effects of reaction conditions on the changes in morphology of heavy metal species on "real" catalyst support materials (e.g. oxides and carbon materials), and the understanding of the structures of model mono-, bi- and multi-metallic catalyst systems of known particle composition. A major thrust of these studies has been to develop methods of in-situ microscopy at elevated temperatures and under controlled gas compositions. This work has expanded with the collaboration with Protochips Inc. (Raleigh, NC), who provide a novel heating technology utilizing MEMS-based heating devices that we have shown to be stable enough to provide sub-Ångström imaging capabilities at high temperature in the ACEM. Model samples of nanoparticulates of controlled composition on carbon or oxide supports are also being studied in collaboration with the catalysis group at the University of Texas-Austin (Prof. P. Ferreira), the University of Texas-San Antonio (Prof. M. Jose-Yacaman), the University of Missouri-St. Louis (Prof. J. Liu), and University of New Mexico (Prof. A. Datye). Studies of the behavior of Pt species on oxide substrates are also being conducted with Drs. S. A. Bradley of UOP Co., and C. H. F. Peden of PNNL. NOx trap catalyst materials BaO/Al_2O_3 are being studied with Dr. Peden and Dr. Ja Hun Kwak at PNNL and Pt-Re/C catalysts on model carbon nanotube materials are being studies with Drs. Y. Wang and L. Zhang, also of PNNL.

Technical Progress

In-Situ Microscopy Developments

First Full-Cell Tests of "Gen 2" E-Cell Holder: The Second Generation or Gen 2 E-cell specimen holder for the JEOL 2200FS aberration-corrected STEM is being used for testing of the potential for this concept to be used to study elevated-temperature in-situ gas reactions with atomic-level resolution. The E-cell requires that the sample be encapsulated such that a gas can be admitted and the specimen heated simultaneously, without affecting the vacuum of the electron microscope. Also simultaneously, the electron beam must be able to penetrated the upper 'window' of the cell and interact with the sample while maintaining its fine-probe characteristics, and the signal from the sample then must pass through the reaction gas volume with a path length set by the distance between upper and lower windows, and finally through the lower window to reach the electron detectors for both bright-field (BF) and high-angle annular dark-field (HA-ADF) images. As a reminder, this cell geometry is shown in Fig. 1a and 1b.

We showed previously that it was possible to image a catalyst sample, gold on iron oxide (used for the water-gas shift reaction and for CO oxidation to CO_2) with excellent resolution with the electron beam passing through a 25nm window of amorphous silicon nitride. The window in that test was not part of a Protochips Aduro^{TM} heater chip, i.e. it was a stand-alone membrane with the sample powder deposited on the underside. This test showed that incorporation of thin SiN films over the surface of a heater chip, if practicable even thinner than 25nm, would be an ideal upper window for the E-cell. That process is currently under development by our collaborators at Protochips, to be a final step in the microfabrication of E-cell heater/windows. In the meantime, we tested the use of an evaporated carbon film as the upper window. This was done by first evaporating about 25nm of carbon onto a cleaved NaCl crystal, then floating off the evaporated film in water, and finally picking up the film properly on an AduroTM heater chip that was sealed into the upper plate of the E-cell holder. The schematic of Fig. 1a indicates the use of this carbon film for testing the full E-cell geometry.

The tests were conducted again with the Au/FeOx catalyst sample deposited on the heater window, by carefully placing a small quantity of the powder onto the heater, then shaking off the excess, being careful to not allow any powder to be deposited on the upper surface of the heater. Although the thought suddenly occurs while typing this text, that, if it were easy to tell which side of the carbon film the powder was on, one might be able to compare heating of a catalyst sample in a gas-reaction experiment by imaging catalyst inside the E-cell, with heating of the catalyst material in the vacuum of the electron microscope, both in the same heating experiment. This idea might be worth exploring in a future test session.

Examples of the results of our first imaging in the full cell geometry are shown in Figs. 2 and 3. Figure 2a is a HA-ADF image of a gold nanoparticle on the FeOx support, recorded at 12Mx direct magnification, showing a near-perfect orientation of the gold lattice in the <110> zone-axis orientation, showing e.g. the {200} cube planes with 2.04Å resolution. This image was recorded with the sample at 500°C, and with no gas in the E-cell; that is, the cell was pumped to a vacuum of a few millitorr by the scroll pump in the gas-handling manifold of the E-cell system. Figure 2b shows a gold nanoparticle recorded at 10Mx direct magnification, with the sample still at 500°C, but with the cell pressurized at 1.2 Torr with a reducing gas (4%H_2/Ar). The particle is larger, and not in a perfect orientation, but the 2.04Å {200} planes are still seen. The cell was further pressurized to 2 Torr, and a series of images of the same gold nanoparticle was recorded at 10Mx direct magnification at 500°C. Three images in that series are shown in Fig. 3; the particle is in a near-perfect <100> cube axis orientation, with both sets of 2.04Å planes imaged. Subtle changes are seen in the particle over time (a few minutes for the entire series), with e.g. ledges of {100} planes forming as indicated by the arrow in Fig. 3c. To our knowledge, this is the first example of imaging at this level of resolution, at elevated temperature, in an enclosed cell, in-situ gas reaction experiment.

New imaging phenomenon explained: We are also working on in-situ studies of model palladium and platinum catalysts supported on novel zinc oxide structures that have known, and simple, geometries that are more amenable to interpretation of catalyst behavior than possible with "real" catalysts. In studies with Prof. Jingyue (Jimmy) Liu of the University of Missouri-St. Louis, we have characterized the effects of elevated temperature treatments of

Pd on ZnO "nanobelts." The ZnO nanobelts used in these experiments were fabricated by a thermal evaporation-condensation method in a high-temperature tube furnace. Each nanobelt is a single crystal with relatively uniform thickness, and some nanobelts possess atomically flat and clean surfaces. Figure 4 shows a scanning electron micrograph of a batch of the as-prepared nanobelts. Figure 5 is a HA-ADF image of Pd nanoparticles on a well-oriented ZnO nanobelt; the Pd particles grew from an atomic dispersion of Pd on the ZnO surfaces during elevated temperature treatments in the ACEM. Also noted is the row of bright atom contrast as indicated by the arrows in Fig. 4, and this row of bright atoms is seen to continue even beneath the large surface Pd nanocrystal. The row actually represents columns of atoms in the perfectly oriented crystal surface, and the bright contrast at first might be interpreted as columns containing a substantial percentage of Pd atoms. Figure 6 is another image of a ZnO nanobelt in the same crystal orientation, with the same bright contrast in the near-surface layer, but having Pt atoms and clusters on the surface beyond the bright atom row. These species represent in total an incomplete additional plane of atoms beyond the observed bright atom plane. In several additional experiments, we showed that the bright contrast could be extinguished simply by tilting the sample around an axis parallel to the surface, but would not be extinguished by tilting around an axis within the plane, normal to the surface. Those axes are shown, respectively, as the [-1100] and [0001] axes (ZnO hexagonal crystal structure notation) in Fig. 6.

We also quantified the spacing between the bright atom row and the next row of Zn atoms within the ZnO crystal; it was measured to be approximately 0.30 nm, much larger than the bulk lattice spacing of 0.26 nm. These observations and a series of other experiments suggest that a <u>surface-resonance channeling effect</u> may play a major role in determining the observed anomaly of intensity enhancement of HA-ADF images of structurally perfect surfaces [1]. A better understanding of the effect of surface/interface channeling on HA-ADF image contrast may have implications for the quantitative interpretation of those images and may provide new routes to utilization of this technique to study surface structures with sub-Ångström resolution. This analysis gives us further tools to better understand the image features revealed by our sub-Ångström resolution capability in the aberration-corrected electron microscope. A publication on this work is under preparation.

Modeling catalyst nanoparticle structures: In order to more reliably understand the HA-ADF imaging results from our catalyst studies using the ACEM, we have as one goal to be able to do simulations of the images that would be expected from nanoparticles of particular shapes, and to compare them quantitatively with the experimental images. Simulating HA-ADF images is a computer-intensive operation, and also requires careful construction of the atomic models of the nanoparticle to be simulated. We are collaborating on several catalyst projects, primarily involving studies of bimetallic and trimetallic compositions for fuel cell applications, with Prof. Paulo Ferreira and his group at the Univ. of Texas-Austin. His student Brian Patrick has developed the tools for modeling nanoparticle structures, and then computing the expected HA-ADF images from those models. We are currently working to transfer those tools to be used at ORNL for our future studies.

An example of the additional power this new capability brings is shown in Fig. 7. A model of a cube-octahedron shape is shown in Fig. 7a. When observed looking down a <110>

direction (i.e. normal to the edge shown in white in 7a), the shape matches reasonably well the experimental HA-ADF image shown in Fig. 7b. Software was written to model this cube-octahedron with a composition of Pt3Co, the nominal composition of platinum-cobalt fuel cell nanocatalysts used in our study; the software allowed us to place this composition randomly on the atom positions determined for the model structure. The simulated HA-ADF image with a random distribution of Pt-Co atoms at 3Pt to 1Co atomic ratio is shown in Fig. 7c, and compared to a perfectly ordered Pt_3Co structure, shown in Fig. 7d. Figures 7e-g are color-mapped intensity profiles of the experimental image compared to the profiles for the disordered and ordered structures, respectively. It is clear that the experimental image does not show a random dispersion of Pt and Co atoms, but that these elements are segregated to some extent in the structure. This modeling and image simulation capability has also been applied to characterize surface segregation of Pt atoms in the first 3 layers of Pt_3Co nanoparticles. The work was presented at the Fall meeting of the Materials Research Society in Boston, and also be presented at the next annual meeting of the Microscopy Society of America this summer in Portland [3]. A publication is under preparation.

References

1. J.M. Cowley, Observations of surface-channeling phenomena with a STEM instrument *Ultramicroscopy* **27** (1989) 319.

2. J. Liu and J.M. Cowley, Scanning reflection electron microscopy and associated techniques for surface studies. *Ultramicroscopy* **48** (1993) 381-416.

3. B.N. Patrick, L.F. Allard, Y. Shao-Horn and P.J. Ferreira, Aberration-Corrected STEM Image Simulation of Segregation in Pt_3Co Nanoparticles for PEM Fuel Cells, submitted to *Microscopy & Microanalysis* 2010.

Status of Milestones

On schedule

Communications/Visits/Travel

L. F. Allard co-organized the 4-day symposium "Advanced Microscopy and Spectroscopy Techniques for Imaging Materials with High Spatial Resolution," with Profs. Manfred Ruehle (Stuttgart), David Seidman (Northwestern) and Joanne Etheridge (Monash University), held at the Fall meeting of the Materials Research Society in Boston, Dec. 2009.

Publications

No publications this quarter.

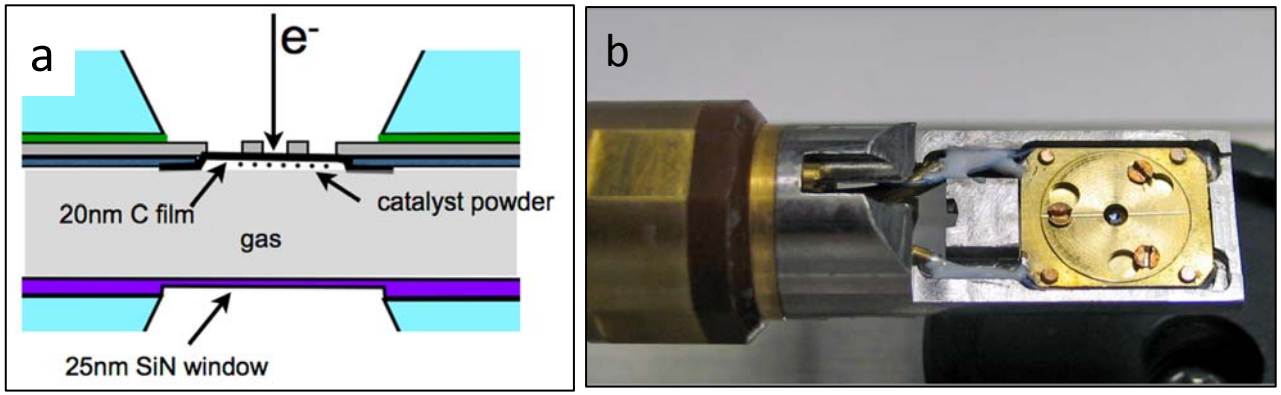

Fig. 1. a) Schematic of E-cell geometry, showing heater membrane upper window coated with a C film, with catalyst deposited on C film; b) top view of Gen 2 E-cell, with heater window in place.

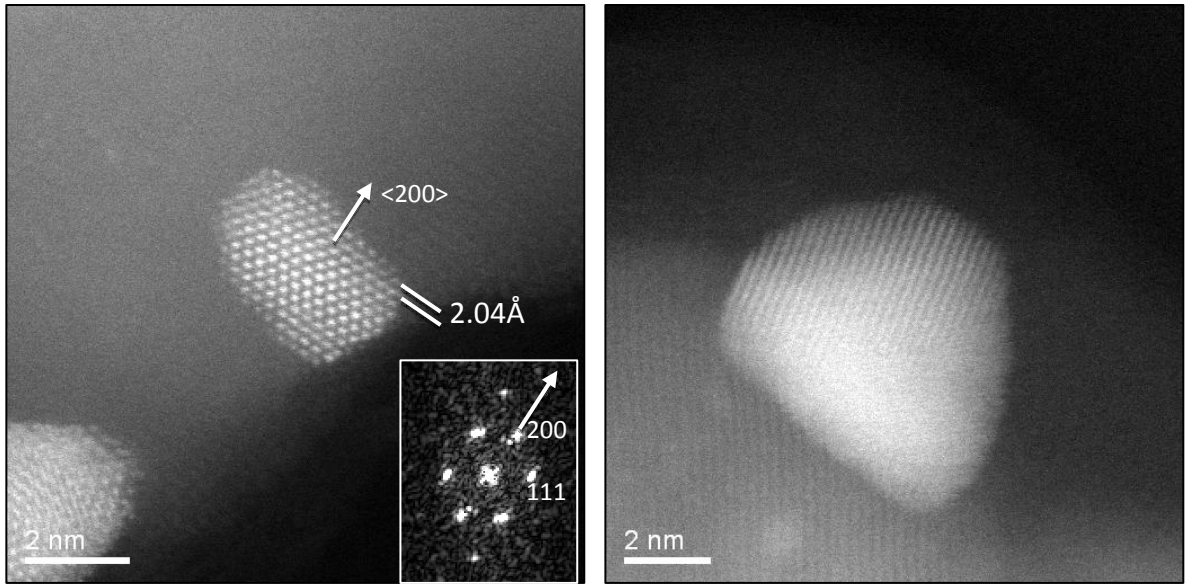

Fig. 2. a) Au nanoparticle in perfect <110> orientation; HA-ADF image at 500°C, with no gas in the E-cell; b) Similar HA-ADF image with 1.2Torr gas in E-cell, at 500°C.

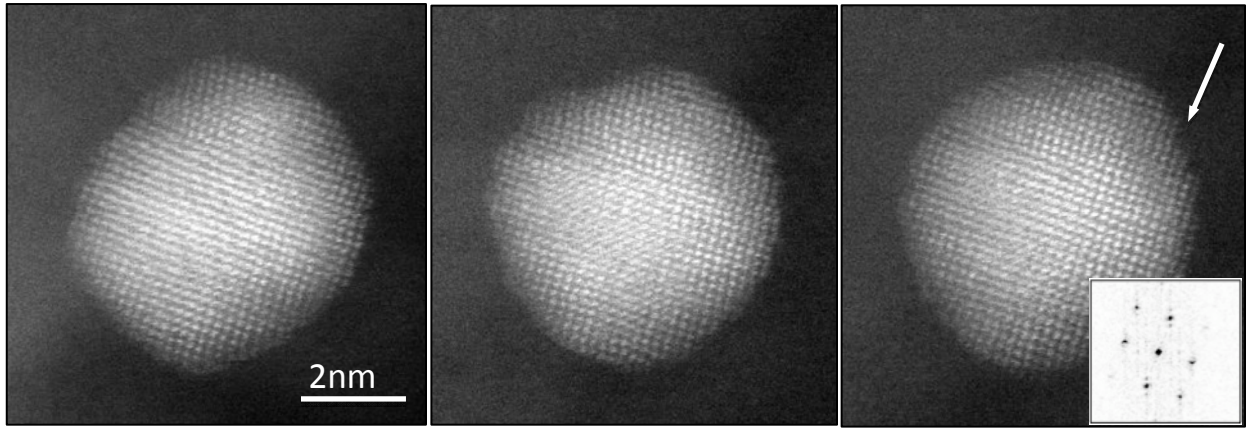

Fig. 3. Three frames from image sequence of Au nanoparticle with E-cell operating at 2 Torr, 500°C; particle imaged through a 25nm C window. Particle orientation is near <100>. Note {100} ledges developed during heating (arrow).

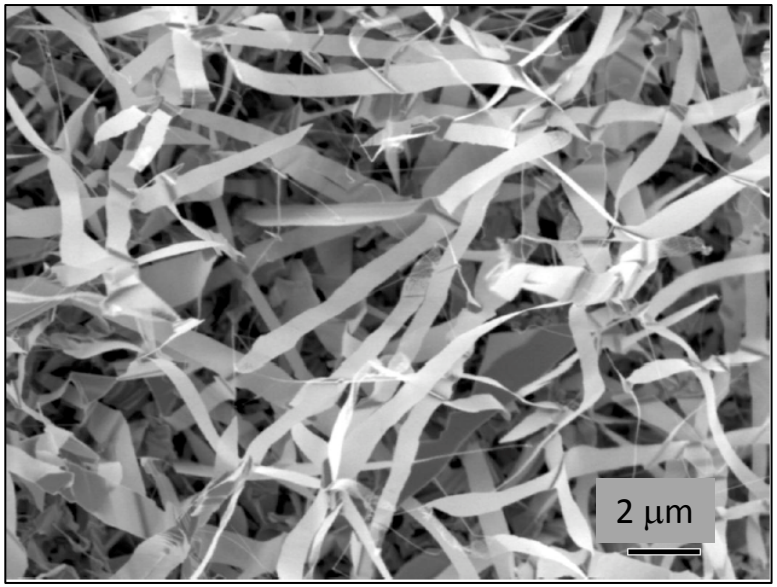

Fig. 4. Secondary electron image from an SEM showing ZnO nanobelt morphology.

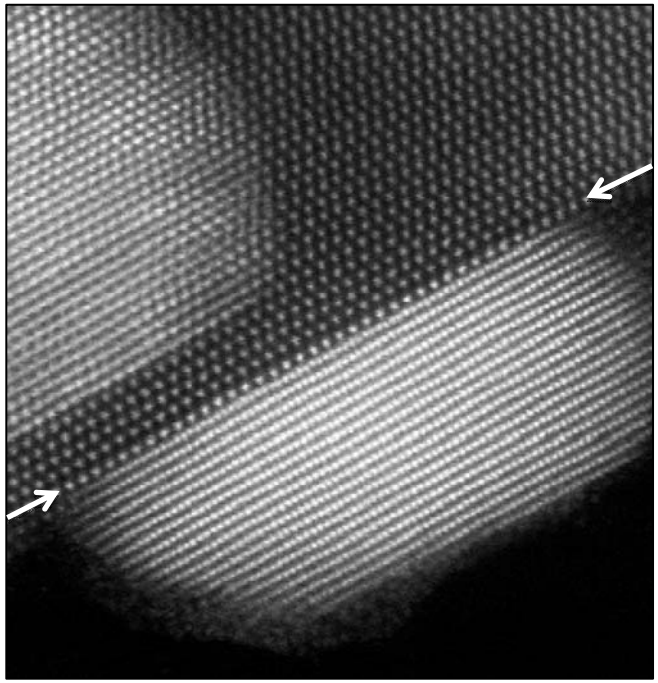

Fig. 5. ZnO nanobelt, with 2 Pd nanocrystals grown in-situ. Note bright row of atom columns as indicated by arrows.

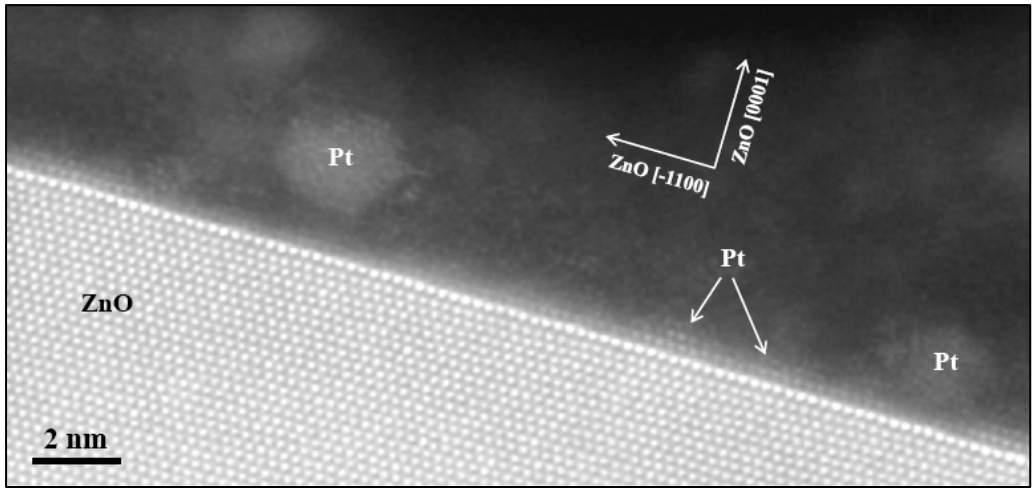

Fig. 6. Another ZnO nanobelt perfectly oriented, with ZnO crystal directions labeled. Note faint additional clusters and partial atom layers outside bright row of atom columns as seen in Fig. 5.

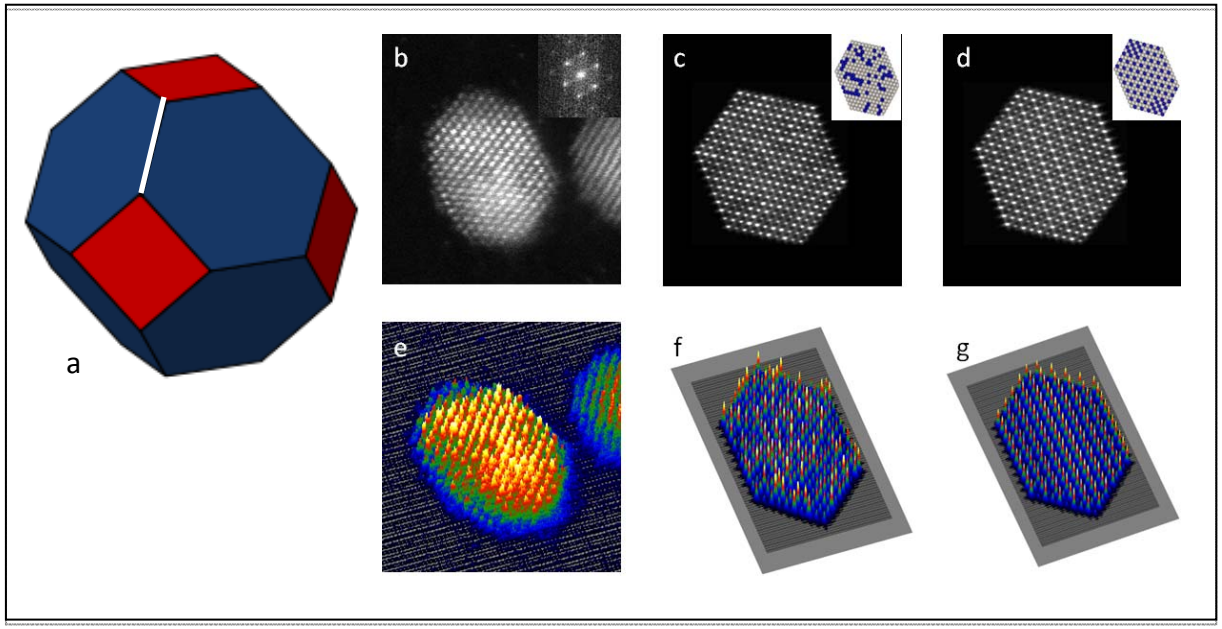

Fig. 7. Example of modeling and simulation of images of nanocrystals. a) schematic of cube-octahedron structure, which is the shape suggested by the HA-ADF image of a nominal Pt_3Co nanoparticle in (b); c) and d) are respectively simulated images of random Pt_3Co structure and fully ordered Pt_3Co structure. The three final images e-g) show 3d intensity profiles of the experimental image, and the two simulated images. The experimental image is confirmed to be segregated in Pt and Co.

Agreement 14957: High Temperature Thermoelectrics

A. A. Wereszczak, H. Wang, R. McCarty, J. Sharp,****
M. E. Ragan, K. T. Strong, Jr., P. J. Ritt, J. R. Salvador,* and J. Yang*****
Oak Ridge National Laboratory
****Marlow Industries, Inc.**
*****General Motors R&D Center**

Objective/Scope

Measure needed thermomechanical and thermophysical properties of candidate thermoelectric (TE) materials and then use their data with established probabilistic reliability and design models to optimally design automotive and heavy vehicle TE modules. Thermoelectric materials under candidacy for use in TE modules tend to be brittle, weak, and have a high coefficient of thermal expansion (CTE); therefore, they can be quite susceptible to mechanical failure when subjected to operational thermal gradients. A successfully designed TE module will be the result of the combination of temperature-dependent thermoelastic property and strength distribution data and the use of the method of probabilistic design developed for structural ceramics.

Technical Highlights

Efforts are presented in two sections: "Thermomechanical Characterization" and "CRADA with Marlow"

I. Thermomechanical Characterization

I.A. Introduction

Skutterudites are attractive thermoelectric material (TMs) candidates for use in thermoelectric devices (TDs) under consideration for power generation associated with intermediate- and high-temperature waste heat recovery. These (any) thermoelectric materials must first possess sufficient thermomechanical robustness to withstand the operational thermal gradients that activates their thermoelectric effect.

Tensile strength (and its scatter) is one indicator of that robustness. To support that assertion, Kingery's [1] thermal resistance parameter, R_{Therm}, is useful to first consider in context with TMs,

$$R_{Therm} = \frac{S_{Tens}(1-\nu)\kappa}{\alpha E} \quad , \qquad (1)$$

where S_{Tens} is tensile stress or tensile strength, ν is Poisson's ratio, κ is thermal conductivity, α is the coefficient of thermal expansion or CTE, and E is elastic modulus. One desires R_{Therm} to be as large as possible for improved thermomechanical resistance against effects caused by thermal gradients or thermal transients. The parameters ν, κ, α, and E are materials properties and are essentially unchangeable for any given TM under consideration. For TMs, the minimization of κ is purposely and

primarily sought because that achievement improves thermoelectric efficiency. Additionally, TMs typically have a large CTE (> 10 ppm/°C). The ν for most TMs usually ranges between 0.25-0.30. The Es for TMs typically range between 50-140 GPa; however, the E is virtually unchangeable within a given class of TMs (e.g., skutterudites, TAGS, tellurides, etc.). Therefore, the intent to make the R_{Therm} for TMs as large as possible is primarily hindered by the inherently low κ and typically high CTE.

The remaining parameter in Eq. 1 is S_{Tens}. Its consideration is complicated by the fact that S_{Tens} for brittle materials, including TMs, is not necessarily a size- nor temperature-independent value. The S_{Tens} for brittle materials is a function of many parameters that are either intrinsic or extrinsic to the material. Why consider S_{Tens} and not the material's compressive strength? The S_{Tens} is anticipated to be at least one order of magnitude lower than compressive strength in TMs for the same amount of stressed material (as is the case for polycrystalline ceramics) because of the brittleness (i.e., low fracture toughness). Therefore, for conservative design, testing should focus on the measurement of a tensile strength in TMs. Of all the parameters used in the right-hand side of Eq. 1, the manufacturers of TMs can only tangibly increase R_{Therm} by increasing S_{Tens}. Thus, the valid measurement of strength in TMs, the identification of those flaws that limit strength, the active reduction of those flaw sizes to increase S_{Tens}, and appropriate strength-size-scaling of TMs in thermoelectric device design all need to be executed to ultimately achieve the highest probability of survival of a TD in service.

The primary goal of this study was to measure the S_{Tens} (via three-point-bend testing) as a function of temperature of developmental n- and p-type skutterudite materials under consideration for use in devices for power generation via waste heat recovery. Another goal was to measure strength using test coupons whose geometry closely mimics that of thermoelectric legs. Owing to the relatively small size of the test coupons, a third goal was to develop and use a test fixture that: (a) validly tests for failure stress, (b) has high temperature capability, (c) has a means of efficiently and easily promoting alignment, and (d) has a simplicity that enables the testing of large numbers of test coupons in a relatively short period of time.

I.B. Experimental Procedure

I.B.i. Material Description

N-type thermoelectric materials ($Yb_{0.27}Co_4Sb_{12.08}$) were prepared on a 60 g scale by combining Co and Sb in approximately a 1:3 ratio and melting them by induction in a boron nitride crucible under an argon atmosphere. The resulting melt was combined with elemental Yb and Sb to a nominal composition of $Yb_{0.40}Co_4Sb_{12}$ in a carbon coated fused silica tube and then flame-sealed under a reduced atmosphere. The excess of Yb is a required due to the formation of Yb_2O_3 as a side product. The charge was melted at 1150°C for 5 minutes with subsequent annealing of the melt at 800°C for 1 week. The annealed melt was then milled, cold pressed, and annealed for an additional week at 800°C.

P-type materials were prepared by first alloying Co and Fe in a 1:3 ratio by arc-melting, then combining the alloy with elemental Ce and Sb with a nominal composition of $Ce_{1.05}CoFe_3Sb_{12.10}$ (the excess of Ce and Sb were necessary due to losses by vaporization) with a final mass of 60 g in a boron nitride crucible. The charge was melted by induction under Ar at 1100°C for 1 week.

The synthesis of both n- and p-type materials results in low density sintered powders, which were further milled in preparation for consolidation by spark plasma sintering (SPS). Consolidation of $Yb_{0.27}Co_4Sb_{12.08}$ proceeded by loading 12 g of milled powder into a 12.7-mm boron nitride coated die. The powder was placed under 50 MPa of uniaxial pressure under dynamic vacuum, then heated at a rate of 75°C/min to 720°C, and then soaked for an additional 2 minutes. The three consolidated pellets from this process were all greater than 98% theoretical density. The p-type material was processed in a similar manner to the n-type samples, but was heated at a rate of 75°C/min to 675°C with subsequent soaking for 2 minutes.

Prismatic bars of developmental n-type ($Yb_{0.27}Co_4Sb_{12.08}$) and p-type ($Ce_{0.86}Co_{1.02}Fe_{2.98}Sb_{11.97}$) skutterudite were prepared having nominal dimensions of 1.5 x 1.5 x 12 mm. Samples were cut from the cylindrical SPS consolidated ingots by wafering along the cylinder axis with a low speed diamond saw. Their edges were not chamfered. The electrical resistivity (ρ), Seebeck coefficient (S), and power factor for both materials are shown as a function of temperature in Fig. 1. The transport properties were evaluated using an Ulvac ZEM-3 system. The ρ and S responses for the n-type material are equivalent to responses measured previously on a similar material [2].

For the identification of strength-testing temperatures in a material whose general response is an unknown, it is often useful to first perform dilatometry to identify any temperature where a potential change of state could be occurring [3] or where the material goes into a non-equilibrium state. Dilatometry was performed on both the n- and p-type skutterudite, and the responses are shown in Fig. 2. There was no observable inflection in the elongation as a function of temperature response for the n-type material, but there was at approximately 425°C for the p-type material. This was observed on two specimens, so its response was consistent. Therefore, strength testing with the n-type was performed through 500°C and that for the p-type to 400°C.

I.B.ii. Strength Testing Description: Three-Point-Bending via "Ball-on-Two-Roller Loading"

The cross-sectional dimensions of thermoelectric legs in TDs are often 1 x 1 to 4 x 4 mm, so three-point flexure strength testing was performed on prismatic bars having cross-sectional dimension in that range (1.5 x 1.5 mm in this case). This approach was deemed superior to other types of strength tests and geometries (e.g., ring-on-ring biaxial flexure testing of disk specimens) because produced failures can be caused by flaw-types and flaw-locations (e.g., edges, etc.) that are likely to exist in thermoelectric legs.

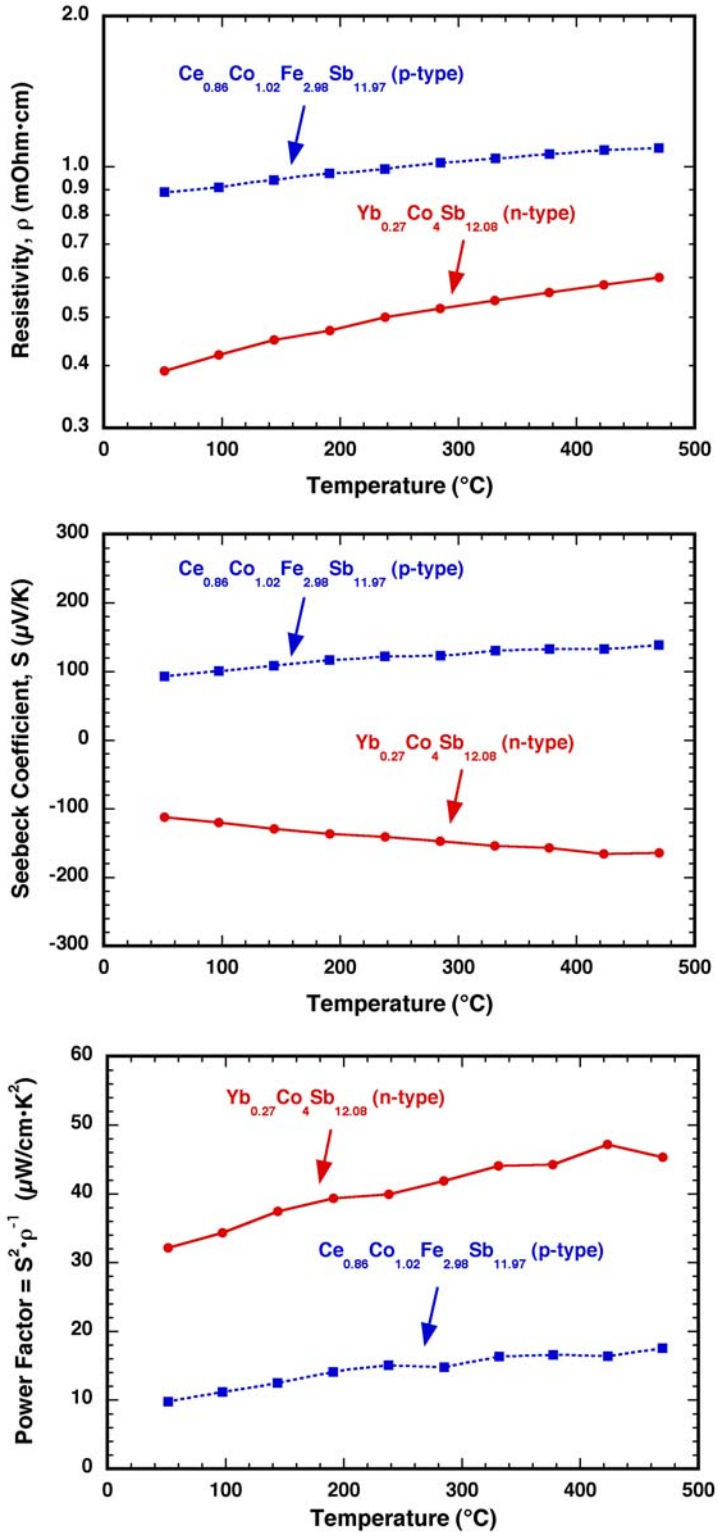

Figure 1. Electrical resistivity (top), Seebeck coefficient (middle), and power factor (bottom) as a function of temperature for the n- and p-type skutterudites.

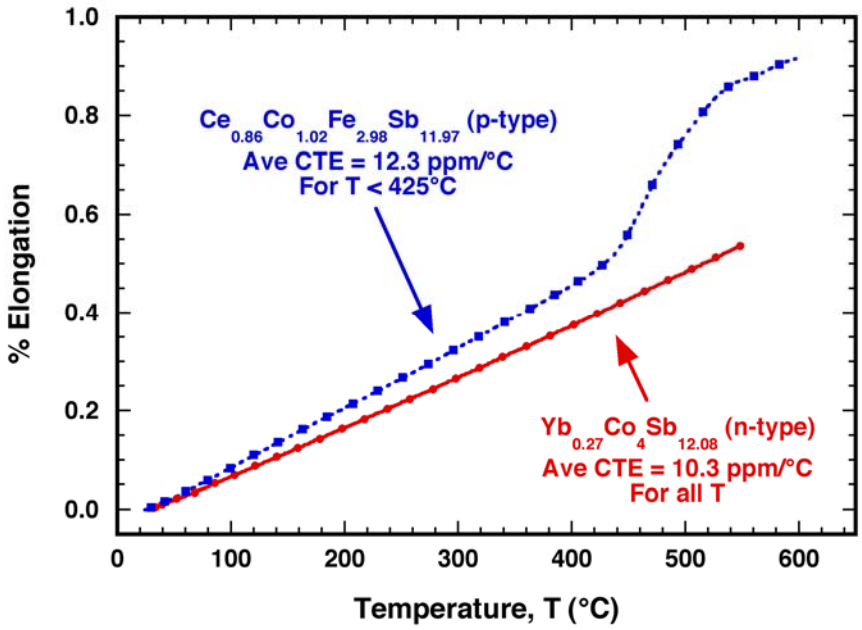

Figure 2. Percent elongation as a function of temperature for the n- and p-type skutterudites. The p-type material underwent a change of state ~ 425°C resulting in an increased rate of elongation.

Owing to the relatively small size of the test coupons, a test fixture was conceived and developed that has high temperature capability, has a means of efficiently and easily promoting alignment, and has a simplicity that enables the testing of large numbers of test coupons in a relatively short period of time. The fixture is shown in Fig. 3. It consists of an alumina tube whose outside diameter closely fits the inside diameter of a larger tube. The inner tube has two grooves cut in one end that retain smaller alumina rollers which serve as the support span for the specimen. The specimen is set and centered on the rollers, and then an alumina sphere is set on the specimen, which provides the top or third-point loading onto the specimen. The all-alumina fixture construction enables high temperature testing. The diameter of the sphere and the outer diameter of the inner tube are matched, and are kept concentrically aligned by the inner diameter of the outer tube throughout the testing duration. An exploded view of the fixture and specimen is shown on the left of Fig. 3 and its assembly is depicted on the right. The top of the sphere is higher than the outermost tube, and it is compressively loaded by a push rod thusly loading the top of the specimen. With the specimen inside the fixture, the entire assembly is then placed inside the hot zone of a radiantly heated furnace, which is all within the working zone of an electromechanical test frame. Two complete fixtures were fabricated and the use of both enabled a high throughput rate of testing.

Another attribute of this fixture is its inherent closed assembly restricts the ambient environment from coming into contact with the specimen surface and enables testing to

be done in ambient air even if the material is susceptible to oxidation. If oxidation is still operative then, alternatively, there is a “reservoir” formed by the inner tube’s inner diameter that can be filled with metal filings or graphite powder which can serve as an interior oxygen getter. Using metal filings or graphite powder with the fixture was found not to be necessary with the testing of these two skutterudite compositions because the “closed assembly” by itself sufficiently suppressed oxidation of the test specimen surfaces (even to 500°C for the n-type material).

At first glance, the ratio of the test span to specimen height (8.0/1.5 or 5.33) used in the present study is much smaller than that used in other flexure tests and fixtures. For example, ASTM C1161B [4] has a span to height ratio of 40/3 or 13.33 and (the discontinued) ASTM F417 [5] has a ratio of 25.4/1.8 or 14.11. A ratio that is too small in bend testing can cause high contact stresses to occur between the rollers and specimen if a material’s outer-fiber tensile stress is relatively high, and those high contact stresses can cause premature (and potentially misleading) failure. A contributing reason why the present study’s ratio of 8.0/1.5 works is the three-point (or outer-fiber) failure force of these test coupons is relatively low because these materials are relatively weak, and is lower than the force necessary to initiate Hertzian cracking at either the two bottom rollers or in the vicinity of the Hertzian contact circle between the upper side of the bend specimen and the loading sphere. All flexure specimens had failure initiation occur at their tensile surface, which supports this.

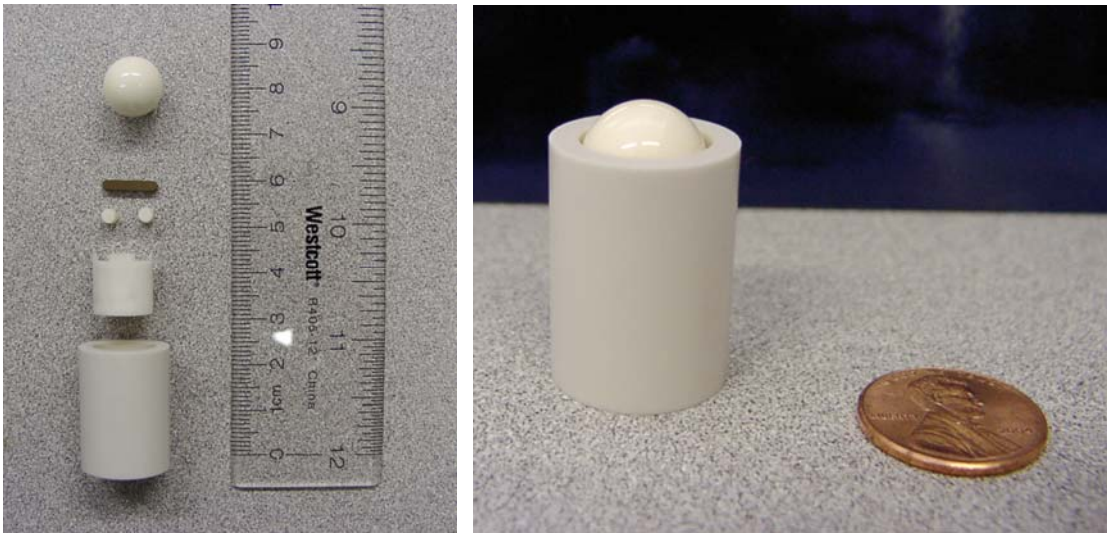

Figure 3. Self-aligning, high-temperature (all-alumina) three-point-bend fixture used to measure flexure strength of 1.5 x 1.5 x 12 mm prismatic bars. Bend span is 8 mm. Exploded (left) and assembled views (right).

Producing failure initiation at the outer fiber surface is itself not a validation of testing because one must be able to accurately estimate the associated failure stress too. The maximum outer-fiber tensile stress of the developed test configuration, as estimated by finite element analysis (FEA), was compared with that calculated from the classical

analytic beam bending equation. This comparison is shown in Fig. 4. Two FEA models were constructed: one representing the traditional "roller-on-two-roller" configuration and the other being the "sphere-on-two-roller" configuration used in this study. An elastic modulus of 135 GP and a Poisson's ratio of 0.20 were used for the thermoelectric materials [2]. The outer-fiber tensile stresses that they produced were identical and were within 3% of that of the classical three-point-bend equation. A 3% difference is small given the potential inaccuracies of any FEA model. Therefore, the analytic classical beam bending equation was used to estimate failure stress for all specimens.

The failure stress (S_{Tens}) was therefore calculated using the analytic three-point bending equation

$$S_{Tens} = \frac{3PS_L}{2bh^2} \quad , \tag{2}$$

where P is the failure force, S_L is the support span (8.0 mm), b is the specimen base (1.5 mm nominal), and h is the specimen height (1.5 mm nominal). All testing was done at a crosshead displacement rate of 0.1 mm/min in an electromechanical test frame until fracture was produced and its associated failure load (P) recorded. For high temperature testing, the specimen/fixture assembly was soaked at temperature for approximately 10 minutes prior to the commencement of loading. Testing was performed in ambient air. As indicated earlier, there was no observable evidence of oxidation on the surfaces of the test specimens.

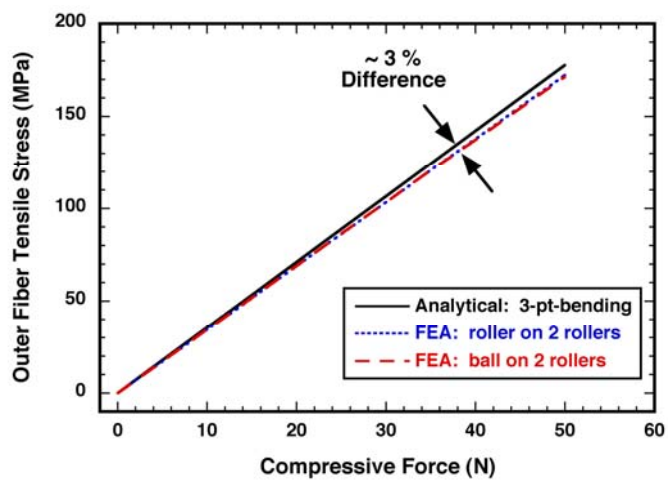

Figure 4. Comparison of the outer fiber tensile stress as a function of 3-point-bend force for the analytical case (black), its finite element analysis (blue), and the case for the bend fixture shown in Fig. 3 (red). Difference was small (~3%), so the analytical expression was used to estimate failure stresses in this study.

Commercial statistical software was used to fit the strengths to an uncensored, unimodal two-parameter Weibull distribution using maximum likelihood estimation. 95% confidence estimates were determined and used to assess any evidence of temperature-dependent changes in strength.

I.C. Results and Discussion

The strength of the n-type $Yb_{0.27}Co_4Sb_{12.08}$ and p-type $Ce_{0.86}Co_{1.02}Fe_{2.98}Sb_{11.97}$ skutterudites as a function of temperature is shown in Fig. 5 and also summarized in Table I. The strength of the n-type skutterudite was independent of temperature to 500°C. The strength of the p-type skutterudite was equivalent to that of the n-type material and also was independent of temperature to at least 200°C. The p-type's strength dropped by ~20% at 400°C. As shown in Fig. 2, both skutterudite materials were believed to be in an equilibrium state at all test temperatures at which they were tested.

The values of the measured failure stresses are made in context with the Weibull effective size according to Table II, and their relationship can then be incorporated and adapted in (probabilistic) TD design. The Weibull strength data was not censored for this study, but fractography revealed that specimens failed from each of edge-, surface-, and volume-type strength-limiting flaws. Given the effective sizes listed in Table II, the characteristic strength of the n-type skutterudite was approximately 115 MPa for all temperatures, and the p-type material had that strength at 200°C and below. However, that failure stress would scale with effective size (length, area, and volume) of the thermoelectric leg according to [6]

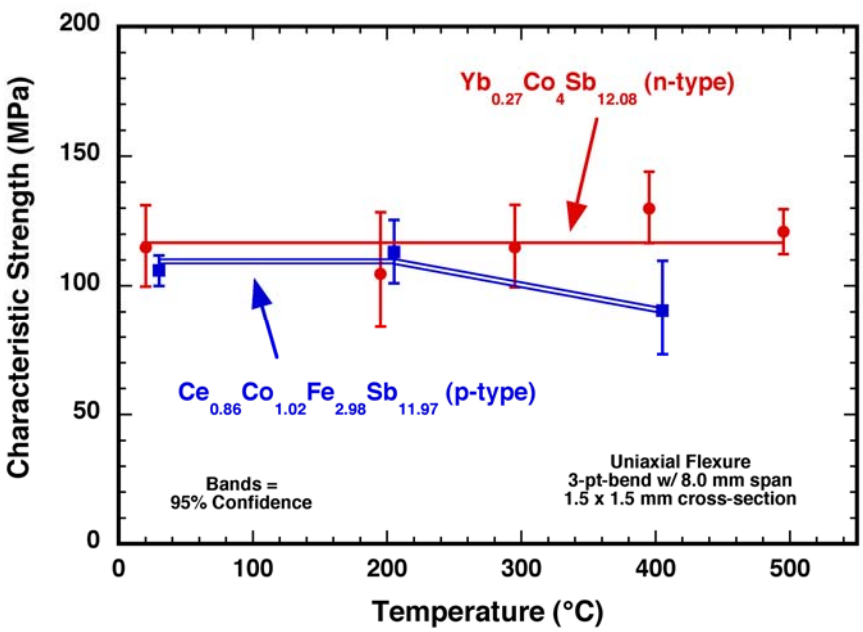

Figure 5. Characteristic strength as a function of temperature for the n- and p-type skutterudites.

Table I. Uncensored and unimodal failure stress statistics of the n- and p-type skutterudite thermoelectric materials. Three point bend testing with 8 mm span. 1.5 x 1.5 mm nominal cross-section of test specimens.

Material	Temp (°C)	# of Tests	Weibull Characteristic Strength* (MPa)	Weibull Modulus*	Gaussian Ave. Strength (MPa)	Gaussian Std. Dev. (MPa)
$Yb_{0.27}Co_4Sb_{12.08}$ (n-type)	25	17	115 (100,131)	3.6 (2.5, 5.7)	103	32
	200	15	105 (84, 128)	2.4 (1.7, 3.9)	93	39
	300	15	115 (100, 131)	3.8 (2.6, 6.1)	104	30
	400	15	130 (117, 144)	4.9 (3.4, 7.9)	120	30
	500	15	121 (112, 130)	7.3 (5.0, 11.9)	114	21
$Ce_{0.86}Co_{1.02}Fe_{2.98}Sb_{11.97}$ (p-type)	25	14	106 (100, 112)	9.7 (6.8, 16.0)	101	11
	200	15	113 (101, 126)	4.8 (3.4, 7.7)	104	24
	400	8	90 (73, 110)	3.4 (2.2, 7.1)	82	24

* Values in parenthesis = ± 95% confidence interval

$$P_f = 1 - \exp\left[-k_L L \left(\frac{S_{Tens}}{\sigma_{0L}} \right)^{m_L} \right] \text{, or} \tag{3}$$

$$P_f = 1 - \exp\left[-k_A A \left(\frac{S_{Tens}}{\sigma_{0A}} \right)^{m_A} \right] \text{, or} \tag{4}$$

$$P_f = 1 - \exp\left[-k_V V \left(\frac{S_{Tens}}{\sigma_{0V}} \right)^{m_V} \right] \text{,} \tag{5}$$

where P_f are probabilities of failure, $k_L L$, $k_A A$, and $k_V V$ are effective lengths, areas, and volumes, respectively and as shown in Table II, S_{Tens} is applied tensile stress, σ_{OL}, σ_{OA}, and σ_{OV} are length, area, and volume scaling parameters, respectively, and m_L, m_A, and m_V are Weibull moduli for length, area, and volume distributions, respectively. Such analysis is done numerically with life prediction software, and an example of such analysis can be found in Ref. [8].

For equivalent effective sizes, the characteristic strength of these skutterudites was stronger than both n- and p-type bismuth telluride thermoelectric materials recently tested by the authors [9].

Table II. Effective sizes for three-point bend testing. A fixture span (S_L) of 8.0 mm, square cross-section (b = h) 1.5 x 1.5 mm, and a Weibull modulus (m) = 5 used in the calculations. Failure stress in these materials can be limited by edge-, surface-, or volume-type strength-limiting flaws.

Effective Size	**Equation**	**for m_i = 5**
Effective Length $L_{eff} = k_L \bullet L$	$(2 \bullet S_L) / (m_L+1)$	2.67 mm
Effective Area $A_{eff} = k_A \bullet A$	$2 \bullet S_L \bullet (h+b) \bullet (m_A+2) / (4 \bullet (m_A+1)^2)$ [7]	2.33 mm^2
Effective Volume $V_{eff} = k_V \bullet V$	$b \bullet h \bullet S_L / 2 \bullet (m_V+1)^2$ [7]	0.25 mm^3

But more relevantly, compared to other strength-related literature on skutterudites, the strength of the herein described skutterudites are equivalent or superior. Electrical discharge machined prismatic bars of 1.5 x 2.0 x 28 mm of n-type $CoSb_3$ and p-type $CeFe_{3-x}Ru_xSb_3$ were flexure strength tested at room temperature in Ref. [10]. The authors cite the general use of ASTM C1161 [4] and 4-point-bending but do not specifically state the flexure fixture size they used though it is surmised here they used 10 and 20 mm spans. They report a characteristic strength of 91 MPa for the n-type material, and 40 MPa for the p-type material. To enable a comparison to the present study's strength statistics in Table II (i.e., m = 5), their results produce associated $k_L L$ = 23.3 mm, $k_A A$ = 26.3 mm^2, and $k_V V$ = 2.9 mm^3 (see Ref. [7] for $k_A A$ and $k_V V$ calculations for 4-point-bending). Using the general Weibull scaling form of S_2 = (effective size 1 / effective size 2)$^{1/m}$ • S_1 for the same probability of survival shows the present study's failure stresses would expected to be ~ 50-60% higher. This suggests that the strength of the n-type materials in the two studies is similar but the p-type material strength in the present study is superior.

I.D. Summary and Conclusions

The failure stress distributions of $Yb_{0.27}Co_4Sb_{12.08}$ (n-type) and $Ce_{0.86}Co_{1.02}Fe_{2.98}Sb_{11.97}$ (p-type) skutterudites were measured as a function of temperature. A self-aligning, high-temperature-capable three-point-bend fixture was developed and used to test specimens whose cross-sectional dimensions (1.5x1.5 mm) are equivalent to those typically used in thermoelectric device legs. Tests were run at sufficiently rapid loading rates so fast-fracture or inert strengths were measured.

The strength of the n-type skutterudite was approximately 115 MPa (L_{eff} = 2.67 mm or A_{eff} = 2.33 mm^2 or Veff = 0.25 mm^3 for m = 5), and that was independent of temperature to 500°C. The strength of the p-type skutterudite was equivalent to that of the n-type material (same effective sizes) and also was independent of temperature to at least 200°C. The p-type's strength dropped by ~20% at 400°C. The herein described n-type skutterudite has a strength comparable to another n-type skutterudite in the literature but this study's p-type has a superior strength.

I.E. Geometry Effect on Transport Properties

Electrical transport properties are usually conducted on small specimens. Due to the lack of standards, specimens being tested have large variations in geometry. It has not been well documented on how sample size the probe distance will affect testing results. A study on sample geometry was conducted using bismuth telluride from the Marlow Industries.

Figure 6 is the typical set up to measure Seebeck coefficient and electrical resistivity. The two current electrodes are on the top and bottom. They are 4 mm x 4 mm, which define the largest specimen dimensions in the cross section area. The current electrodes can move from 8 mm to 22 mm which are the sample length limits. The two thermocouple/voltage probes are 3-8 mm. Typical specimens for the tests are 2-3 mm x 2-3 mm x 10-15 mm.

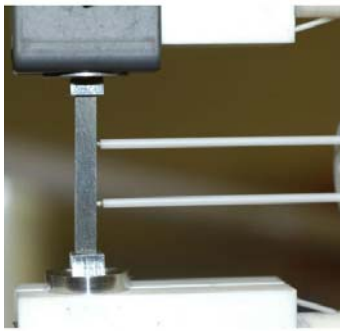

Figure 6. Test set up and specimen geometry

We used n-type and p-type bismuth telluride bars with dimensions of 2 mm x 2 mm x 15 mm. The first set experiment was to vary the probe distance from 4, 5, 6 and 8 mm. As shown in Figure 7, the power factor (product of Seebeck coefficient square and electrical conductivity) of the materials was tested from 50 to 200ºC. The error bars at each temperature indicate the variations caused by changing probe distance. The lower temperature (50-100ºC) the change was about 5-7 % and 2-3 % at higher temperatures (150-200ºC).

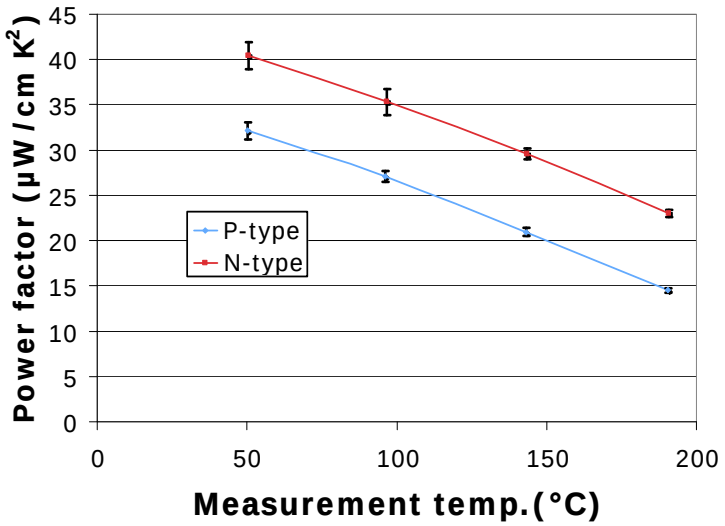

Figure 7. Effect of probe distance: 8, 6, 5, and 4 mm apart.

Figure 8 shows the power factor as a function of temperature when the probe distance was fixed at 5 mm and sample height was changed from 10 to 15 mm. The largest variation was from n-type sample at 50ºC. For most case we observed 2-4% variations in power factors.

These two set of test suggested specimen geometry does not affect the test results greatly within the range we tested. It is always recommended to use the standard sample size for the test equipment. Unexpected error can occur when the sample geometry limits are pushed and testing conditions are changed.

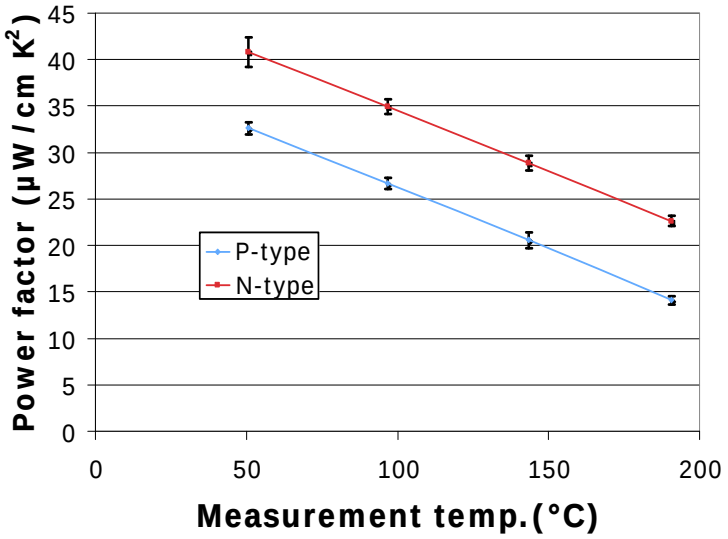

Figure 8. Effect of specimen height: 15, 12 and 10 mm with 5 mm probe distance.

II. CRADA with Marlow

Thermomechanical and thermophysical testing of Marlow-supplied materials continued throughout the FY10Q1.

Status of FY 2010 Milestones

1. Generate thermoelastic and mechanical property database as a function of temperature on candidate p- and n-type TEMats fabricated by Marlow Industries as part of CRADA. (09/10) *On schedule*.
2. Develop in-situ thermal-gradient-strength test method for TEMats. (09/10) *On schedule.*

Communications/Visits/Travel

Marlow's R. McCarty visited Wereszczak and Wang at ORNL on 22 Oct 2009 for a semiannual Marlow-ORNL CRADA meeting.

Problems Encountered

None.

Publications/Presentations/Awards

J. R. Salvador, J. Yang, X. Shi, H. Wang, and A. A. Wereszczak, "Transport and Mechanical Property Evaluation of $(AgSbTe_2)_{1-x}(GeTe)_x$ (x=0.80, 0.82, 0.85, 0.87 and 0.90)," *Journal of Solid State Chemistry*, 182:2088-2095 (2009).

J. R. Salvador, J. Yang, X. Shi, H. Wang, A. A. Wereszczak, H. Kong, and C. Uher, "Transport and Mechanical Properties of Yb-Filled Skutterudites," *Philosophical Magazine*, No. 19, 89:1517-1534 (2009).

A. A. Wereszczak, M. E. Ragan, K. T. Strong, Jr., P. J. Ritt, H. Wang, J. R. Salvador, and J. Yang, Strength of N- and P-Type Skutterudites," to appear in Vol. 31, *Ceramic Enginering and Science Proceedings*, 2010.

References

[1] W. D. Kingery, "Factors Affecting Thermal Stress Resistance of Ceramic Materials," *Journal of the American Ceramic Society*, 38:3-15 (1955).

[2] J. R. Salvador, J. Yang, X. Shi, H. Wang, A. A. Wereszczak, H. Kong, and C. Uher, "Transport and Mechanical Properties of Yb-Filled Skutterudites," *Philosophical Magazine*, No. 19, 89:1517-1534 (2009).

[3] A. A. Wereszczak, H. -T. Lin, T. P. Kirkland, M. J. Andrews, and S. K. Lee, “Strength and Dynamic Fatigue of Silicon Nitride at Intermediate Temperatures,” *Journal of Materials Science,* 37 1-16 (2002).

[4] "Standard Test Method for Flexural Strength of Advanced Ceramics at Ambient Temperature," ASTM C 1161, Vol. 15.01, ASTM, West Conshohocken, PA, 2008.

[5] "Test Method for Flexural Strength (Modulus of Rupture) of Electronic-Grade Ceramics (Withdrawn 2001)," ASTM F417, ASTM, West Conshohocken, PA, 1996.

[6] "Standard Practice for Reporting Uniaxial Strength Data and Estimating Weibull Distribution Parameters for Advanced Ceramics," ASTM C 1239, Vol. 15.01, ASTM, West Conshohocken, PA, 2008.
[7] G. D. Quinn, “Weibull Strength Scaling for Standardized Rectangular Flexure Specimens,” Journal of the American Ceramic Society, 86:508-510 (2003).
[8] O. M. Jadaan and A. A. Wereszczak, “Probabilistic Design Optimization and Reliability Assessment of High Temperature Thermoelectric Devices,” *Ceramic Engineering and Science Proceedings*, [3], 29:157-172 (2008).
[9] A. A. Wereszczak, T. P. Kirkland, O. M. Jadaan, and H. Wang, "Strength of Bismuth Telluride," *Ceramic Engineering and Science Proceedings*, 30, [9] 131-142 (2009).
[10] V. Ravi, S. Firdosy, T. Caillat, B. Lerch, A. Calamino, R. Pawlik, M. Nathal, A. Sechrist, J. Buchhalter, and S. Nutt, “Mechanical Properties of Thermoelectric Skutterudites,” pp. 656-662 in CP969, Space Technology and Applications International Forum – STAIF 2008, Ed. M. S. El-Genk, American Institute of Physics, 2008.

Agreement 16308: MBD Thermoelectrics Theory and Structure

David J. Singh
Oak Ridge National Laboratory

Objective/Scope

We will use modern science based materials design strategies to find ways to optimize existing thermoelectric materials and to discover new families of high performance thermoelectrics for waste heat recovery applications. The emphasis will be on the thermoelectric figure of merit at temperatures relevant to waste heat recovery and on other properties important for applications, especially anisotropy and mechanical properties.

Technical Highlights

Vehicular applications of thermoelectric materials for waste heat recovery will be greatly facilitated by the identification of high performance materials that have low cost and are available in large quantities. Critically, high thermoelectric performance as characterized by the figure of merit *ZT*, at operating temperature, is needed. High figure of merit in turn depends on finding conductive materials with narrow electronic energy bands and low thermal conductivity. The narrow bands are needed in order to obtain high values of the thermopower, which is a key ingredient in the figure of merit. One approach has been the use of Zintl phase compounds. Examples include clathrates, filled-skutterudites and Na_xCoO_2. These materials are based on covalent frameworks that support conduction in combination with electropositive elements that donate charge to the framework. Ideally, the cations provide sites on which alloying can be done to reduce thermal conductivity and provide doping while not strongly affecting charge transport. This quarter, we investigated very narrow band Zintl compounds based on anionic clusters. These are different from Zintl phases studied so far because they do not have connected covalent networks. The motivation comes from prior work showing that extremely narrow bands are desirable for high *ZT* provided that carrier localization can be avoided, the fact that cluster compounds may have very narrow bands, and the fact that the Zintl concept provides a route for maintaining carrier mobility with heavy doping. Importantly, Zintl phases based on anionic clusters of inexpensive materials, such as Sn and Sb, suitable for application in vehicles are known.

We did first principles electronic structure and Boltzmann transport calculations for ($SnSb_4$) based Zintl phases in order to establish a proof of principle and to better elucidate this concept. We also performed calculations of the phonon dispersions and vibrational spectra. These showed that the phonon frequencies are low, which is favorable in a thermoelectric material. The compounds studied were K_8SbSb_4, Na_8SnSb_4, $K_4Ba_2SnSb_4$ and the related material Na_5SnSb_3. We used experimental lattice parameters with optimized atomic positions in the unit cells. The crystal structures are shown in Fig. 1.

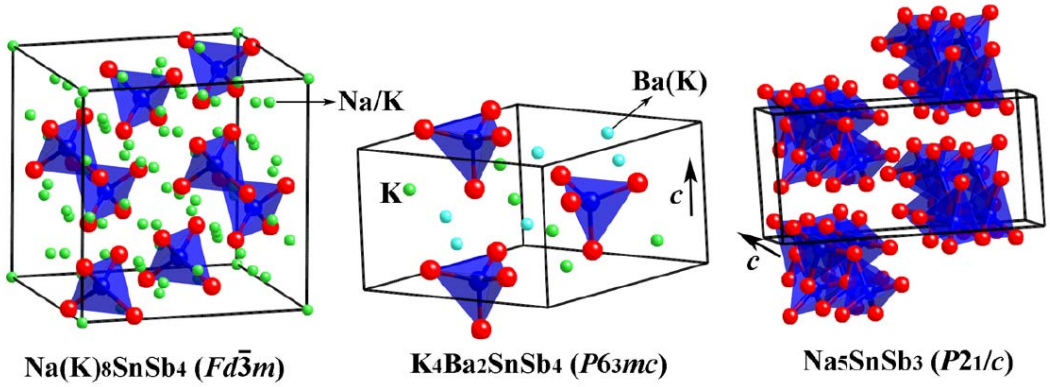

Fig. 1 Crystal Structures of $SnSb_4$ based Zintl phases. The clusters are shown as tetrahedra, with Sn at the center, while the interstitial cations are depicted as small light spheres.

Results for the electronic band structure and the calculated thermopower as a function of temperature and doping are shown in the left panels of Fig. 2 for Na_8SnSb_4. As anticipated we find narrow bands including at the valence band edge. Importantly, we find a band structure with bands of different character at the valence band maximum: a very flat band and a more dispersive band. This combination is favorable for thermoelectric performance since a heavy band enhances thermopower while a light band enhances conduction.

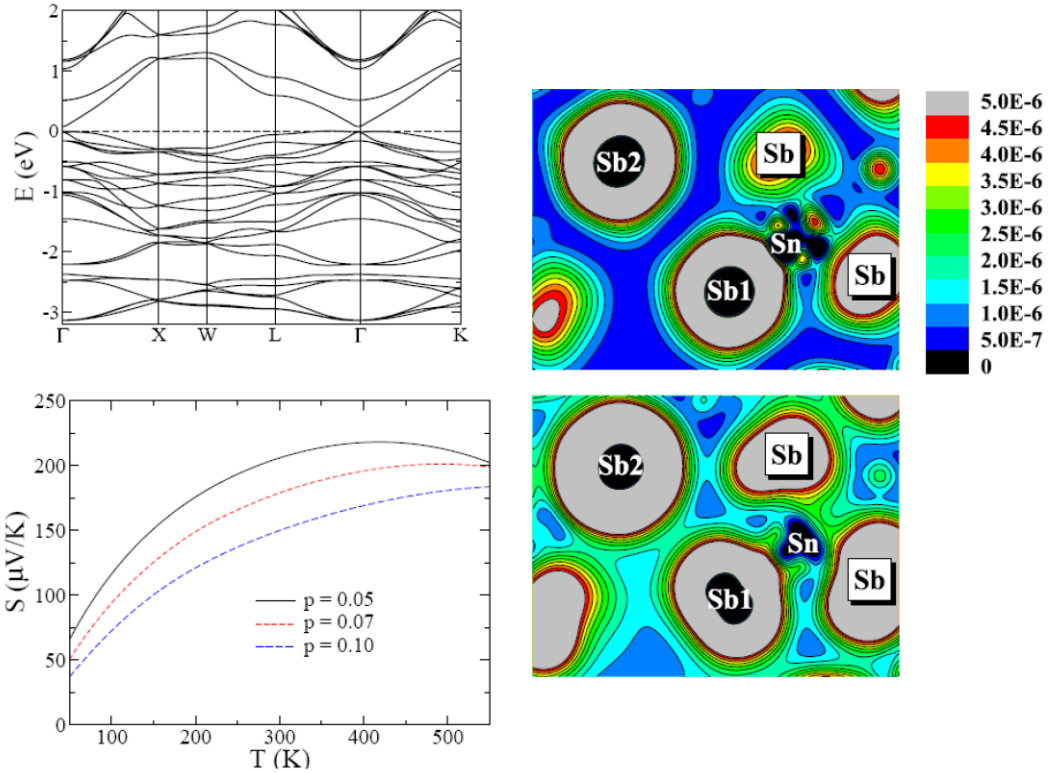

Fig. 2 Band structure (top left), thermopower (bottom left) and charge density associated with the top dispersive valence band (right) for Na_8SnSb_4.

The charge density associated with the dispersive band shows the reason for this. The band derives from the non-bonding frontier orbitals of the cluster, which point out of the cluster and therefore overlap the neighboring clusters more strongly than the deeper valence bands. This is a generic result, which we also find for the other compounds for which calculations were done. Also, as mentioned, we find soft lattices for these materials. This also is expected to be a generic feature of cluster compounds, since they do not have connected networks of covalent bonds.

The thermopower is high for reasonable doping levels especially in the 300 – 450 K range. These results by themselves would suggest that these compounds could be useful thermoelectrics. However, this not the case because of the high content of K or Na in the compounds studied. These large alkali contents imply that the compounds would react with water and making them unsuitable for vehicles and in addition the maximum thermopower is at too low temperature relative to exhaust gas temperatures for efficient waste heat recovery. What the results do show is that the concept of using Zintl cluster compounds as thermoelectrics is viable. Based on this, we will investigate Zintl cluster compounds with more stable chemistry based on larger electronegativity difference between the central atom in the cage and the outer atoms, and higher valent electropositive ions.

Status of FY 2010 Milestones

We are progressing towards our milestone of predicting new thermoelectric compositions. Strategies that will be used are to continue investigation of Cu containing delafossites, other narrow band oxide materials, and chalcogenides. We also plan to continue investigation of nano-structured PbSe and related materials. Depending on the results we will continue with those materials and/or investigate alternate narrow band oxides containing mixed-valent transition element ions and Zintl-phase materials.

Communications/Visits/Travel

D.J. Singh hosted a two day visit to ORNL by Professor Claudia Felser (Mainz, Germany). She presented recent results on various new materials including several half-heusler thermoelectric compositions. Research discussions on this subject were held over the course of the visit. Professor Felser also discussed the interests of German manufacturers, especially BMW and Bosch, in thermoelectric and piezoelectric materials.

Problems Encountered

No significant problems encountered this quarter.

Publications/Presentations/Awards

D.J. Singh was part of a team that received the ORNL Director's Award for Outstanding Team Accomplishment in Science and Technology. D.J. Singh was promoted to an ORNL Corporate Fellow.

References

1. D.J. Singh and L. Nordstrom, *Planewaves, Pseudopotentials and the LAPW Method, 2nd Edition*, Springer, Berlin, 2006.

2. G.K.H. Madsen and D.J. Singh, “BoltzTraP: A code for calculating band-structure dependent quantities,” *Computer Physics Commun.* **175**, 67 (2006).

Agreement 17859: Durability of ACERT Engine Components

Hua-Tay Lin, T. Kirkland, and B. Armstrong
Oak Ridge National Laboratory

N. Philips and J. Jenson
Caterpillar, Inc.

Objective/Scope

There are four primary goals of this research agreement, which contribute toward successful design and implementation of advanced lightweight material components to achieve high-efficiency engine of 55% of heavy-duty diesel engines by 2012 as set under the 21st CT program: 1) the generation of a mechanical engineering database of candidate advanced lightweight materials before and after exposure to simulated engine environments; 2) the microstructural evolution and accompanied chemical changes during service in these advanced materials; 3) material selection, development, and design of complex-shaped components, and 4) application and verification of probabilistic life prediction methodology for advanced high-efficiency diesel engine components. The methodology implemented would also help to manufacture consistent mechanical reliability and performance of complex shaped components.

Technical Highlights

Development of Al-oxide based environmental barrier coating (EBC) for the ferritic Fe-steel substrates was undertaken during this reporting period. The objective this thermal testing is to provide an alternative option to provide an effective protection for the ferritic Fe-steel under the engine application environment. The Si-rich ferritic Fe steel alloy is the current production material used for the exhaust components in the heavy-duty diesel engines. The application of EBC would allow end users to significantly reduce the heat rejection and also prevent the oxidation/corrosion degradation process encountered in the current production materials. Thus, it would allow the OEMs to avoid the use of the very high-cost stainless steel materials for the exhaust port and manifold components. This is one of the key enabling materials technologies that would allow end users to achieve 55% engine efficiency by 2012 as set under the 21st Century Truck Program.

Colloidal processing offers a low cost alternative approach for producing uniform coatings on complex-shaped components via a simple dip coating process (i.e., the ORNL slurry coating process) (1-2). Also, the oxide-based coating could be processed at lower temperature and shorter times, thus preventing the interaction (chemical reaction) between the coating and Fe-based substrate. Control of the rheological behavior of the suspension by tailoring interparticle (or surface) forces is paramount to achieve a high quality defect free coating. In aqueous-based suspensions long-range attractive van der Waals forces must be balanced by repulsive forces to tailor the desired degree of suspension stability. Typically, ionizable polymeric dispersants, or polyelectrolytes, are used to modify the surface of particles to impart repulsive electrosteric forces (3-4). Aluminum, (H10, Valimet Inc., Stockton, CA) was used as the metal powder in this study. The aluminum powder had an average particle size of ~ 13.19 μm and surface area of 0.4475 m2/g, determined using dynamic light scattering

(Horiba, Inc., Kyoto, Japan) and B.E.T. (Autosorb-1, Quantachrome Instruments, Boynton Beach, FL), respectively. Polyacrylic acid (PAA, 450kg/mol, Aldrich Chemicals, Milwaukee, WI), an anionic polyelectrolyte, was used as the dispersant and PL001 (Polymer Innovations, Inc., Vista, CA) as the rheological modifier for the Al system. Water purity was measured using inductively coupled plasma mass spectroscopy (ICPMS, X Series 2, Thermo Fisher Scientific, Inc., Waltham, MA). The standards (QCS26, High Purity Standards, Charleston, SC) and the nitric acid matrix (Ultrex Pure, J.T. Baker, Phillipsburg, NJ) were used to calibrate the ICPMS. The Al-oxide based coating was employed via a dip or slurry based process. A post heat treatment at 850°C in air was carried out to covert the slurry coating into the oxide based coating.

Figure 1 shows the polished cross section of as-coated Al-oxide based layer on the ferritic Fe steel alloy substrate. Note a Cu plating layer (the most outer layer) was deposited prior to the metallographic polishing. The voids observed in the Fe-based substrate resulted from the electric plating process as well. The detailed SEM observations show that a dense and coherent Al-oxide layer (~ 20 micron thick) containing Fe element presumably coming from the substrate, formed after the heat treatment (Fig. 1). Study of the heat treatment conditions (i.e., temperature and time) will be carried out to determine an effective window for an optimized coating layer. In addition, study of thermal cycle will be carried out to determine long-term stability of the Al-oxide based coating via the low-cost aqueous processing method.

Status of FY 2010 Milestones

Complete testing and analysis of a prototype ACERT exhaust component with advanced thermal barrier coating. **(09/10**) – On schedule.

Communications/Visits/Travel

H. T. Lin, M. Kass, and D. R. Johnson of ORNL and J. G. Sun of ANL visited N. Philip and J. Jenson of Caterpillar on Nov. 18, 2009 to discuss the up-to-date research plans ACERS engine and components.

Communications and conference calls with Dr. Philip of Caterpillar and Dr. Sun of ANL regarding the up-to-date progress on development of alternative EBC systems for ACERS engine and components.

Communications with Dr. Kass at NTRC regarding the up-to-date status on the installation of C15 ACERT engine.

Problems Encountered

None.

Publications/Presentations/Awards

Dr. H. T. Lin has been chosen as the winner of the prestigious 2010 James I. Mueller Memorial Award in recognition of his contributions and leadership in the field of engineering ceramics. The James I. Mueller Award is the highest honor bestowed by Engineering Ceramics Division, the American Ceramic Society.

References
1. Armstrong, B., Kirby, G., Cooley, K., *Proceedings of The 29th International Technical Conference on Coal Utilization & Fuel Systems*, Clearwater, FL (2004).
2. Kirby, G., Cooley, K., and Armstrong, B., *Proceedings of GT2005 ASME Turbo Expo 2005: Power for Land, Sea, and Air*, Reno-Tahoe, NV (2005).
3. Cesarano, J. and Aksay, I., *J. Am. Ceram. Soc.*, 71 (4) 250-55 (1988).
4. Cesarano, J. and Aksay, I., *J. Am. Ceram. Soc.*, 71 (12) 1062-67 (1988).

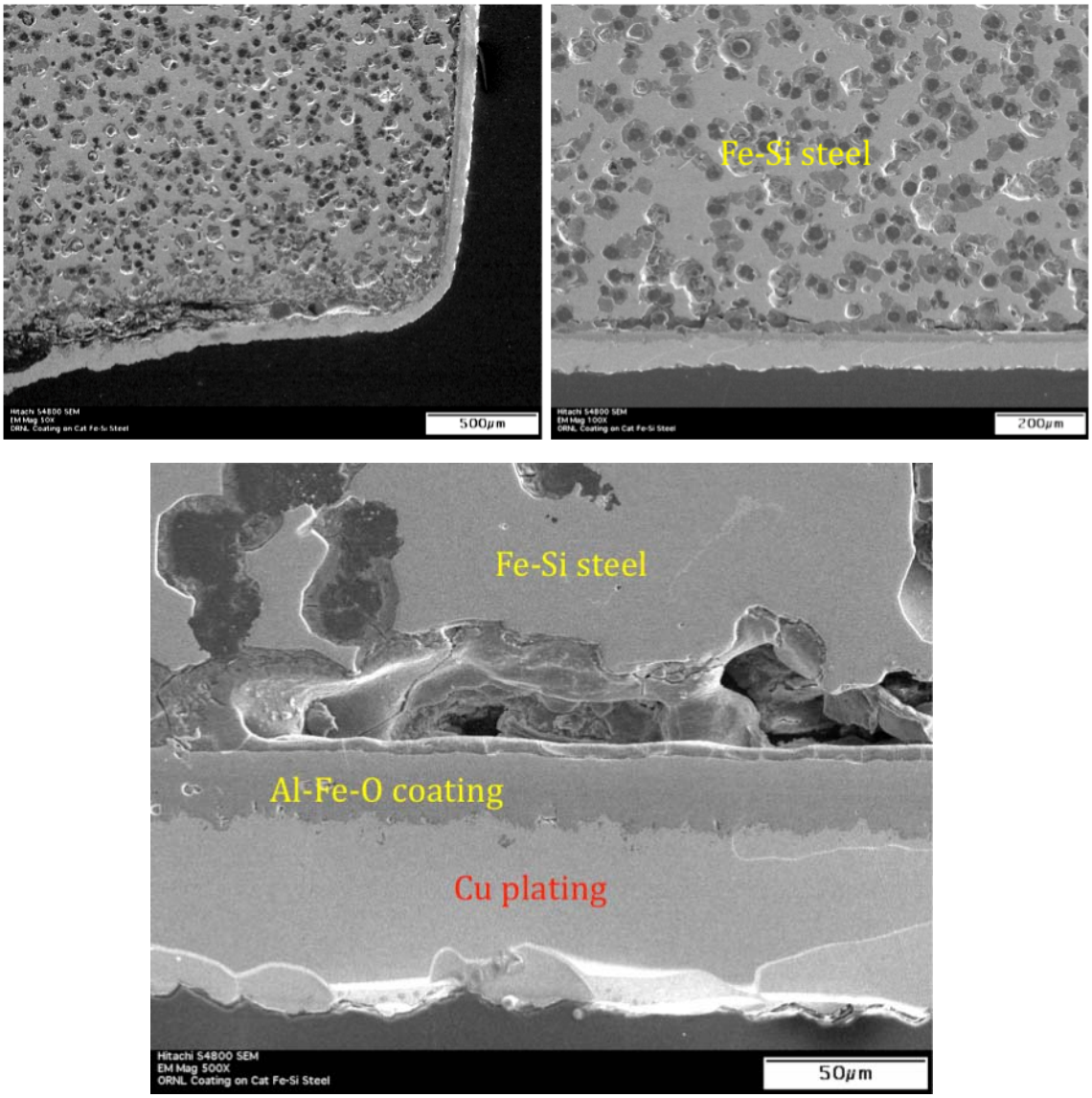

Figure 1. SEM photomicrographs showed the as-deposited Al-oxide based coating via the low-cost aqueous processing method.